REFERENCE ONLY

UNIVERSITY OF LONDON THESIS

Degree PhD Year 2006 Name of Author CURATI, S. F

COPYRIGHT
This is a thesis accepted for a Higher Degree of the University of London. It is an unpublished typescript and the copyright is held by the author. All persons consulting the thesis must read and abide by the Copyright Declaration below.

COPYRIGHT DECLARATION
I recognise that the copyright of the above-described thesis rests with the author and that no quotation from it or information derived from it may be published without the prior written consent of the author.

LOANS
Theses may not be lent to individuals, but the Senate House Library may lend a copy to approved libraries within the United Kingdom, for consultation solely on the premises of those libraries. Application should be made to: Inter-Library Loans, Senate House Library, Senate House, Malet Street, London WC1E 7HU.

REPRODUCTION
University of London theses may not be reproduced without explicit written permission from the Senate House Library. Enquiries should be addressed to the Theses Section of the Library. Regulations concerning reproduction vary according to the date of acceptance of the thesis and are listed below as guidelines.

A. Before 1962. Permission granted only upon the prior written consent of the author. (The Senate House Library will provide addresses where possible).

B. 1962 - 1974. In many cases the author has agreed to permit copying upon completion of a Copyright Declaration.

C. 1975 - 1988. Most theses may be copied upon completion of a Copyright Declaration.

D. 1989 onwards. Most theses may be copied.

This thesis comes within category D.

☑ This copy has been deposited in the Library of UCL

☐ This copy has been deposited in the Senate House Library, Senate House, Malet Street, London WC1E 7HU.

C:\Documents and Settings\lproctor\Local Settings\Temporary Internet Files\OLK8\Copyright - thesis (2).doc

und By
Bookbinders
)992 3965
lissetts.com

GROWTH AND DOPING OF CVD DIAMOND FILMS

Stéphane Pierre Curat

Thesis submitted for the degree of Doctor of Philosophy

Department of Electronic and Electrical Engineering
University College
University of London

October 2005

UMI Number: U591899

All rights reserved

INFORMATION TO ALL USERS
The quality of this reproduction is dependent upon the quality of the copy submitted.

In the unlikely event that the author did not send a complete manuscript
and there are missing pages, these will be noted. Also, if material had to be removed,
a note will indicate the deletion.

UMI U591899
Published by ProQuest LLC 2013. Copyright in the Dissertation held by the Author.
Microform Edition © ProQuest LLC.
All rights reserved. This work is protected against
unauthorized copying under Title 17, United States Code.

ProQuest LLC
789 East Eisenhower Parkway
P.O. Box 1346
Ann Arbor, MI 48106-1346

ABSTRACT

The extreme properties of diamond combined with the emergence of chemical vapour deposition (CVD) techniques for the growth of large area free standing diamond wafers has led to considerable interest in the use of this material for electronic applications. However, to date, the polycrystalline nature of the material grown by heteroepitaxy has hindered progress in this field leading to only niche applications for diamond electronics being identified. Whilst homoepitaxial growth seemed to be a solution to counter this issue, the substrate cost and the lack of a suitable dopant for *n*-type conductivity together with the relatively large activation energy of *p*-type dopants reduced the effectiveness of electronic devices made from diamond. Finally, the low growth rates using standard microwave CVD techniques remains a problem.

This thesis presents electronic characterisation of such homoepitaxial films using Hall effect measurements. The observation of *p*-type character of the surface conductivity due to hydrogen termination was confirmed and a correlation between the transport properties and the film thickness was demonstrated. In addition to Hall effect measurements, SEM/STM data are presented and the parameters for high growth rates of these overlayers are revealed. Passivation of these layers has also been investigated so that the *p*-type character and hence the device operation is not lost at higher temperatures when the devices are operated in air. A newly developed material, ultrananocrystalline diamond (UNCD), has been studied for its *n*-type character. Hall effect measurements revealed the conductivity of this material is strongly influenced by the addition of nitrogen into the source gases and UNCD becomes conductive with low thermal activation energy. Finally, impedance spectroscopy measurements were taken on both UNCD and phosphorus doped material to investigate the conduction paths in both materials that lead to the *n*-type conductivity observed in both kind of materials.

The likely impact of the realisation of more effective processes for both growth and doping, described here, for the development of electronic devices from diamond is discussed.

ACKNOWLEDGMENTS

First I would like to thank my supervisor, Dr Richard B. Jackman, for welcoming me in his group and offering me the possibility to carry out a PhD at UCL. His encouragements, enthusiasm and support through this PhD were invaluable. His constant stream of ideas, suggestions and increasingly audacious abstract writing will not be forgotten either and have left me too exhausted to eulogise extensively.

London is an expensive place to live in and I could not have completed my PhD without permanent financial support. The award of a post-graduate studentship from the European consortium DoDDS (Doped Diamond Devices and Sensors) for the first two years of my PhD studies is greatly acknowledged. I owe also a fundamental thank to the Diamond Electronics Group at UCL for supporting me financially thereafter until the submission of this thesis. The Institute of Physics (IOP) and the Graduate School at UCL significantly contributed to the costs of attending several conferences on diamond in the form of travel bursaries.

Oliver Gaudin, Costas Mavroidis, Damianos Troupis, Oliver Williams, Haitao Ye, and again Richard Jackman have been my colleagues, and friends, within the Diamond Electronics Group. I would like to thank all of them although I believe thanks are not enough. They have all provided help at some point in one way or another and have contributed to make a chaotic but creative working environment giving me a long-lasting memory of many good moments. Discussions, often around a beer, with previous group members, namely (in alphabetical order) Bhaswar Baral, Simon Chan, Stuart Lansley, Hui Jin Looi, Duncan Marshall, Robert Mckeag, Lisa Pang and Mike Whitfield have been also helpful and fuelled new ideas.

Within the department of Electronic and Electrical Engineering I would like to thank more specifically Trevor and Jim from the workshop, as well as the cleanroom staff, Takashi Matsuura, Kevin Lee, Mike Creswell and previously Vic Law, who often provided help in the form of technical support and advice in device processing.

Finally, I wish to keep the last words of these acknowledgements to express my gratitude to my family for permanent support and encouragements over the years. This thesis is for them (although, I know, they will not read it!). Also, heart felt thanks are expressed to Simona for her love and support during this endeavour.

TABLE OF CONTENTS

Abstract **1**

Acknowledgments **2**

Table of contents **4**

Chapter I: Introduction **8**

Chapter II: Structure, growth, doping, properties and applications of diamond **12**

II.1. Introduction 13

II.2. Structure of diamond 13

II.3. Synthesis of diamond 19

II.3.1 Natural diamond 19

II.3.2 Synthetic diamond 20

II.4. CVD growth techniques 26

II.4.1 Hot Filament Chemical Vapour deposition (HFCVD) 26

II.4.2 Plasma Enhanced CVD (PECVD) 27

II.4.3 Combustion flame CVD 32

II.4.4 Comparison of CVD diamond films 33

II.5. Nucleation mechanisms 34

II.5.1 Gas phase nucleation 35

II.5.2 Surface nucleation 36

II.6 Growth of diamond by CVD methods 41

II.6.1 Substrate materials 41

II.6.2 Effect of H_2, N_2, O_2 and noble gases 43

II.6.3 Surface pre-treatments and nucleation enhancement 44
II.6.4 Deposition conditions 46
II.7. Doping of diamond 48
II.7.1 *p*-type doping 48
II.7.2 *n*-type doping 52
II.8. Properties of diamond 54
II.9. Applications of diamond 55
II.9.1 Mechanical applications 56
II.9.2 Thermal applications 56
II.9.3 Optical applications 57
II.9.4 Electronic applications 58
II.10. References 60

Chapter III: Experimental and characterisation techniques 70

III.1. Introduction 70
III.2. Surface cleaning and preparation 71
III.2.1 Acid bath cleaning of diamond surfaces 71
III.2.2 Hydrogenation of diamond surfaces 72
III.3. Surface characterisation 73
III.3.1 Scanning electron microscopy 73
III.3.2 Scanning tunnelling microscopy 74
III.4. Resistive deposition of metal contacts 76
III.5. Electrical characterisation 78
III.5.1 IV measurements 78
III.5.2 Hall effect measurements 78
III.5.3 Impedance spectroscopy measurements 84
III.6. References 88

Chapter IV: Homoepitaxial films 90

IV.1. Introduction 90
IV.2. Experimental methods 92
IV.3. Results 93
IV.3.1 Homoepitaxy on diamond substrates having the same thickness 93
IV.3.2 Homoepitaxy on diamond substrates having a different thickness 97
IV.3.3 High growth rates 100
IV.4. Discussion 103
IV.6. Concluding remarks 106
IV.7. References 107

Chapter V: Passivation of hydrogenated diamond surfaces 109

V.1. Introduction 109
V.2. Electronic properties of hydrogen-terminated diamond surfaces 110
V.3. Experimental methods 118
V.4. Results 119
V.5. Discussion 124
V.6. Concluding remarks 126
V.7. References 127

Chapter VI: Ultrananocrystalline diamond: Hall effect measurements 129

VI.1. Introduction 129
VI.2. Experimental methods 130
VI.3. Results 131
VI.4. Discussion 136
VI.5. Concluding remarks 141
VI.6. References 141

Chapter VII: Ultrananocrystalline diamond: Impedance spectroscopy....................143

VII.1. Introduction....................143

VII.2. Experimental methods....................144

VII.3. ANL analysis of UNCD films....................146

VII.4 Results: Impedance spectroscopy measurements....................150

VII.5. Discussion....................160

VII.6. Concluding remarks....................162

VII.7. References....................163

Chapter VIII: Phosphorus-doped diamond: Impedance spectroscopy....................166

VIII.1. Introduction....................166

VIII.2. Experimental methods....................168

VIII.3. Results....................169

VIII.3.1 Current-voltage characteristics....................169

VIII.3.2 Impedance spectroscopy measurements....................171

VIII.4. Discussion....................175

VIII.5. Concluding remarks....................179

VIII.6. References....................180

Chapter IX: Concluding remarks....................184

CHAPTER I
INTRODUCTION

Diamond has been long known as a precious gemstone. Its semiconducting properties were discovered in the 1950's [1]. Although there is still nowadays a strong demand for optically flawless diamonds for the gem industry, the extreme properties of diamond have led to much interest in the scientific community during the past decades. Many physicists have shown that the combination of physical, chemical and electronic properties of diamond will make it far more superior than the existing semiconductor materials.

However, the realisation of diamond as an electronic material did not come without any difficulties. The natural form of diamond poses many restrictions in terms of economics, quality, functionality and reproducibility. High-pressure high-temperature (HPHT) synthesis overcomes some of these issues by converting graphitic carbon to diamond but produces material similar to that found in nature in that it is small and contains impurities. Diamond as a semiconductor material has made much more progress since the emergence of chemical vapour deposition (CVD). When compared with HPHT techniques, the CVD techniques enables the synthesis of diamond uniformly and reproducibly over a greater surface area. Thus, together with the possible incorporation of dopant impurities during crystal growth, semiconducting diamond films may be synthesised to allow the formation of electronic applications to be explored.

During the last decade, much progress has been achieved in diamond growth by CVD, leading to the production of electronic device grade diamond films. However, to date, the impact of CVD diamond has been limited to niche applications. This problem can be considered to have three origins. Firstly, the CVD method leads to diamond being polycrystalline in nature when grown heteroepitaxially whereas single crystal films are

produced homoepitaxially. Although the quality of polycrystalline diamond may be very high, the presence of grain boundaries strongly affects the electronic properties of the material. Thus, the use of high quality diamond mono-crystals seems to be the only practical way to provide material for the most advanced electronic applications. Secondly, whilst homoepitaxial growth seems to counter the first issue, the lack of suitable dopants for *n*-type conductivity together with the relatively large activation energy of the *p*-type dopants limit the efficiency of any electronic device produced from diamond. Finally the low growth rates of standard microwave plasma CVD techniques, at approximately 1 μm/h, means that the material is not as inexpensive as an alternative electronic material. This problem has been addressed recently by Yan *et al.* [2], where they have achieved rates up to 150 μm/h using microwave plasma enhanced CVD. Their process consisted of adding intentionally nitrogen in the growth gas mixture. However, this approach is not viable for diamond-based electronic applications since nitrogen is known to affect the electronic properties in a negative way.

The purpose of the work presented here is to study the likely impact of more effective processes for both growth and doping for the development of electronic devices from diamond. To begin such a work, the relevant existing information and models, which describe the structure of diamond, is introduced in chapter II. An account of the techniques used to synthesise diamond along with the CVD methods of growing diamond is then presented. In this chapter, doping diamond is mentioned, and the properties and applications of diamond are also reviewed.

The experimental techniques and laboratory equipments used are reviewed in chapter III. Surface cleaning and preparation of the samples are firstly described. This is followed by a description of the surface characterisation techniques. Also included are the different electrical probes that have been used to characterise the sample electrically.

The experimental results commence in chapter IV with the microwave plasma enhanced CVD growth of electronic grade quality diamond films for surface conductive device applications. The aim of the experiments reported here is to gain control over the carrier transport properties of the homoepitaxial films, while finding a solution to circumvent the problem associated with low growth rates when no nitrogen is introduced in the growth gas mixture.

When the diamond surface is terminated with hydrogen, e.g. after diamond growth, a *p*-type surface conductive layer is formed, which has already allowed Schottky diodes and metal-semiconductor field effect transistors (MESFETs) to be fabricated. These devices have been shown to be capable of operation at temperatures up to 250°C in air. Unfortunately, at higher temperatures, the *p*-type character and hence the device operation, is lost when the devices are operated in air. In chapter V, the current understanding in the field of hydrogenated diamond is first reviewed. Passivation of these *p*-type surfaces is then used in order to counter this problem and hence allows useful devices to emerge from this technology.

The development of diamond has been hindered by the difficulty of obtaining *n*-type semiconducting diamond. However, ultrananocrystalline diamond (UNCD), when grown with nitrogen in the gas reactants, exhibits *n*-type conductivity. The electrical conduction mechanisms behind this behaviour are yet unclear. In chapters VI and VII, Hall measurements and impedance spectroscopy are applied respectively to study of the transport and conduction mechanisms within this material.

Doping diamond with phosphorus is another alternative to obtain *n*-type diamond. The transport properties, which have been investigated by Hall effect measurements, showed that phosphorus gives a donor level ~0.6 eV below the conduction band [3]. Further, charge-based deep level transient spectroscopy (Q-DLTS) measurements have identified electrically active defect states (that also contribute to conductivity within the film) that

may accompany the introduction of phosphorus to the diamond [4]. However, no impedance spectroscopy measurements have been performed. In chapter VIII, impedance spectroscopy is applied to gain further insights into this system.

Finally, chapter IX provides some concluding remarks to the whole study.

References

[1] J. J. Brophy, Phys. Rev. 99, 1336 (1955).

[2] C. S. Yan, Y. K. Vohra, H. K. Mao, and R. J. Hemley, Proceedings of the National Academy of Sciences 99, 12523 (2002).

[3] S. Koizumi, T. Teraji, and H. Kanda, Diamond Relat. Mater. 9, 935 (2000).

[4] O. Gaudin, D. K. Troupis, R. B. Jackman, C. E. Nebel, S. Koizumi, and E. Gheeraert, J. Appl. Phys. 94, 5832 (2003).

CHAPTER II
STRUCTURE, GROWTH, DOPING, PROPERTIES AND APPLICATIONS OF DIAMOND

II.1. Introduction
II.2. Structure of diamond
II.3. Synthesis of diamond
- II.3.1 Natural diamond
- II.3.2 Synthetic diamond

II.4. CVD growth techniques of diamond films
- II.4.1 Hot Filament Chemical Vapour deposition (HFCVD)
- II.4.2 Plasma Enhanced CVD (PECVD)
- II.4.3 Combustion flame CVD
- II.4.4 Comparison of CVD diamond growth techniques

II.5. Nucleation mechanisms
- II.5.1 Gas phase nucleation
- II.5.2 Surface nucleation

II.6. Growth of diamond by CVD methods
- II.6.1 Substrate material
- II.6.2 Effect of H_2, N_2, O_2 and noble gases
- II.6.3 Surface pre-treatments and nucleation enhancement
- II.6.4 Deposition conditions

II.7. Doping of diamond
- II.7.1 *p*-type doping
- II.7.2 *n*-type doping

II.8. Properties of diamond
II.9. Applications of diamond
- II.9.1 Mechanical applications
- II.9.2 Thermal applications

II.9.3 Optical applications
II.9.4 Electronic applications
II.10 References

II.1. INTRODUCTION

This chapter presents an introduction to diamond; including its structure, synthesis, properties and applications. Doping of this remarkable material will be also mentioned. The discussion begins with natural diamond, which serves as a reference against which the success of 'artificial' diamond synthesis can be assessed. The work presented in this thesis is based on diamonds that have been grown by chemical vapour deposition (CVD) so after briefly mentioning the alternative means for diamond synthesis, the more common CVD techniques are reviewed.

II.2. STRUCTURE OF DIAMOND

Diamond is an allotrope of carbon. Carbon (symbol C) belongs to the group IV in the periodic table of the elements, like silicon (Si) and germanium (Ge). Its nucleus counts a number of six protons and six, seven or eight neutrons surrounded by six electrons. The electrons for the free carbon atom in its ground state are arranged in the $1s^2 2s^2 2p^2$ electronic configuration. However, in bonded carbon, such as diamond and graphite, the electron configuration is modified. The electronic wave functions of the four electrons occupying the *2s* and *2p* orbitals mix. As a result sp^n hybridization of orbitals occur with $n = 1, 2, 3$ [1] and the three possible hybridizations occurring in carbon are: sp^3 (tetragonal), sp^2 (trigonal) and *sp* (digonal) orbitals.

The sp^3 hybrid orbitals are formed when the electrons in the *2s* and *2p* orbitals rearrange so that they have all the same energy. As a result the valence of the carbon atom is raised from two to four. The four sp^3 hybrid orbitals of carbon are all identical. They have one lobe larger than the other and they point to the corners of a tetrahedron, forming 109°2.8' equal angles to each other as shown in figure II.1.

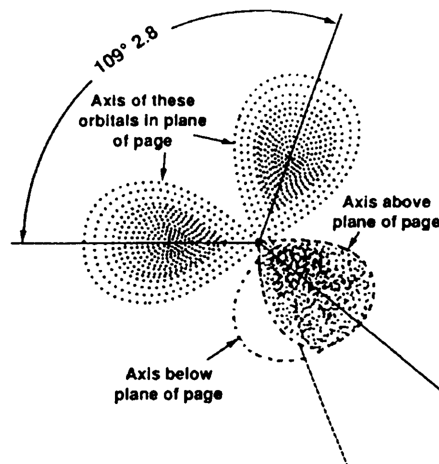

Figure II.1: tetrahedral hybridization axis of the four sp^3 orbitals. (Reproduced from [2])

Diamond is the well known sp^3 bonded polytype of molecular carbon where each carbon atom shares its four sp^3 valence electrons with one sp^3 valence electron of any four other carbon atoms placed around it. The result is that each carbon atom forms a strong covalent σ (sigma) bond with another carbon atom so that a rigid lattice is formed. This lattice is face-centred cubic (fcc) with additional carbon atoms located at a_0(1/4, 1/4, 1/4), a_0(3/4, 3/4, 1/4), a_0(1/4, 3/4, 3/4) and a_0(3/4, 1/4, 3/4), where a_0 is the lattice constant; see figure II.2 below.

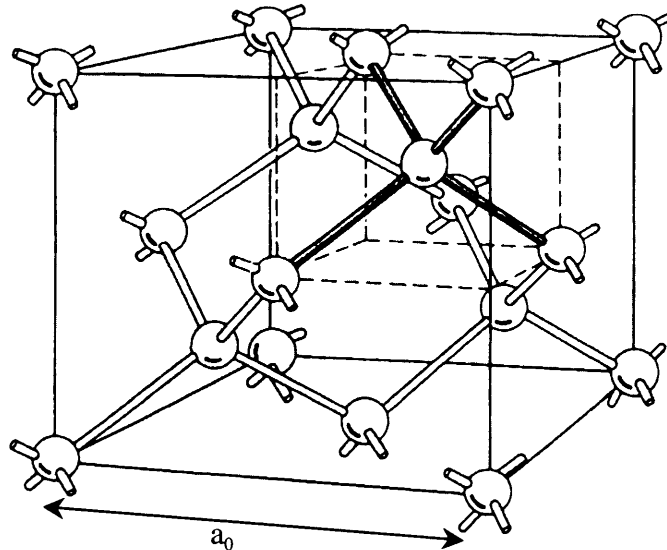

Figure II.2: crystalline structure of diamond and unit cell of diamond highlighting the four tetrahedral bond of a single carbon atom. (After [3]).

This structure can also be viewed as two inter-penetrating fcc lattices displaced from one another by one quarter of the cube diagonal [4]. At 0°C, a_0 = 3.567 Å [5], giving a carbon - carbon bond length of 1.54 Å [2] which energy is 711KJ/mol [2]. Diamond has the highest atom density of any material which explains why diamond is the stiffest, hardest and least compressible of all substances [2].

Diamond can be seen with another perspective as presented in figure II.3(a) where the (111) plane is considered to be formed by a set of basic building blocks having a ring of six carbon atoms in the 'chair' configuration that are stacked according to the ABCABC sequence (see figure II.3(a)). Another stacking pattern can occur with the stacking sequence ABABAB (see figure II.3(b)) giving rise to hexagonal diamond, also called lonsdaleite when it is the hexagonal form of natural diamond.

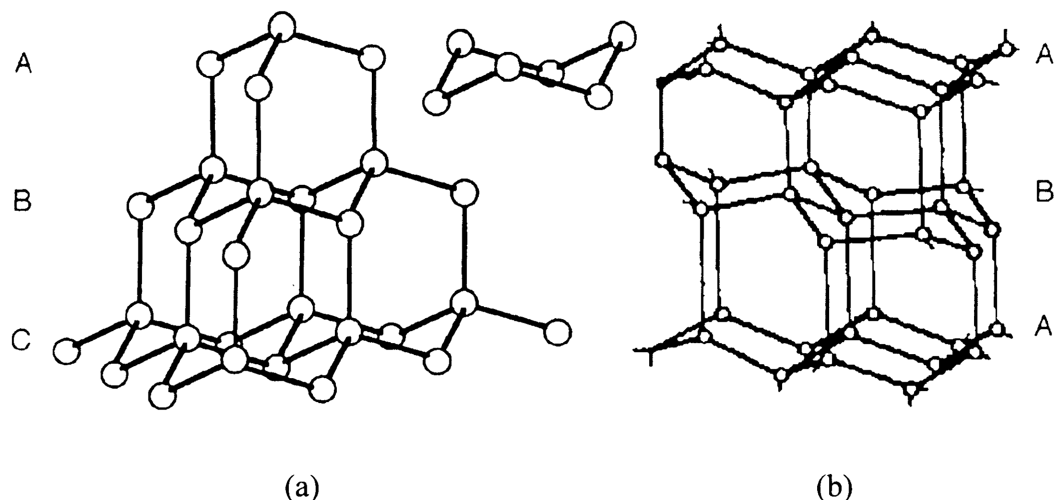

Figure II.3: (a) Left: bonding configuration in cubic diamond with the ABC stacking pattern constructed from the basic block in the 'chair' configuration shown floating. (b) Right: the ABAB stacking pattern of hexagonal diamond, lonsdaleite. (Reproduced from [2])

This form of diamond was discovered in the 1960s during experiments on diamond synthesis but was also found in meteorites [6]. Its structure has a slightly shorter bond length than cubic diamond resulting in a material with a tighter lattice. The direct consequence is that it is stronger than cubic diamond. However the additional bonding energy required for the formation of hexagonal diamond means that cubic diamond is preferentially formed under most conditions.

The sp^2 hybrid orbitals are formed in a manner similar to the sp^3 hybrid orbitals. The only difference is that the four electrons in the *2s* and *2p* orbitals rearrange in two distinct energy levels. Three of these four electrons hybridize to occupy three sp^2 orbitals whilst the remaining one stays in its original *2p* configuration. The sp^2 hybrid orbitals are identical and are coplanar forming a 120° angle between them, as illustrated by figure II.4. The remaining *2p* orbital is pointing perpendicular to the plane formed by the sp^2 orbitals.

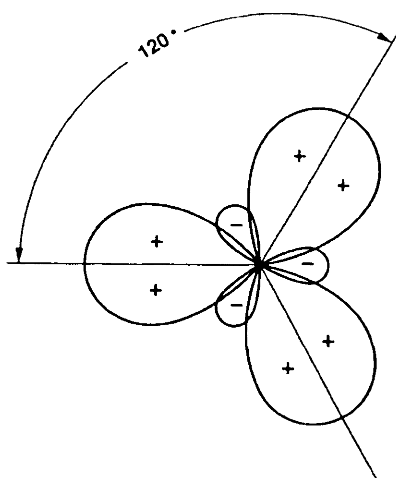

Figure II.4: planar section of the sp^2 hybrid orbitals (Reproduced from [2])

Graphite is known as the sp^2 bonded carbon structure. Each carbon atom shares its three sp^2 hybrid orbitals with the sp^2 hybrid orbitals of any three other carbon atoms placed around it to produce a hexagonal structure located in parallel planes. The sp^2 bonds are strong σ bonds, 0.141 nm long [2]. The remaining *2p* orbitals, perpendicular to the σ bonding plane, overlap to form a pi (π) bond between the parallel sp^2–hybridized carbon planes. The electrons in the π bond region are delocalised and only held together by van der Walls forces. These forces can be easily overcome to allow the planes to slide past each other, explaining the low shear modulus of graphite. Further, the fact that the electrons are delocalised also allows them to move under an electric field, explaining the low resistivity of graphite.

As in the case of diamond, the stacking of planes can occur in two different ways giving either the more common form of graphite (hexagonal structure) with a ABAB stacking pattern (as shown by figure II.5(a)), or the less thermodynamically stable rhombohedral graphite with a ABCABC pattern, as shown in figure II.5(b).

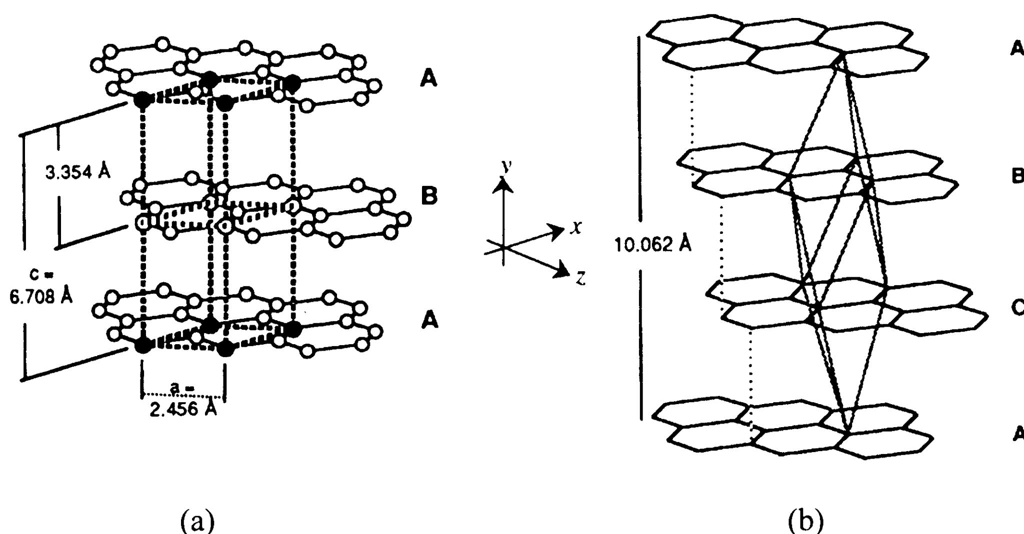

Figure II.5: Schematic drawing of (a) the common form of graphite with an ABAB stacking pattern and (b) the rare rhombohedral form of graphite with a ABCABC stacking pattern (Reproduced from [7]).

The *sp* orbital is the last hybrid orbital that can occur in bonded carbon. In this case the electrons from the *2s* level combine with two electrons from the *2p* level to form two *sp* hybrid levels. The two other valence electrons remain in the *2p* levels. When two *sp*-hybridized carbon atoms bond, a covalent σ bond is formed from the overlapping of the hybrised *sp* obitals. The two remaining valence electrons that are free and delocalised contribute to the formation of two π bonds. This scenario is encountered in molecules such as acetylene HC≡CH and carbides $(C{\equiv}C)_n$ where there is a triple bond between the carbon atoms.

The hybridization of orbitals in molecular carbon is a flexible process from which a whole new range of carbon based materials can be found. The combination of sp^3 and sp^2 bonding accounts for the diversity in number, structure and properties of these carbon materials. Carbon nanotubes and the family of fullerene molecules are two examples of these types of material.

II.3. SYNTHESIS OF DIAMOND

II.3.1 Natural diamond

Natural diamond is believed to have formed over 990 million years ago between 140 km and 200 km beneath the surface of the earth where the temperature ranges from 900°C and 1400°C and the pressure between 45 Kbar and 60 Kbar [8,9]. Diamond crystals then surface in volcanic eruptions and primary deposits are found embedded within kimberlite, a form of solidified lava, inside extinct volcanic pipes [6]. Glacial and alluvial erosion have subsequently distributed these primary deposits over wider geographical areas to form secondary and tertiary deposits.

Natural diamonds display a range of different qualities and purity depending on the conditions under which they were initially formed. A system has been developed based on this variation, as summarised in table II.1.

Type	Abundance	UV absorption edge	IR absorption edge	Nitrogen content
Ia	~98% (natural)	~330 nm	2.5-10 μm	N to 0.3% A and B aggregates; Low levels of single N atoms (<10^{16} cm^{-3}) in single substitutional sites
Ib	~0.1% (natural) Most HPHT			N in single substitutional sites
IIa	~2%	~220 nm	2.5-6 μm transparent >6 μm	Very low N level
IIb	< 0.1%			Extremely low N level; semiconducting (Boron acceptors)

Table II.1: classification of natural diamond crystals (From [6])

Naturally occurring diamond has been divided into four broad categories or types. Type I diamonds contain some nitrogen impurities and exhibit a characteristic absorption edge at ~300 nm. Type Ia contain mainly nitrogen aggregates and account for most of natural diamonds (~98%) while Ib contain mainly single substitutional nitrogen and represent ~0.1%. Type II diamonds are characterised by very low levels of nitrogen, leading to a near bandgap absorption edge at ~220 nm and represent ~2% of natural diamonds. Type IIa refers to the very rare ultra pure diamonds while type IIb contains detectable levels of boron, which has been shown to give rise to the *p*-type semiconductive behaviour [10]. Type IIb diamonds are naturally extremely rare.

II.3.2 Synthetic diamond

(i) High Pressure High Temperature synthesis

Earlier work on diamond synthesis reproduced in the lab the conditions of geological formation of diamond by applying high pressures and high temperatures. The General Electric company, in 1955, was first to announce successful synthesis of diamond using this high pressure, high temperature (HPHT) process [11].

The phase diagram of carbon (see figure II.6) gives an insight to understand the HPHT process. The boundary between the graphite and the diamond stable regions suggests that by applying high pressures to graphite at a given temperature, one may obtain diamond. However figure II.6 also shows that diamond is not thermodynamically stable at room temperature and at atmospheric pressure. Yet this metastable form of carbon does not turn back into graphite and diamond can be considered as kinetically stable under ambient conditions [12]. This happens because the carbon-carbon bonds in both diamond and graphite are too strong to be broken unless sufficient thermal energy is provided. In fact diamond begins to revert to graphite at temperature above 1800 K. This condition implies that the reverse process, i.e. conversion of graphite into diamond is only possible at

temperatures greater than 1800 K. At such temperatures, a pressure of 60 Kbar will be required.

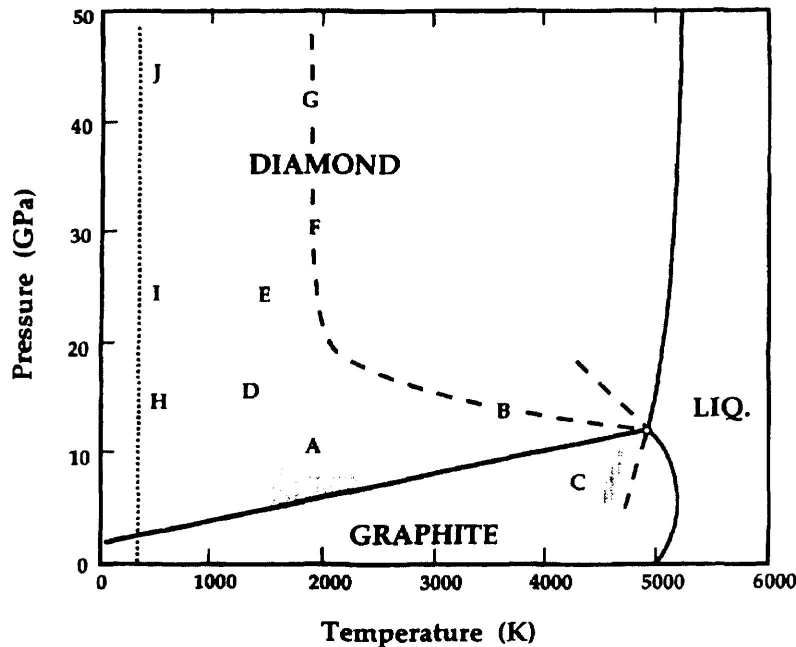

Figure II.6 P, T phase and transition diagram for carbon. Solid lines represent equilibrium phase boundaries. A: commercial synthesis of diamond from graphite by catalysis; B: rapid solid-phase graphite to diamond synthesis; C: fast transformation of diamond to graphite; D: hexagonal graphite to hexagonal diamond synthesis; E: shock compression graphite to hexagonal diamond synthesis; F: shock compression graphite to cubic diamond synthesis; B, F, G: graphite or hexagonal diamond to cubic diamond synthesis; H, I, J: compressed graphite acquires diamond-like properties, but reverts to graphite upon release of pressure. (After [1,13])

Direct conversion of graphite to diamond proved to be very difficult since both high temperatures and pressures were required. The General electric company used another alternative to circumvent this problem and achieved successful synthesis of diamond by dissolving carbonaceous material in molten iron or nickel such that some of the dissolved

carbon crystallised out as diamond [6]. The metal in such process acts as a solvent/catalyst for diamond synthesis. The announcement of General Electric's successful synthesis was followed by a period of considerable activity. It is now possible to produce large crystals of good quality and the world production is now three times the production of diamond from the earth [6].

(ii) Chemical Vapour Deposition synthesis

Both natural and synthetic diamonds are formed under high pressures and high temperatures conditions. However it is possible to crystallise diamond in a pressure-temperature regime where diamond is thermodynamically unstable with respect to graphite, i.e., at pressures less than one atmosphere and temperatures less than 1373K [12]. Diamond growth in the metastable phase can be traced back to Eversole [14], Angus *et al.* [15], and Derjaguin *et al.* [16]. Eversole was the first to grow diamond from a vapour source by introducing methane at low pressure (0.15 torr) over fine diamond powder at temperatures around 1300K. Angus and co-workers have further investigated this approach by conducting more experiments. Although diamond had been grown from a vapour, the low deposition rate (<0.1 μm/h) and the co-deposition of graphitic carbon reported in the above work prevented worldwide interest at the time. At about the same period, Derjaguin *et al.*, were able to grow diamond whiskers from a carbonaceous gas at approximately atmospheric pressure [16]. These Russian scientists continued to develop the method in the late 1970's and early 1980's and made a breakthrough in low-pressure synthesis of diamond in 1981 by adding atomic hydrogen to the methane gas [17]. The effect of atomic hydrogen increased the growth rate of diamond while suppressing the deposition of graphite. An extensive research programme at the National Institute for Research in Inorganic Materials (NIRIM) in Japan followed in the 1980's, which resulted in a variety of new techniques for the growth of diamond at low pressure to emerge. This has resulted in the field generally known as Chemical Vapour Deposition (CVD) of diamond and has been

the most popular and successful method to date of producing diamond in this thermodynamic regime.

The formation of diamond in the metastable phase is a competing process between the formation of diamond and graphite since there is only a small free energy difference between these two carbon forms; around 0.03 eV at 298K and atmospheric pressure. Hence, there is always a finite probability that both phases will form during CVD synthesis. To promote preferentially the formation of diamond to the detriment of that of graphite, conditions must be provided ensuring that the growth of diamond is favoured and that graphite and other non-diamond carbon form with a low probability. This requirement has been considered in terms of thermodynamic, chemical and kinetic factors. Koba [18] has listed the important features:

(i) Bulk transport and subsequent activation of a carbon-containing reactant gas to produce species suitable for the formation of diamond precursors.

(ii) The presence of a driving force to transport the activated gas phase species to the substrate surface, followed by the adsorption of precursors onto the growth surface.

(iii) Diffusion of the precursors to the growth sites and reaction of the film precursors for the incorporation of film constituents so that the film can grow form the surface away.

(iv) The active presence of a species which suppresses the formation of any non-sp^3 species to ensure that only diamond carbon crystallises; usually this requirement is satisfied by a high concentration of atomic hydrogen which performs a number of critical roles in the growth process; including the preferential etching of graphite (~50 times faster than diamond) [19], prevention of the reconstruction of the diamond surface into non-diamond elements and creation of free radical sites on the hydrogen saturated growth surface providing a route for continued growth of the sp^3 surface [20].

Figure II.7 below shows a schematic of a generic diamond CVD process using a mixture of methane and hydrogen gases [21].

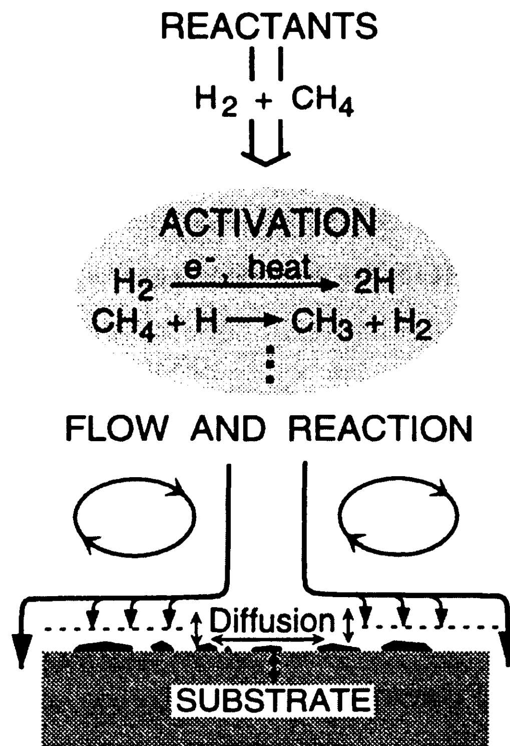

Figure II.7: A schematic showing the principal elements in the diamond CVD process: flow of reactants into the reactor, activation of the reactants by thermal and plasma processes, reaction and transport of the species to the growing surface, and surface chemical processes depositing diamond and other forms of carbon. (Reproduced from [21])

The CVD growth of diamond can be simplified and broken down into three stages:

(i) Formation of atomic hydrogen and development of gas phase chemistry by decomposing carbon-containing molecules

(ii) Nucleation of diamond on the surface of the substrate

(iii) Growth of diamond via surface chemistry

The first stage is accomplished by providing enough energy to the gas mixture. The energy supplied breaks the bonds of molecular hydrogen to produce a high concentration of atomic hydrogen. Atomic hydrogen being highly reactive and unstable reacts with either a hydrogen molecule or a gas phase hydrocarbon molecule (e.g. CH_4 or C_2H_6) resulting in hydrogen abstraction. This gives rise to either a molecular hydrogen or a highly reactive intermediate (free radical) which may undergo chemical reactions. Diamond nucleation is believed to begin with the adsorption of these free radicals to the surface. Further reactions follow where atomic hydrogen abstracts the hydrogen atoms from the radicals attached to the surface. This allows other free radicals to link to the existing ones on the surface so that the film can grow. Other reaction intermediates have been identified by Sunkara *et al.* [22] but Angus [23] summarised the process when the source gas is a mixture of methane and hydrogen:

1. Generation of free radicals in the gas phase

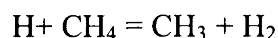

$$H + CH_4 = CH_3 + H_2$$

2. Addition of hydrogen to a bare diamond surface

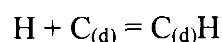

$$H + C_{(d)} = C_{(d)}H$$

3. Abstraction of a hydrogen from a hydrogenated surface to form a surface free radical

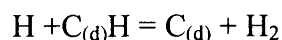

$$H + C_{(d)}H = C_{(d)} + H_2$$

4. Attachment of a methyl radical to the diamond surface

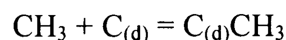

$$CH_3 + C_{(d)} = C_{(d)}CH_3$$

The sum of the above elementary reactions results in the attachment of one carbon atom to the diamond surface in the form of a methyl group.

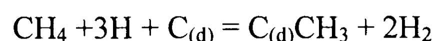

$$CH_4 + 3H + C_{(d)} = C_{(d)}CH_3 + 2H_2$$

Further abstraction reactions and rearrangements caused the attached carbon to become fully incorporated into the growing diamond crystal [24]. The net result is the conversion of stable gas phase species (e.g. methane into diamond) by a series of steps each of which are

thermodynamically favoured. For all these processes, an additional important role of atomic hydrogen is to allow graphite to be etched away from the surface as the film grows, as mentioned earlier.

It is to be noted that, at present, the growth of diamond on non-diamond substrates (heteroepitaxy), such as silicon (Si), by CVD processes leads to polycrystalline diamond films. Single crystal layers can only be obtained when single crystal diamond (natural or synthetic diamond) is used as the substrate (homoepitaxy) material.

II.4. CVD GROWTH TECHNIQUES

Many CVD techniques are able to satisfy the requirements needed to ensure the preferential growth of diamond under metastable conditions. These have been reviewed extensively in the literature (e.g. Zhu *et al.* [12], Bachmann [25]) and the most common of these may be divided into three categories:

(i) Hot Filament CVD
(ii) Plasma Enhanced CVD
(iii) Combustion flame CVD

II.4.1 Hot Filament Chemical Vapour deposition (HFCVD)

Originally reported by Matsumoto *et al.* [26], hot filament CVD (HFCVD) is one of the simplest techniques used to grow diamond. A schematic diagram is given in figure II.8. In this experimental set-up, a gas mixture of typically 1% hydrocarbon (most commonly methane) in hydrogen is admitted at a rate of ~100 sccm (standard cubic cm per minute) in a chamber where a refractory metal (e.g. tantalum or tungsten) is heated to ~2000°C. The thermal energy provided by the hot filament dissociates the molecular hydrogen into atomic hydrogen. At these temperatures, the dissociation efficiency is approximately 10% [27],

yielding a low concentration of atomic hydrogen and so low pressures (~40-100 Torr) are used to enhance the transport of atomic hydrogen. Unfortunately these low pressures result in low growth rates of 1-10 $\mu m.h^{-1}$. The atomic hydrogen and free radicals, which are formed near the hot filament, require the substrate to be placed near the filament (~1 cm). One of the major problems associated with HFCVD has been practical difficulties concerning the filament. Conversion of the refractory metal filament into a carbide leads to brittle fracture and failure. Contamination of the film with filament metal can also occur and is detrimental to the semiconducting properties the resulting film. However this technique presents a few advantages. It is relatively inexpensive, it is ideal for scale-up and the method offers the possibility for the fabrication of three-dimensional structures such as coating of fibres by following filaments round the substrates [28].

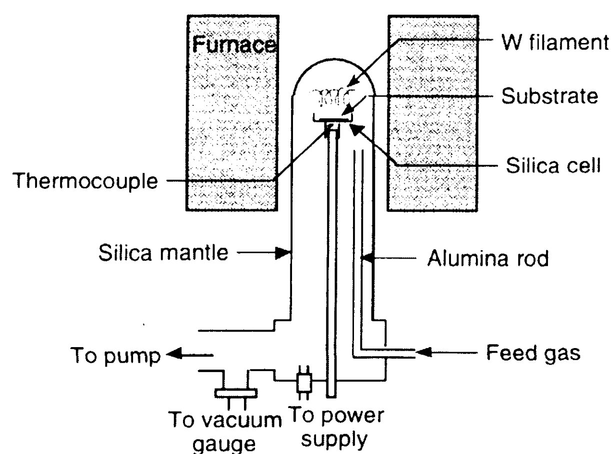

Figure II.8: Schematic of a HFCVD apparatus (Redrawn from [26]).

II.4.2 Plasma Enhanced CVD (PECVD)

Spitsyn *et al.* have suggested the use of electrical discharges as a mean to produce atomic hydrogen and hydrocarbon free radicals [17]. Various plasma systems have been developed including microwave (MW), radio frequency (RF) and direct current (DC). Plasma systems

may further be subdivided into low (<200 Torr) and high (200-760 Torr) pressure techniques. At the higher pressures, greater power levels are required to maintain the existence of the plasma, resulting in a much higher gas temperature or "thermal" plasmas where full dissociation of molecules into atoms and radicals may occur. Within such environment, higher growth rates are achievable [25].

(i) Microwave plasma enhanced chemical vapour deposition (MWPECVD)

The use of the 2.45 GHz high frequency radiation has become one of the most common and successful methods for plasma excitation [29]. Figure II.9 shows various equipment set-ups. The choice of this specific frequency was mainly driven by the industrial availability of components, which comply with national regulations. Further, 2.45 GHz is particularly convenient as the ~12 cm wavelength leads to waveguides and components which are reasonably compact, while a cheap supply of suitable magnetron power sources are available due to the use of this frequency for domestic microwave ovens. This technique was first developed by the NIRIM group in a tubular silica chamber form (see figure II.9(a)). Typical deposition conditions are similar to that of the HFCVD technique, e.g. pressure in the range 40-100 Torr, substrate temperature ~800°C, 1% CH_4 in H_2, total gas flow ~100 sccm; under these conditions with 1 kW microwave power growth rates of 1-5 $\mu m.h^{-1}$ can be achieved. The tubular design, which places the substrate in direct path of the microwaves, is relatively easy and cheap to set-up. However it suffers from problems of reliability and silica contamination of the deposited film due to the reaction of the plasma with the silica tube. This system has been improved by Bachmann [25] with the 'Bell jar' reactor (see figure II.9(b)), which was subsequently developed into the well known ASTeX (Applied Science and Technology, Woburn, MA, USA) High Pressure Microwave System. The 'Bell jar' design is a resonant cavity, which allows growth over larger areas and significantly reduces wall contamination in the grown film. Another interesting alternative is electron cyclotron resonance (ECR) systems in which the frequency of the electron gyration is equal to that of that of the microwaves. A typical set-up is shown in figure

II.9(c). Kawarada *et al.* have examined 2.45 GHz ECR systems as an alternative route to achieving large, uniform high density plasmas compared with resonant cavities [30]. However at pressures of less than 0.1 mbar, where true ECR conditions are satisfied, deposition rates and crystal sizes observed were rather poor and it has been concluded that such systems although showing initial promise are best suited to the deposition of mixed phase films for the use of low wear coatings [31].

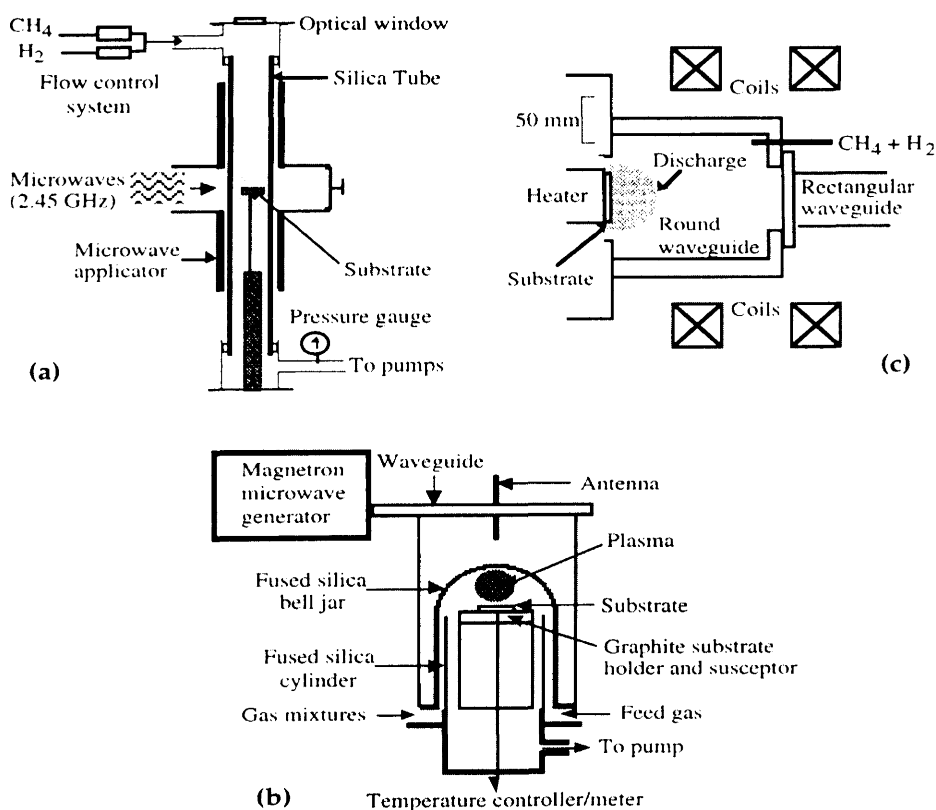

Figure II.9: Schematic of a microwave plasma CVD systems showing (a) NIRIM tubular, (b) Bell jar and (c) ECR coupled arrangements (Redrawn from [12]).

(ii) Radio frequency plasma chemical vapour deposition (RFCVD)

Radio frequency plasma technology has been studied as an attractive possibility to grow diamond at low pressures. Zhu *et al.* have reported that low-pressure plasmas were produced using either capacitively or inductively coupled systems (see figure II.10(a)) at frequencies between 100 Hz and 13.56 GHz [12]. Other than the frequency, the deposition conditions used were similar to those utilised for MWPECVD and led to similar growth rates. However, the quality of the deposited film was judged to be inferior [25].

More recently, Matsumoto *et al.* developed a high power technique (see figure II.10(b)) to obtain high growth rates (60-180 $\mu m.h^{-1}$) by introducing methane at much higher concentration than in other CVD techniques (up to 10%) [32]. In this technique, RF induction heating was utilized to obtain a thermal plasma of the precursor gas mixture at RF powers of 40-80 kW using frequencies 3-30 MHz. However, the sophistication, high power consumption and large gas volume requirements are real drawbacks of this system.

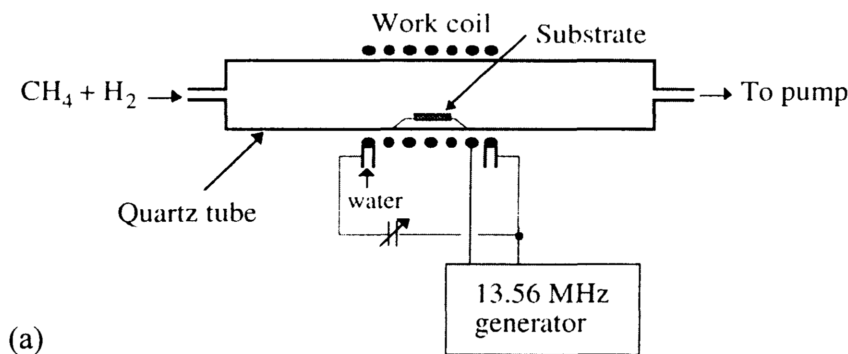

Figure II.10: Schematic of (a) an inductive RF plasma CVD apparatus and (b) RF thermal plasma CVD system (Redrawn from [32]).

(iii) Direct current plasma chemical vapour deposition (DCCVD)

The easiest way to form an electrical discharge at low pressures for the production of atomic hydrogen and hydrocarbon free radicals is probably a direct current (DC) plasma discharge. By applying a high DC voltage and high current density (1 kV and 4 A/cm^2) between two parallel electrodes in a relatively high gas pressure (200 Torr) (see figure II.11(a)), Suzuki *et al.* [33] achieved high growth rates (~20 μm.h^{-1}). In this system, the substrate must be mounted on the anode with a temperature above 600°C to produce diamond. If the substrate is mounted on the cathode amorphous carbon is preferentially formed. There are several modifications to using DC glow discharges to grow diamond but the major one is probably the DC plasma jet introduced by Kurihara *et al.* [34] as shown in figure II.11(b) where thermal plasmas with temperatures greater than 4000°C are created, thus allowing complete gas dissociation. In this design, the gases are heated and decomposed by an arc discharge between two cylindrically symmetrical electrodes. This creates a rapid expansion of the gases, thus causing them to rush out of the orifice towards the substrate in a jet, hence the name of this technique – DC plasma jet. The main advantage of DCCVD is the high deposition rate that can be achieved. In addition, diamond films can be deposited on substrate surfaces with mechanical pre-treatments. However problems still exist with small deposition areas (~10 mm in diameter), poor temperature control due to extremely high gas temperatures and film non-uniformity.

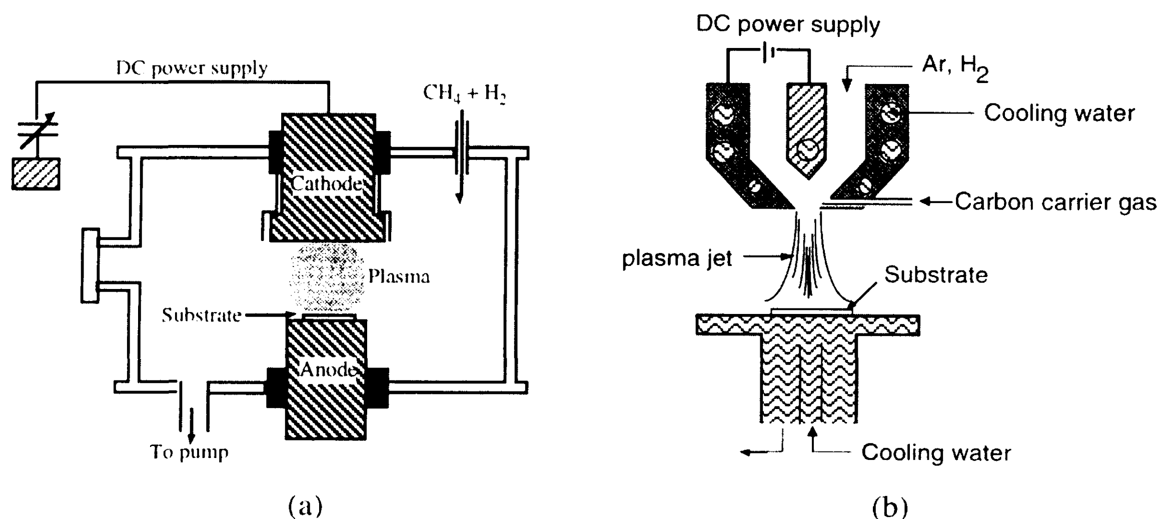

Figure II.11: Schematic diagram of (a) an direct current (DC) plasma CVD reactor (From [33]) and (b) a direct current plasma jet system (Redrawn from [32]).

II.4.3 Combustion flame CVD

Combustion flame CVD is a method developed by Hirose *et al.* [35] that involves the burning of various hydrocarbons at atmospheric pressures. It utilises a simple welding torch and a water-cooled substrate holder; a typical set-up is shown in figure II.12. Diamond growth has been observed with an oxy-acetylene flame but other gases such as methane, propane or ethylene have also produced diamond films at lower rates when burned with oxygen in air [36]. Because of its high gas pressure and high gas temperature, the flame can be regarded as a thermal plasma, although the degree of ionisation might be low. For the same reason, much of the hydrogen and oxygen liberated in the combustion process is present in the form of atomic species together with carbon species which come from the dissociation of acetylene. The conditions are then met for diamond growth to take place in the flame region. The ratio of acetylene to oxygen is critical for the formation of the oxy-acetylene flame and for the deposition of diamond and is around unity. The substrate is typically placed in the inner flame rather than in the outer flame because the outer flame is an oxidising environment and thus would convert carbon into gaseous carbon dioxide. On

the other hand, the inner flame is a carbon rich, reducing environment which also includes a large concentration and variety of excited species, thereby allowing diamond growth. The gas temperatures are of the order of 3000°C, while the substrate temperature is maintained at 800-1000°C. High growth rates of up to 140 $\mu m.h^{-1}$ can obtained in typical combustion flame systems. However, this method suffers from high substrate temperature, poor film uniformity and poor process stability.

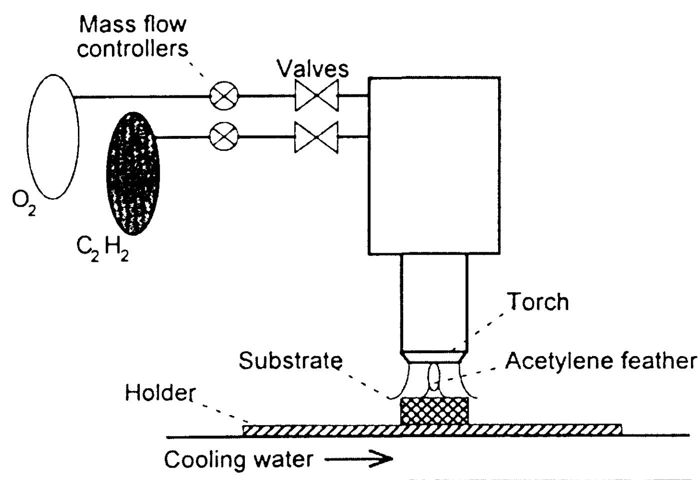

Figure II.12: Schematic of a typical combustion flame CVD apparatus (Redrawn from [12]).

II.4.4 Comparison of CVD diamond films

Bachmann has reviewed the status of many existing diamond CVD techniques [37]. A summary is given here in table II.2. The variety of techniques available to grow diamond films offers multiple choices for the deposition method, each having its strengths and weaknesses. However it is the performance requirements of the diamond films, which may include a combination of good substrate adhesion, high optical transparency, low impurity content and high thermal conductivity together with economical consideration that will ultimately dictate the deposition method.

Technique	Rate ($\mu m.h^{-1}$)	Area (cm^{-2})	Quality	Advantages	Drawbacks
Hot filament	0.3-2	100	+++	simple large area	contamination stability
Combustion flame	30-100	<1	+++	simple	area stability
DC discharge (low P)	<0.1	70	+	simple large area	quality rate
DC discharge (medium P)	20-250	<2	+++	rate quality	area
DC plasma jet	930	<2	+++	highest rate quality	area, stability homogeneity
RF (low P)	<0.1	?	-/+	Scale-up	quality, rate
RF (thermal)	180	2	+++		area, stability homogeneity
Microwave (2.45 GHz)	1 (low P) 30 (high P)	40	+++	quality stability	rate area
Microwave (ECR, 2.45 GHz)	0.1	>40	-/+	area low P	quality rate

Table II.2: Comparison of CVD techniques (Reproduced from [37]).

II.5. NUCLEATION MECHANISMS

All the CVD growth methods described above have invariably led to deposited thin films on non-diamond substrates to be polycrystalline in nature, whereas single crystal diamond has been observed to grow on diamond substrates. In either case, a detailed understanding and an effective control of the fundamental phenomena associated with diamond nucleation and growth are required. This is essential for optimising the diamond film properties

necessary for targeted application such as grain size, orientation, transparency, adhesion, and roughness.

The investigation diamond of nucleation not only leads to insights necessary for the controlled growth of diamond films suitable for various applications, but it can also provide insight into the mechanisms of diamond growth. To date, the understanding of diamond nucleation is very limited. The current status is given below.

II.5.1 Gas phase nucleation

Homogeneous nucleation in the gas phase and its contribution to different deposition processes are poorly understood. However, there is evidence that, at least in some cases, diamond can be nucleated homogeneously in the gas phase. Derjaguin *et al.* [38] presented theoretical arguments where homogenous nucleation is possible in the gas phase whilst Matsumoto *et al.* [39] suggested that hydrocarbon cage molecules such as adamantine, bicyclooctane, texacyclopentadecane and dodecahedron are possible embryos for homogeneous nucleation of diamond, as all these cage compounds possess the diamond unit structure. The diamond lattice should then be generated by simple abstraction of hydrogen and addition of carbon. However, thermodynamic equilibrium calculations revealed that such low-molecular-weight hydrocarbons were not stable at high temperatures (over 600°C) in the harsh environment associated with diamond CVD [40,41].

A limited number of experiments have been conducted to examine homogeneous nucleation of diamond in the gas phase at atmospheric and sub-atmospheric pressures [42-44]. The number of diamond particles collected from the gas phase is very small compared with typical nucleation densities observed on different substrate surfaces. Therefore, the homogeneous nucleation mechanism cannot account for the large variation of nucleation densities observed on different substrate materials. It has been speculated that the nuclei formed in the gas phase may reach the growing surface and increase the surface nucleation

density. However, whether and how the diamond particles formed in the gas phase could serve as seeds on the substrate surface for subsequent growth of diamond film remain unknown.

II.5.2 Surface nucleation

A diamond film must first nucleate on a substrate before heteroepitaxial growth of any sort can be considered. The nucleation mechanisms of diamond on non-diamond substrates are not well understood and in general the process is difficult. These mechanisms are the subject of considerable experimental and theoretical work and various possibilities have been considered. The difficulty with nucleation is probably due to a combination of the high surface energy of diamond compared to other available substrates, low sticking probability for the diamond precursors and competition from other non-diamond phases which would also like to grow on the substrate.

Nucleation of diamond on non-diamond substrates has been classified into nucleation on an intermediate layer of diamond-like amorphous carbon [45], metal carbides [46] or graphite [47] formed at the substrate surface by chemical interactions with the activated gas species and the surface during the incubation period. These intermediate layers provide nucleation sites for diamond crystallite growth. Hence they enhance the diamond nucleation density on non-diamond substrates and offer an opportunity for controlling the morphology, orientation and texture of diamond films. The thickness of such layers ranges from several angstroms, e.g. 6Å for carbon on platinum [48], to a few micrometers, e.g. 1.5-3 μm for Mo_2C on Mo [49]. The representative nucleation mechanisms proposed in the published literature are summarized in figure II.13 [50].

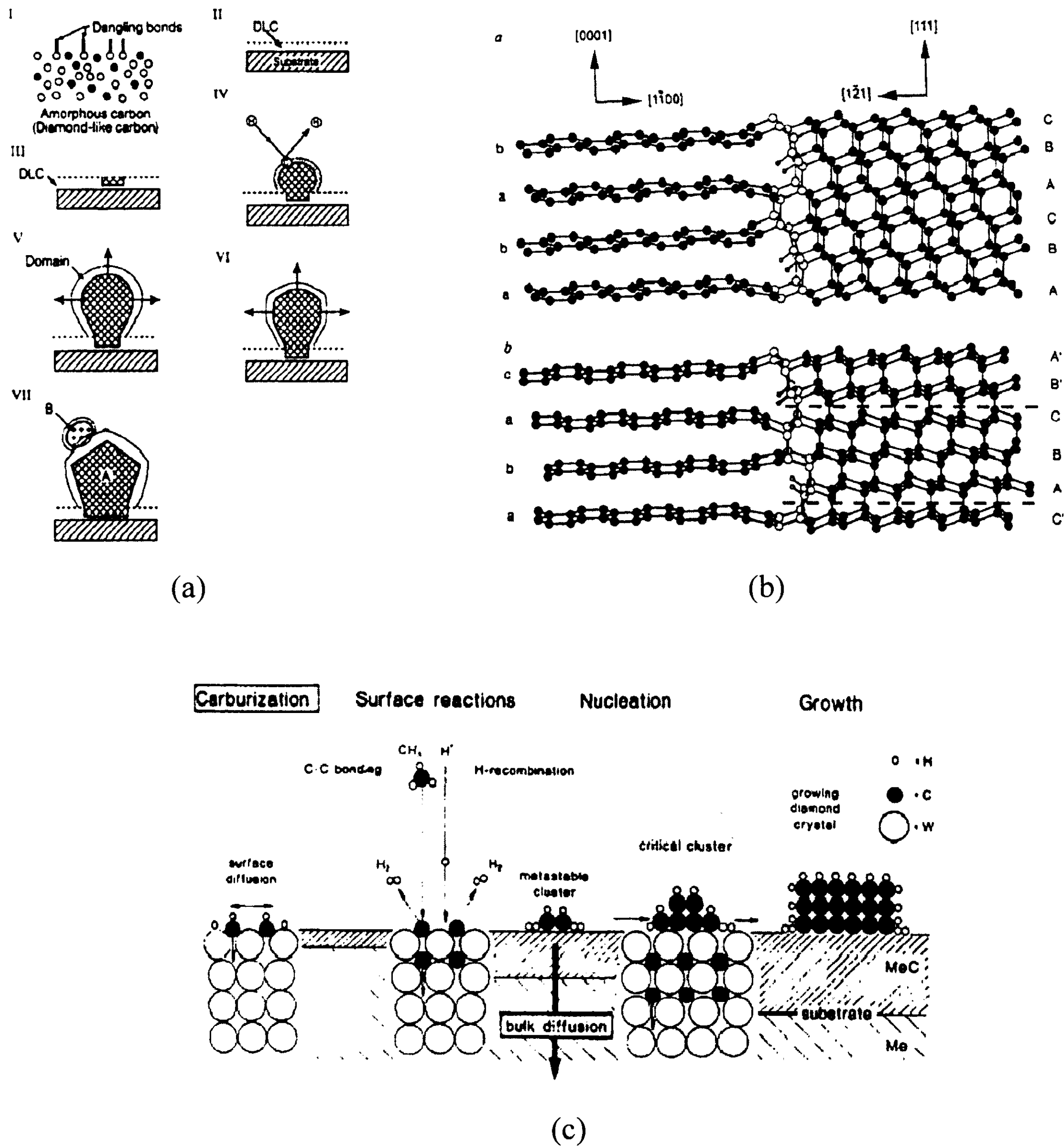

Figure II.13 Summary of nucleation mechanisms thought to account for nucleation of diamond on most non-diamond substrates: (a) on a DLC intermediate layer: (I) formation of carbon clusters and change in bonding structure from sp^1 to sp^2; (II) sp^2 converts to sp^3, (III) amorphous phase crystallises; (IV-VI) growth and faceting of diamond crystals; (VII) secondary nucleation and growth. (b) On a graphite intermediate layer: initial condensation of graphite and subsequent hydrogenation of the $\{1\bar{1}00\}$ prism planes along edges of graphite particles; diamond nucleation at emerging stacking fault follows – the

interface between the graphite layer and the diamond nuclei is almost perfect. Upper: cubic diamond on perfect hexagonal graphite, lower: twinned diamond nucleus adjoining a graphite stacking fault. Twin boundaries are indicated by dash lines, H-atoms by open circles, C-atoms by solid circles. The larger opened circle represent the initial nucleus formed at the interface by tying together the graphite layer with tetrahedrally bonded C atoms. (c) On a carbide intermediate layer: carburisation consumes all available C to form a carbide surface layer; C surface concentration below diamond nucleation minimum; with increasing carbide layer thickness, the C transport rate decreases and the C surface concentration increases; diamond nucleus forms when either surface C concentration reaches a critical level or a surface C cluster attains a critical size (Adapted from [50]).

Nucleation on an intermediate layer of diamond-like carbon (DLC) carbon layer has been studied by Singh [45]. It was found that small diamond nanocrystallites were embedded into the diamond-like amorphous carbon (a-C) layer from which large diamond crystallites were observed to grow. It was proposed that the diamond nanocrystallites are formed as a result of direct transformation of the a-C layer into diamond, with the intermediate layer providing nucleation sites. Figure II.13(a) depicts this nucleation mechanism. In step I, carbon clusters are formed on the substrate surface, and a change in the bonding structure from sp^1 to sp^2 takes place. In step II, sp^2-bonded carbon atoms are converted into a relatively stable network of sp^3-bonded carbon. The continuous rain of atomic hydrogen and activated hydrocarbons impinging on the surface provides enough energy for the sp^1 to sp^2 to sp^3 conversion. At the same time, etching of unstable phases (sp^1 and sp^2), which is ten times faster than etching of stable phase (sp^3), promotes and stabilizes the sp^3 phase. In step III, a bonding state in the carbon network transits from a disordered domain to diamond– crystallisation in the amorphous layer occurs. The crystallised regions then act as nuclei for the subsequent growth of diamond. In step IV to VI, diamond growth takes place. Carbon atoms added into the surface (step IV) diffuse inwards by a solid-state diffusion process. The initial diamond shape was found to be hemispherical (step IV). Once a

diamond microcrystal reaches a critical size (step V), it will acquire a faceted crystallographic shape characterised by defects (VI). In step VII, secondary nucleation takes place as a result of the concentration fluctuation on the surface of the diamond crystal. This fluctuation leads to an uneven surface of the disordered domain. Once the thickness of the disordered domain exceeds a critical value, there will not be enough energy or time available for the carbon atoms to diffuse into the diamond crystal, leading to secondary nucleation on the surface.

Nucleation of diamond on an intermediate layer of graphite has been observed on various substrates. Experiments on nickel and platinum in HFCVD [48], on silicon [51] and copper [52] in MWPACVD showed that there was an initial period during which a graphite deposit formed. This deposit subsequently disappeared, and the final deposit contained only polycrystalline diamond. On the basis of these experimental results, Lambracht *et al.* [53] proposed a detailed nucleation mechanism, as shown schematically in figure II.13(b). It was suggested that graphite initially condenses on the substrate surface and the $\{1\bar{1}00\}$ prism planes are subsequently hydrogenated. Diamond nuclei grow preferentially on the prism planes of graphite, with kinetically preferential nucleation at the emerging graphite stacking faults, and with an almost perfect interface between graphite and the diamond nuclei. Etching of graphite occurs simultaneously during diamond nucleation. Atomic hydrogen, which plays and important role, terminates the dangling surface bonds and stabilizes sp^3 nuclei with repect to sp^2 nuclei, but it also serves as a reactive solvent which permits the conversion of graphite nuclei into diamond nuclei, hence circumventing the large activation barrier between graphite and diamond. Lambracht *et al.* [53] stated this detailed nucleation mechanism is the dominant channel for the spontaneous nucleation of new independent diamond crystals in the absence of pre-existing diamond seeds.

Nucleation of diamond on an intermediate layer of metal carbide was observed by Badazian *et al.* [54] when diamond was grown on silicon (Si). The authors suggested that a β-SiC buffer layer is formed prior the nucleation of diamond, and that the nucleation follows on

the surface of the carbide layer. This is supported by many growth experiments performed either on diamond particles/films on Si substrate in HFCVD and MPCVD [46], which showed that the Si surface was indeed transformed to SiC leading to diamond growth with diamond nucleation occurring on a SiC intermediate layer. An AFM study provided further evidence for the formation of this SiC layer [55]. The formation of a carbide layer has also been observed when other substrates materials were used. Joffreau *et al.* [56] conducted systematic studies of diamond growth on carbide-forming refractory metals, and observed that diamond nucleation occurred only after the formation of a thin carbide layer. Lux and Haubner [57] subsequently proposed a model to elucidate the mechanism governing the nucleation process on a carbide-forming substrate as shown in figure II.13(c). It was suggested that carbon dissolved initially into the substrate, resulting in the formation of a stable carbide. Diamond nucleation is believed to occur on the carbide layer when the carbon concentration on the surface reaches its saturation value. Lux and Haubner [57] also compared the time evolution of diamond nucleation densities on Ti, Hf, Nb, Ta, Mo and W, and found that the difference in the nucleation densities was related to the diffusion of carbon in the respective substrates. The incubation period for nucleation is the shortest on metal that can most rapidly achieve a super-saturation of carbon on the surfaces.

It should be noted that the formation of these intermediate layers is a step in the non-epitaxial nucleation processes of diamond on non-diamond substrates, but this alone is not sufficient for nucleation to occur [58]. Carbon saturation of the substrate surface and defects or high-energy sites (unsatisfied valences), present in the intermediate layers mentioned above, are the two conditions that need to be satisfied for non-epitaxial diamond nucleation.

II.6 GROWTH OF DIAMOND BY CVD METHODS

Compared with the situation for nucleation a clearer understanding has been achieved for the growth of diamond under CVD conditions. Frank-van der Merwe two-dimensional layer-by-layer growth is the growth mode of diamond homoepitaxy and heteroepitaxy [59]. On the other hand, Volmer-Weber growth, which leads to the production of continuous film by growing out three dimension nucleation sites until they coalesce [60], is the growth mode of polycrystalline diamond films on non-diamond substrates. Clearly, if the nucleation density is low this results in rough films, furthermore growth is very slow until the nuclei coalesce and the growth mode changes to a two-dimensional Frank-van der Merwe layer-by-layer growth mode. To obtain reasonably smooth films and respectable growth rates, a high nucleation density is required and this means that some type of nucleation enhancement process must be employed. The most important deposition parameters responsible for the quality of the diamond films are discussed below.

II.6.1 Substrate materials

The substrate material will determine the morphology and the texture of the diamond film. While single crystal diamond growth has been observed solely on single crystal diamond substrates, diamond films grown on polycrystalline diamond or non-diamond substrates are always polycrystalline in nature. In the latter case, substrates materials may be classified into three major groups in terms of carbon/substrate interactions, as listed in table II.3.

Little or no solubility or reaction	Diamond, graphite, carbons Cu, Ag, Au, Sn, Pb, etc.
C-diffusion only, C dissolves in metal-carbide mixed crystals	Pt, Pd, Rh, etc.
Carbide formation	
metallic	Ti, Zr, Hf, V, Nb, Ta, Cr, Mo, W, Fe, Co, Ni (metastable)
covalent	B, Si, etc.
ionic	Al, Y, rare earth metals, etc.

Table II.3: Classification of substrate materials (From [57])

Diamond surfaces or particles provide the best nucleation potential [61] while research efforts on heteroepitaxy showed that nucleation readily occurs on cubic boron nitride (c-BN) [62]. It was also found that diamond nucleation rates on stable carbide-forming substrates such as Si, Mo and W are one to two orders of magnitude higher than on non-carbide-forming substrates (Cu and Au) [17]. Among carbide-forming substrates (Si, Mo, Al, Ni and Ti), the nucleation density on Mo is about one order of magnitude higher than on all other substrates under the same deposition conditions [63]. Nucleation rates on polycrystalline substrates have been found to be several times higher than on single crystal substrates of the same material after identical surface pre-treatment. Refractory metal carbides (TaC, WC and Mo_2C) and some covalent carbides (SiC and B_4C) have a positive effect on nucleation, while the effect of ionic carbides (Al_4C_3 and liquid salts) on nucleation needs yet to be known. Nucleation occurs readily on substrates forming amorphous diamond-like carbon (mostly Mo and Si) without any scratching pre-treatment.

II.6.2 Effect of H_2, N_2, O_2 and noble gases

The reaction gases used in low-pressure diamond synthesis methods contains relatively low concentrations of volatile carbon compounds with a high excess of hydrogen. Activation of such a gas mixture is carried out to obtain the highest possible concentration of atomic hydrogen. Atomic hydrogen plays a major role in mediating rates and in maintaining a proper surface for growth. Low molecular weight hydrocarbon species (e.g. CH_3 and C_2H_x) are believed to be responsible for the extension of the diamond lattice and a number of hydrogen-carbon compounds have already been used successfully as carbon sources.

The essential features of the synthesis is characterised by the following two reactions and occur simultaneously: (1) the decomposition reaction, which consists of a normal pyrolitic hydrocarbon chemical vapor deposition reaction; (2) the etching reaction by the atomic hydrogen. This prevents the formation of all other weakly bonded solid carbon compounds except diamond.

The presence of a small amount of nitrogen in the CH_4/H_2 gas mixture is not harmful. But the presence of both nitrogen and oxygen seems to be detrimental. In this case, due to the gas activation, NO_x compounds can react with the atomic hydrogen and reduce its concentration. Nitrogen as an impurity leads to a complete change in the texture and surface morphology [64]. However, oxygen additions to the gas mixture without nitrogen are probably not harmful at all and can even have positive effects [65]. The addition of small amounts of oxygen leads to the formation of transparent diamond crystals due to the reduction of crystal defects [66].

Argon or other heavier noble gases can effectively increase the electron density of the plasma that promotes the equilibrium of hydrogen atoms and ions and improves the properties of the deposited films [67]. Similar to nitrogen and oxygen, these noble gases have significant effects on surface morphology and crystalline structure of diamond films.

By adjusting the noble gas/hydrogen ratio in the gas mixture, a continuous transition from micro- to nano-crystallinity was achieved [68].

II.6.3 Surface pre-treatments and nucleation enhancement

Enhancement methods, which have successfully been used to promote the nucleation of diamond, include scratching, seeding, electrical biasing, covering/coating, ion implantation, pulse-laser irradiation and carburization. Amongst these surface pre-treatments, ultrasonic scratching and biasing show the best efficiencies on nucleation enhancement. Nucleation on pre-treated surfaces is observed to occur primarily on carbide-rich particles or defects such as scratches, grain boundaries, particle boundaries, dislocations, electron bombardment damages, and edges of etch pits/craters [69].

Scratching with both diamond and non-diamond abrasives has been shown to enhance the nucleation density by several orders of magnitude [69]. However, diamond abrasives give the highest nucleation enhancement. Various mechanisms are thought to be responsible for this. These include seeding effects [17,70], minimisation of interfacial energy on sharp convex surfaces [71], breaking of a number of surface bonds, or the presence of a number of dangling bonds at sharp edges [72], strain field effects [73], rapid carbon saturation (fast carbide formation) at sharp edges [57], and removal of surface oxides [69]. Another possible operating mechanism for nucleation enhancement by scratching is that it produces non-volatile graphitic particles through local pyrolysis of absorbed hydrocarbons [47]. These graphitic clusters would be subsequently hydrogenated in the atomic-hydrogen environment under the typical CVD conditions to form the precursor molecules. Scratching methods include wet and dry abrasion and ultrasonic agitation in a suspension of the abrasive material. Experimentally, it was shown that the nucleation density decreases with increasing particle size of diamond abrasive paste in the polishing pre-treatment while the adverse effect was observed in the ultrasonic scratching pre-treatment [69].

Seeding is a method that has been investigated to enhance nucleation. Diamond, Si, Al_2O_3 or SiC have been seeded on various substrates. The residual diamond particles on the substrate surface are thought to act as the predominant nucleation sites and diamond growth then occurs by means of homoepitaxy on these seed particles [70]. The nucleation density was found to be linearly proportional to the diamond seed particle density, being approximately one-tenth of the seed particle density.

Electrically biasing the substrate has been effective to increase the nucleation of diamond because biasing the substrate helps to reduce and suppress oxide formation on the substrate surface, remove the native oxide, and overcome the energy barrier for the formation of stable diamond nuclei by more effectively activating the substrate surface and/or increasing the flux and mobility of adatoms [58,74]. In DCCVD and HFCVD [33,75], positive substrate biasing was effectively employed to increase nucleation of diamond, while in MWPECVD both positive and negative biasing enhanced diamond nucleation [74].

To improve nucleation, substrate surface covering has been investigated. Graphite fibers/clusters or films [76], thin films of metals (Fe, Ti, Mo, Ni), DLC, BN, SiC and hydrocarbon oil [77] overlayers have been tried. The nucleation enhancement with these overlayers was attributed to the physical and chemical effects associated with the changes to the substrate surface (the overlayer is said to promote carbon saturation at the substrate surface, and to provide high-energy sites or nucleation centres), and changes in the gas chemistry in the immediate vicinity of the substrate surface [76].

Another method that has been used is ion-implantation. It modifies the surface energy and the substrate structure of substrates to enhance diamond nucleation. The lattice damage (strain, amorphous disorder and twinning) created by ion implantation is deemed to be responsible for the nucleation enhancement [73]. Implantation of C^+ on Cu and As^+ on Si has enhanced diamond nucleation [52], while Ar^+ implantation on Si has decreased nucleation density [78].

Pulse-laser irradiation of thin buffer layers of a-C, WC or c-BN deposited on substrates (Cu, stainless steel, Si) has led to significant enhancement of both nucleation and adhesion of diamond films on substrates [79]. It was speculated that the irradiation converted a portion of the a-C on the surface into diamond, or resulted in the formation of a reaction product that facilitated diamond nucleation. Carburization of substrates (Mo, W, Si, Fe/Si) also led to nucleation enhancement owing to the formation of carbides and the saturation of carbon at the substrate surface.

The scratching and seeding treatments are attractive in that they are inexpensive, yield simply and effectively high nucleation densities but they are not well suited to many applications, which require extremely smooth and clean surfaces such as diamond films for electronic devices or optical windows. Furthermore, the treatment of non-planar geometries can be difficult especially if abrasives are used. As an alternative, biasing or covering/coating methods are more attractive as they lead to high nucleation densities comparable to, or even better than those achieved by seeding or scratching, without the significantly damage of the surface. However, all these methods, apart from the biasing technique, cannot lead to oriented heterogeneous nucleation or epitaxial growth on non-diamond subatsrates.

II.6.4 Deposition conditions

Deposition conditions such as substrate temperature, gas pressure, gas composition and gas activation critically influence nucleation density and rate. It has been noted that ideal deposition conditions for growth may not be optimal for nucleation. For example, in-situ surface analyses and microstructure characterisation of the diamond nucleation process on negatively biased Si substrates revealed that biasing could enhance nucleation significantly, but produces a much poorer quality diamond film if the biasing continued during the whole period of growth [58]. Similarly, the optimal values of gas pressure and substrate temperature for growth are not identical to those for nucleation.

From experience, the optimal substrate temperature, which gives a maximum nucleation density, was found to be close to 860°C. Hayashi *et al.* speculated that the overall dependence of nucleation density on substrate temperature was caused by the change in the adsorption state and surface diffusion length of growth precursors [80]. The same authors thought that the precursors were adsorbed on the substrate mainly by physical adsorption below 900°C, and predominantly by chemical adsorption above this temperature, resulting in an abrupt increase in the diffusion length of the precursors around 900°C. As a result, the capture rate of the precursors (sticking probability) on the substrate surface, and hence the nucleation rate and density, drastically increase when the substrate temperature approaches 860°C.

The effect of the filament temperature in HFCVD on nucleation is similar to that of the substrate temperature, i.e. with increasing filament temperature, the nucleation density initially increases, reaches a maximum at 2100°C and decreases thereafter [81]. The drop-off for $T > 2100^{\circ}C$ was explained by the observation that the etching of nucleation sites was enhanced with increasing filament temperature [82].

In DCCVD, a nucleation density of 6×10^{9} cm^{-2} was achieved on untreated substrates by increasing the discharge current to 1A and the cathode temperature to 1400°C [83]. It has also been suggested that diamond nucleation is enhanced by using high power densities, such as in plasma jet, or d.c. plasma discharge CVD, in which H_2 and CH_4 dissociation is promoted.

Low gas pressures (about 5 Torr), high methane concentration, and high gas flow rates have led to high nucleation densities [49,84,85]. The pressure dependence of nucleation density has been explained by the competition effect between β-SiC formation, which increases the diamond nucleation density, and atomic-hydrogen etching, which decreases the number of nucleation sites [84]. Bou *et al.* added that a high CH_4 concentration can promote carburization of the substrate surface and accelerate carbon saturation at the substrate

surface, while a high gas flow rate may increase the mass transfer of gas species to substrate surface [49]. Consequently, diamond nucleation density can be enhanced.

It has been observed that the addition of oxygen in the gas mixture can promote a much faster diamond nucleation and growth as it accelerates the saturation of carbon on the substrate surface and reduces the incubation period [86]. Further, the presence of oxygen allows low substrate temperatures, preserves a good film quality at high CH_4 concentrations, and suppresses eventual surface contamination by Si [49]. However, the downside is that by etching the nucleation sites (graphite) on substrates like Ni and Pt, diamond nucleation is suppressed when oxygen is added [48]. Work carrier out in low-pressure low-temperature MWPECVD and plasma arc jet CVD showed that the optimum oxygen concentration was 2-10% and 33% respectively [87,88].

II.7. DOPING OF DIAMOND

Doping can be achieved by incorporating certain impurity atoms which are electrically active at substitutional sites in the diamond lattice. Ideally, these impurities should be compatible in terms physical size without disturbing the lattice itself. Unwanted impurities (i.e. those that do not occupy a subsitutional site in the lattice) may generate additional defects, which can yield levels deep in the bandgap susceptible to compensate or trap the original useful carriers. The impurities must also be uniformly distributed throughout the lattice and not be segregated nor accumulated at certain sites.

II.7.1 *p*-type doping

Type IIb diamonds contain boron (B) and have been studied extensively. Brophy *et al.* conducted the first Hall measurements for type IIb diamond using indium and silver paint as ohmic conctacts [89]. They reported a *p*-type conduction with a sheet carrier

concentration of 7×10^{13} cm^{-2}, a resistivity of 760 Ωcm and a Hall mobility of 100 cm^2/Vs at room temperature. Point contact rectification confirmed the *p*-type conduction over the entire surface. Austin *et al.* [90] performed Hall measurements over a wider temperature range to determine the activation energy of the carriers in natural diamond. Based the model containing both acceptors and donor levels, a value of 0.38 eV was determined. In addition, a hole density of 1.8×10^{13} cm^{-3}, a resistivity of 270 Ωcm and a mobility of 1550 cm^2/Vs at room temperature were reported. They suspected that the impurity element responsible for this *p*-type behaviour was either attributed to boron or aluminium. Later Collins *et al.* [91], used a similar model to Austin *et al.* to determine the activation energy of the *p*-type behaviour in their IIb diamond sample. They found that the presence of boron atoms at substitutional sites create acceptor centres with an activation energy of 0.37 eV. This large ionisation barrier results in an activation of less than 1% of the dopants at room temperature [92].

To date, only boron has clearly demonstrated and established itself conclusively to be an electrically active dopant for diamond. Nonetheless, to gain the best control over the electronic properties of diamond, intentional boron doping has been investigated by several means: during the HPHT synthesis, via the gas phase, and by ion implantation.

Boron doping during HPHT synthesis was first reported by Wentorf *et al.* [93]. Boron was added to the mixture of carbon and diamond forming catalysts. The resistivity obtained was about 10^5 Ωcm with an activation energy of only 0.17 to 0.18 eV. The high resistivity value measured was thought to be caused by compensation effects from nitrogen impurities in the diamond. As nitrogen is readily incorporated into diamond, the holes due to boron atoms are annihilated when the electrons from the nitrogen donor level drop to the boron level creating no net charge in conductivity.

The main problems associated with doping during HPHT synthesis are related to the technique itself. Contamination from the catalyst and nitrogen during the process is inevitable and renders the material far from being of electronic device grade quality.

Furthermore, the process is too crude as it is difficult to control important parameters such as uniformity, thickness of the doped layer, large surface and selective area doping, which are required by device engineers.

Boron doping of diamond in the gas phase has been demonstrated by introducing diborane (B_2H_6) in the feed gas of a standard microwave plasma system [94,95]. Although diborane is the most common gaseous form of boron used in CVD processes, its high toxicity has lead to the search for non-toxic alternatives such as boron trioxide (B_2O_3) [96].
A comprehensive study of the conduction behaviour of boron doped films has been recently conducted by Lagrange *et al.* [97] over the temperature range 300-1000K. The authors pointed that the activation energy was affected by the doping concentration. This has been confirmed in other experiments where a reduction of the activation energy for samples heavily doped with boron was observed [98,99]. An activation energy of 0.368 eV was determined for concentrations below 2×10^{17} cm^{-3}, but with increasing concentration the activation energy decreased until a metallic behaviour was observed for concentrations above 3×10^{20} cm^{-3}. This reduction of activation energy was attributed to the formation of an impurity band [100-102].

Unlike with the HPHT process, good control over the boron concentration in diamond films can be achieved during CVD growth. The improvement originated from the progress of the CVD technique for depositing diamond films. It is now possible to improve the electronic properties of boron doped homoepitaxial films to surpass that of natural diamond. For example, Fox *et al.* [103] managed to deposit homoepitaxial films with Hall mobilities up to 1400 cm^2/Vs with reproducible values within the 1100-1300 cm^2/Vs range.

Ion implantation has also been investigated as a means of incorporating boron atoms into the diamond lattice. Although the technology is mature for silicon processing, the fact that diamond is metastable leads to possible graphite formation during implantation or in the subsequent post-annealing process, which has been found necessary in order to activate

boron atoms [104]. Many parameters have been investigated such as the substrate temperature during implantation. Prins [104] reported the beneficial results obtained by implanting natural diamonds at 77K at energies up to 120 keV with a total B dose of 4.5×10^{15} cm^{-2}. At this temperature it was proposed that vacancies created in the lattice are "frozen", allowing suitable post-annealing (up to 1750°C) to activate the boron atoms. The dopants exhibited an electrical activation energy of 0.37 eV. Implantation of polycrystalline diamond films has also been demonstrated by Kalish *et al.* [105] who compared B and C implanted films done at -30°C at an ion energy of 60 keV and dose of 2×10^{16} cm^{-2}. After subsequent annealing at 1000°C and the removal of a graphitic surface layer, conductive nature was only observed with the B implanted film. Fontaine *et al.* [106] demonstrated by Raman spectroscopy that the integrity of CVD polycrystalline films remain up to a B dosage threshold of 3×10^{15} cm^{-2} at an energy implant of 90 keV.

Ion implantation, as a technique, offers precise control of dopant concentration as ion beam current can be measured. Good uniformity over the surface, uniform depth profile obtained by multiple implantation at different energy levels and selective doping at preferential sites are other advantages of this technique. However, the drawback is the inevitable lattice damage caused by ion bombardment.

Boron is not the only impurity giving rise to *p*-type conductivity in diamond. Hydrogen, which is found in many natural diamonds [6] and which is present to some extent in all CVD material due its ubiquity for the process of metastable diamond, leads also to this characteristic. However, hydrogen is not a conventional dopant. The *p*-type character is only visible in the surface region. The origin of this effect remains controversial and several models have been proposed to explain this phenomenon. These are reviewed in chapter V. Briefly; it has been proposed that the carriers arise through the formation of shallow acceptors beneath the surface when hydrogen is present, which causes band bending leading to an accumulation of holes in this region [107,108]; other studies suggest that the

adsorption of H_3O^+ ions on the hydrogen-terminated surface induces the *p*-type conductivity [109,110].

II.7.2 *n*-type doping

Nitrogen (N), which is the group IV element adjacent to carbon and which is common in natural diamond, exists in isolated substitutional sites (in type Ib diamond). As such it might be expected to act as an *n*-type electrical dopant for diamond by analogy to phosphorus in silicon. However, the 1.7 eV activation energy required to ionise the nitrogen impurity is such that it renders nitrogen doped diamond insulating at room temperature [111]. Despite this inactivity as a donor impurity, the presence or absence of nitrogen has an important effect on many of the optical and electronic properties of diamond due both to its role in the creation of phonon absorption and carrier recombination centres and its effect in compensating acceptors [112]. In spite of this, the case of UNCD is atypical. The incorporation of nitrogen in these films leads to *n*-type conductivity [113]. However, nitrogen in this particular case is not thought to be a conventional dopant (see chapter VI).

Theoretical calculations for phosphorus (P) doping in diamond predicted the possibility of a shallow (0.2 eV) donor occupying susbstitutional sites albeit with a low solubility [114]. This is due to the large radius of phosphorus (1.10 Å) compared to carbon (0.77 Å), and the rigidity of the diamond lattice. An early attempt of incorporating phosphorus into diamond was conducted by Okano *et al.* [96] using diphosphorus pentoxide (P_2O_5) into a microwave reactor. Due to the low solubility of phosphorus in the diamond lattice, concentrations of less than 10^{17} cm^{-3} were observed, along with the fact that gas concentration appeared to have little influence on film resistivity (~100 Ωcm). Later, Koizumi *et al.* [115], in Japan, were the first to successfully incorporate phosphorus into the diamond lattice. Phosphine (PH_3) was used and Hall measurements confirmed the *n*-type nature of the film. Concentrations exceeding 1×10^{18} cm^{-3} were reported with mobilities of 23 cm^2/Vs and an activation energy of 0.43 eV at 500K. The authors attributed their success to the reduction

of hydrogen incorporation in the film during growth at 950°C. Recently, a few other groups have also been successful in the preparation of P-doped diamond layers [116,117], and devices such as pn-junctions based on P- and B-doped CVD diamond have been fabricated [118]. These results have satisfied even the most vehement sceptics, however no conclusive ion implantation data has been recorded to date [119].

The search for *n*-type dopants has lead to the consideration of other elements. Sulphur (S), sodium (Na) and lithium (Li) have been suggested as potential donors for diamond. The possibility of doping with sulphur was predicted by Saada *et al.* [120] and the first Hall measurements were performed by Nishitani-Gamo *et al.* [121], which reported a mobility of 600 cm^2/Vs at 300K. However, the activation energy was 0.37 eV, which is similar to that of boron. Later SIMS measurements showed that in fact these samples were contaminated with boron and that the Hall voltage was misinterpreted [122]. This unfortunate event was even repeated by another group [123] and has led to the common belief in new sulphur data regardless of its origin. Kajihara *et al.* [114] carried out theoretical studies on the possible doping with sodium and lithium. Their calculations showed that both elements have a preference to occupy interstitial sites with the possibility of being shallow dopants with activation energies of 0.3 eV (Na) and 0.1 eV (Li). However the high energy formation of both elements suggests possible difficulties in incorporation during either growth or in-diffusion. Therefore, the more energetic method of ion implantation has been studied by groups including Prawer *et al.* [124] with implantation of Na and Li ions into natural diamond. The electrical conductance of their samples following implantation was believed to be related to the presence of the implanted ions since similar implantation with other ions of comparable mass did not result in a reduction of the diamond's resistivity. Activation energies of 0.13 eV for Na and 0.2 eV for lithium were obtained with a sheet resistance in the region of $10^9 \Omega/\square$. The conduction was understood in terms of variable range hopping between implant sites in the crystal rather than due to thermal activation.

II.8. PROPERTIES OF DIAMOND

Diamond possesses a compilation of extreme properties, which arise from its composition and structure. It is commonly known to be the hardest material; this is due to each carbon atoms being strongly bonded with another so that a rigid lattice is formed. The structure of diamond is also responsible for various other physical properties. For example, the ease with which lattice vibration, or phonons, can travel through the diamond crystal gives rise to a very high sound propagation velocity and also a very high thermal conductivity. Selected other physical properties are listed in table II.4, along with a comparison with other materials.

Property	**Diamond**	**Notes/comparison**
Knoop's Hardness (kg mm^{-2})	7000	Hardest material know SiC (2480), Si (850), stainless steel (660)
Coefficient of friction	0.1 (in air)	Very low in air
Young's Modulus (10^{11} Nm^{-2})	10.35	Highest mechanical strength SiC (7), Si (1.9), stainless steel (2)
Sound propagation velocity (km s^{-1})	18.2	1.6 times the value of alumina
Chemical inertness		Inert to all acids, bases and solvents at room temperature
Range of high transmittance (μm)	0.22-2.5 and >6	Orders of magnitude lower than other materials in infra-red
Refractive index	2.41	1.6 times the value of silica
Thermal conductivity at 300K (W cm^{-1} K^{-1})	20	Highest value at 300K Si (2.3), SiC (3.2), Cu (5)
Thermal expansion (10^{6} K^{-1})	1	Si (2.33), SiC (3.3), stainless steel (17.3)

Table II.4: Selected properties of diamond [19]

Table II.5 summarises a number of electronic properties that are of particular interest for electronic devices, such as its wide bandgap and high electron and hole mobilities. The comparable mobility values of diamond contrast with those of most other semiconductor materials where the conduction is dominated by electrons. Diamond shows also very high values of electrical breakdown field and intrinsic resistivity. The low relative permittivity and the possible negative electron affinity of diamond also stand out among other semiconducting materials.

Property	Diamond	Si	GaAs	3C-SiC	GaN
Bandgap (eV)	5.45	1.1	1.43	2.2	3.39
Electron mobility ($cm^2V^{-1}s^{-1}$)	2000	1500	8500	1000	900
Hole mobility ($cm^2V^{-1}s^{-1}$)	1800	600	400	40	150
Breakdown field (10^6 Vcm^{-1})	10	0.3	0.4	4	5
Intrinsic resitivity (Ωm)	10^{16}	10^3	10^9	$>10^9$	$>10^9$
Saturation electron velocity (10^7 cm^{-1})	2.7	1	2	2	2.7
Dielectric constant	5.7	11.9	12.8	9.7	9
Electron affinity (eV)	-ve ({111} surface) 4.8 (*p*-type)	4.8	4.7	-	-

Table II.5: Electronic properties of diamond compared with other semiconductors [125,126]

II.9. APPLICATIONS OF DIAMOND

Many demanding applications can be satisfied by exploiting the properties of diamond, making it a useful material rather than a decorative item in the gem stone industry. With the

advent of CVD methods to grow synthetic diamonds, much effort have been made to seek ways of producing cheaper and higher quality synthetic diamond films to encourage the use of synthetic diamond in industry and to lower the cost of diamond to a level where it can be an economically viable material.

II.9.1 Mechanical applications

The high hardness and abrasion resistance, along with high thermal conductivity and low coefficient of friction, of diamond have resulted in it finding extensive use in a wide variety of abrasive or cutting applications ranging from the rough cutting of stone and concrete to ultra-precision machining of electronic ceramics. The majority of diamond used for these applications is synthesized using HPHT growth techniques, and the size of diamond grit used depends on the application type:

1. Rough applications, such as cutting, sawing, mining etc., use a grit size of about 3000 - 6500 μm;
2. Precision applications, such as grinding, require 50 - 500 μm grit size
3. Ultra-precision applications, such as fine grinding, lapping and polishing, use grits from 10 nm to 80 μm.

Further, the development of CVD techniques has enabled the possibility of coating machine parts to provide hard wearing parts.

II.9.2 Thermal applications

As integrated circuit clocks speed up, power densities increase and package footprints decrease the heat generated increases. Over the past decade the computing power has increased by five orders of magnitude [127] and therefore thermal management has become an important consideration. A heat spreader attached to the integrated circuit can lower the operating temperature of the chip. Diamond is the most attractive candidate for this application because of its extremely high thermal conductivity, at up to five times greater

than that of copper. The advantages of CVD diamond over natural or high pressure diamond include the ability to achieve the desired thermal conductivity simply by tuning the fraction of hydrocarbon in the gas supply mixture and the ability to cover large areas of both planar and three-dimensional objects [127]. Other benefits of CVD diamond include a thermal coefficient of expansion similar to silicon and gallium arsenide, low density and high electrical resistivity. The dramatic decrease in cost of CVD diamond over the past decade, from about US$ 5000 per square centimetre to around US$ 5 per square centimetre, has helped the case of diamond over other possible materials. Diamond heat spreaders have also proved to be beneficial in the use of laser diode arrays.

II.9.3 Optical applications

The broadband optical transparency of diamond, covering the near-UV, visible, near and far IR region (except for minor intrinsic absorption bands arising from two-phonon, 1332-2664 cm^{-1}, and three phonon, 2665-3994 cm^{-1}, transitions) makes it a suitable candidate for optical windows. Even at elevated temperatures, diamond remains transparent, since the large bandgap does not allow the formation of free careers. This property, together with the fact that diamond has the highest thermal conductivity makes it the best candidate for high power lasers. The mechanical strength and chemical resistance are also beneficial characteristics of diamond.

Applications include windows for high power CO_2 lasers, at 10.6 μm, and high power microwave (Gyrotron) tubes. Laser-induced damage threshold measurements have yielded results of 10 – 20 GW/cm^2 at 10.6 μm, 6 – 10 GW/cm^2 at 1.06 μm, and around 2 GW/cm^2 at 532 nm [128,129]. Other applications include window domes fitted on the front end of fighter planes' missiles [130]. Diamond in this latter application fulfills all the required needs since it offers IR transparency for the guiding system, it is resistant to heating effects, it has a low friction coefficient for a better penetration in air, and it is resilient to sand or dust impacts.

II.9.4 Electronic applications

Diamond displays a number of attractive electronic properties over other semiconductors for a number of electronic applications. Because of the large (indirect) bandgap of diamond of ~ 5.5 eV the intrinsic carrier concentration at 1000 °C is comparable to that of silicon at room temperature. Also, the surface of diamond is stable up to 500-600 °C in air and 1400-1700 °C in inert atmosphere. For these reasons diamond has been envisaged for high temperature electronic devices. The high breakdown field ($E_{BR}=10^7$ V cm^{-1}) and the high thermal conductivity (σ_c = 20 W cm^{-1} K^{-1}) are two major advantages of diamond over other semiconductors for high frequency, high power devices [131].

The unique properties of diamond have been evaluated by several authors in terms of standard figures of merit, which are intended to indicate the suitability of a semiconductor material for a specific device application [95,132-134]. Amongst these, the most commonly used are the Johnson's [135] and the Keyes's [136] figures of merit, noted JFM and KFM, respectively. The JFM estimates the high-speed power handling capability of a material by assessing the performance limits of a transistor in power microwave applications. The JFM is calculated as:

$$JFM = P_M X_c f_T^2 = \left[\frac{E_{BR} v_s}{2\pi}\right]^2 \qquad \text{(II.1)}$$

where : P_M is the maximum operating power at cut-off frequency f_T, X_C is the channel reactance at this frequency E_{BR} is the electric field breakdown and v_s is the carrier saturation velocity.

The JFM relates the operating power and frequency of a device to the electric field breakdown and the carrier saturation velocity. The JFM for diamond is much higher than the corresponding value for Si and is the highest among existing semiconductors [95]. The

JFM is, however, slightly lower if it is estimated in the case of holes since the saturation velocity for holes is reduced compared to that of electrons.

The KFM expresses the suitability of a material for use in densely packed integrated circuit applications by taking into account the thermal conductivity σ_c as a limiting factor on packing density and the dielectric constant (ε_r = 5.7) as an indication of minimum device dimension which would be electrically viable. The KFM is defined as:

$$KFM = \sigma_c \sqrt{\frac{c v_s}{4\pi\varepsilon_r}} \qquad \text{(II.2)}$$

where: c is the velocity of light in vacuum.

Shenai *et al.* [132] have calculated values for the JFM and the KFM. These figures of merit along with the main parameters have been normalised to the values of silicon and are reproduced in table II.6. It can be seen that diamond outscores the other materials by a substantial margin in both parameters.

Material	ε_r	E_{BR}	v_s	σ_c	JFM	KFM
Si	1	1	1	1	1	1
Ge	1.36	0.54	0.6	0.40	0.1	0.27
GaAs	1.09	1.08	2.0	0.31	4.67	0.41
GaP	0.94	1.89	2.0	0.33	14.3	0.49
6H-SiC	0.85	8.1	2.0	3.3	262	5.1
Diamond	0.47	18.9	2.7	13.3	2601	32

Table II.6: The Johnson and Keyes figures of merit (300K) and their primary constituents for a selection of semiconductors normalised to the values of silicon. Reproduced from [132]

Despite the high values obtained with both the JFM and the KFM, diamond has not yet satisfied the potential which these results suggest. This has been due to various factors, including problems associated with the deep activation energy of available dopants and the rather recent availability of *n*-type doping. Hence, to date, most devices made from diamond are unipolar devices utilising mainly the *p*-type hole conduction. These include Schottky diodes on boron-doped diamond operating up to 1000°C [137], boron/nitrogen *pn*-junction diodes [138,139], bipolar transistors based on this *pn*-junction [138] and field effect transistors (FETs) with boron delta-doped channels [140] and hydrogen-related surface conductive layers [141,142]. Many other device structures, which exploit the diamond's unique properties, have been demonstrated or proposed. To mention just a few, solid-state detectors have been fabricated for both ultraviolet (UV) and x-ray detection [143,144] and particle detection [145,146]. Recently, a UV light emitting diode was realized from a diamond *pn* junction [147]. The *pn* junction was formed from a boron-doped *p*-type layer and a phosphorus-doped *n*-type layer that were grown epitaxially. The *pn* junction exhibited good diode characteristics and under forward bias at about 20V strong UV light emission at 235 nm was observed.

II.10. REFERENCES

[1] M. S. Dresselhaus and M. Endo, in *Carbon Nanotubes. Synthesis, Structure, Properties and Applications*, edited by M. S. Dresselhaus, G. Dresselhaus, and P. Avouris (Springer-Verlag, Berlin Heidelberg, 2001), p. 11.

[2] H. O. Pierson, *Handbook of Carbon, Graphite, Diamond and Fullerenes. Properties, Processing and Applications* (Noyes Publications, Park Ridge, New jersey, U.S.A., 1993).

[3] S. M. Sze, *Semiconductor Devices: physics and technology* (Wiley, New York, 1985).

[4] C. Kittel, *Introduction to Solid State Physics* (John Wiley & Sons, New York, U.S.A., 1986).

[5] C. Y. Fong and B. M. Klein, in *Diamond: Electronic Properties and Applications*, edited by L. S. Pan and D. R. Kania, Electronic Materials: Science and Technology (Kluwer Academic Publishers, Boston / Dordrecht / London, 1995), p. 1.

[6] E. Wilks and J. Wilks, *Properties and Applications of Diamond* (Butterworth-Heinemann Ltd, Oxford, 1991).

[7] I. A. S. Edwards, in *Introduction to Carbon Science*, edited by H. Marsh (Butterworth, London, 1989).

[8] G. S. Woods, in *Properties and Growth of Diamond*, edited by G. Davies (INSPEC, London, 1994), p. 98.

[9] J. F. Banfield,; (1997).

[10] A. T. Collins and A. W. S. Williams, J. Phys. C: Solid St. Phys. **4**, 1789 (1971).

[11] F. P. Bundy, H. T. Hall, H. M. Strong, and R. H. Wentorf, Nature (London) **176**, 51 (1955).

[12] W. Zhu, B. R. Stoner, B. E. Williams, and J. T. Glass, Proc. IEEE **79**, 621 (1991).

[13] F. P. Bundy, W. A. Basset, M. S. Weathers, R. J. Hemley, H. K. Mao, and A. F. Goncharov, Carbon **34**, 141 (1996).

[14] W. G. Eversole, U. S. Patent No. 3030187 (1962).

[15] J. C. Angus, H. A. Will, and W. S. Stanko, J. Appl. Phys. **39**, 2915 (1968).

[16] B. V. Derjaguin, D. V. Fedoseev, V. M. Lukyanovich, B. V. Spitzin, V. A. Ryabov, and A. V. Lavrentyev, Journal of Crystal Growth **2**, 380 (1968).

[17] B. V. Spitsyn, L. L. Bouilov, and B. V. Derjaguin, Journal of Crystal Growth **52**, 219 (1981).

[18] R. J. Koba, in *Diamond Films and Coatings*, edited by R. F. Davis (Noyes Publications, Park Ridge, USA, 1993).

[19] P. K. Bachmann, in *Physics World*; *Vol. 32* (1991).

[20] J. C. Angus, F. A. Buck, M. Sunkara, T. F. Groth, C. C. Hayman, and R. Gat, MRS Bulletin (1989).

[21] P. E. Pehrsson, F. G. Celii, and J. E. Butler, *Diamond Films and Coatings*, R. F. Davies ed. (Noyes Publications, Park Ridge, NJ, 1993).

[22] M. Sunkara, J. C. Angus, C. C. Hayman, and F. A. Buck, Carbon **28**, 745 (1990).

[23] J. C. Angus, in *Properties, growth and applications of diamond*, edited by M. H. Nazaré and A. J. Neves (INSPEC, The Institution of Electrical Engineers, London, 2001), p. 256.

[24] J. E. Butler and D. G. Goodwin, in *Properties, growth and applications of diamond*, edited by M. H. Nazaré and A. J. Neves (INSPEC, The Institution of Electrical Engineers, London, 2001), p. 262.

[25] P. K. Bachmann, in *Thin Film Diamond*, edited by A. Lettington and J. W. Steeds (Chapman & Hall, London, 1993).

[26] S. Matsumoto, Y. Sato, M. Tsutsumi, and N. Setaka, Journal of Materials Science **52**, 219 (1982).

[27] N. Setaka, J. Mater. Res. **4**, 664 (1989).

[28] P. W. May, C. A. Rego, N. M. R. Ashfold, K. N. Rosser, G. Lu, T. D. Walsh, L. Holt, N. M. Everitt, and P. G. Partridge, Diamond Relat. Mater. **4**, 794 (1995).

[29] M. Kamo, Y. Sato, S. Matsumoto, and N. Setaka, Journal of Crystal Growth **62**, 642 (1983).

[30] H. Kawarada, K. S. Mar, and A. Hiraki, Jpn. J. Appl. Phys. **26**, L1032 (1987).

[31] P. K. Bachmann, in *Handbook of Industrial Diamonds and Diamond Films*, edited by M. A. Prelas, G. Popovici, and L. K. Bigelow (Marcel Dekker Inc., New York, USA, 1998).

[32] S. Matsumoto, M. Hino, and T. Kobayashi, Appl. Phys. Lett. **51**, 737 (1987).

[33] K. Suzuki, A. Sawabe, H. Yasuda, and T. Inuzuka, Appl. Phys. Lett. **50**, 728 (1987).

[34] K. Kurihara, K. Sasaki, M. Kawarada, and N. Koshino, Appl. Phys. Lett. **52**, 437 (1988).

[35] Y. Hirose, in *First Int. Conf. New Diamond Science and Technology*, Tokyo, Japan, 1988.

[36] Y. Hirose and M. Mitsuizumi, New Diamond **4**, 34 (1988).

[37] P. K. Bachmann, in *Properties and Growth of Diamond* (INSPEC, The Institution of Electrical Engineers, London, UK, 1994).

[38] B. V. Derjaguin and D. B. Fedoseev, Scientific American **233**, 102 (1975).

[39] S. Matsumoto and Y. Matsui, Journal of Materials Science **18**, 1785 (1983).

[40] S. A. Godleski, P. V. Schleyer, E. Osawa, and W. T. Wipke, Prog. Phys. Org. Chem. **13**, 63 (1981).

[41] S. E. Stein, Nature **346**, 517 (1990).

[42] S. Mitura, Journal of Crystal Growth **80**, 417 (1987).

[43] M. Frenklach, W. Howard, D. Huang, J. Yuan, K. E. Spear, and R. J. Koba, Appl. Phys. Lett. **59**, 546 (1991).

[44] P. R. Buerki and S. Leutwyler, J. Appl. Phys. **69**, 3739 (1991).

[45] J. Singh, J. Mater. Sci. **29**, 2761 (1994).

[46] S. D. Wolter, B. R. Stoner, J. T. Glass, P. J. Ellis, D. S. Buhaenko, C. E. Jenkis, and P. Southworth, Appl. Phys. Lett. **62**, 1215 (1993).

[47] W. R. L. Lambrecht, C. H. Lee, B. Segall, J. C. Angus, Z. Li, and M. Sunkara, Nature **364**, 607 (1993).

[48] D. N. Belton and S. J. Schmieg, Thin Solid Films **212**, 68 (1992).

[49] P. Bou, L. Vandenbulcke, R. Herbin, and F. Hillion, J. Mater. Res. **7**, 2151 (1992).

[50] H. Liu and D. S. Dandy, Diamond Relat. Mater. **4**, 1173 (1995).

[51] M. M. Waite and S. I. Shah, Appl. Phys. Lett. **60**, 2344 (1992).

[52] T. P. Ong, F. Xiong, R. P. H. Chang, and C. W. White, J. Mater. Res. **7**, 2429 (1992).

[53] W. R. L. Lambracht, C. H. Lee, B. Segall, J. C. Angus, Z. Li, and M. Sunkara, Nature **364**, 607 (1993).

[54] A. R. Badazian and T. Badazian, Surf. Coat. Technol. **36**, 283 (1988).

[55] M. A. George, A. Burger, W. E. Collins, J. L. Davidson, A. V. Barnes, and N. H. Tolk, J. Appl. Phys. **76**, 4099 (1994).

[56] P. O. Joffreau, R. Haubner, and B. Lux, Int. J. Ref. Hard Mater. **7**, 186 (1988).

[57] B. Lux and R. Haubner, in *Diamond and Diamond-like Films and Coatings*, edited by R. E. Clausing, L. L. Horton, J. C. Angus, and P. Koidl (Plenum Press, New York, USA, 1991), p. 579.

[58] B. R. Stoner, G.-H. M. Ma, S. D. Wolter, and J. T. Glass, Phys. Rev. B **45**, 11067 (1992).

[59] F. C. Frank and J. H. van der Merwe, Proc. R. Soc. London Ser. A **198**, 205 (1949).

[60] M. Volmer and A. Weber, Z. Phys. Chem. **119**, 277 (1926).

[61] M. Komori, T. Maki, T. Kim, G. Hou, Y. Sakaguchi, K. Sakuta, and T. Kobayashi, Appl. Phys. Lett. **62**, 582 (1993).

[62] S. Koizumi, T. Murakami, T. Inuzuka, and K. Suzuki, Appl. Phys. Lett. **57**, 563 (1990).

[63] F. Akatsuka and F. Shimura, in *Applications of Diamond Films and Related Materials*, edited by Y. Tzeng, Y. Yoshikawa, M. Murakawa, and A. Feldman (Elsevier, Amsterdam, 1991), p. 379.

[64] R. Locher, C. Wild, W. Muller-Sebert, R. Kohl, and P. Koidl, Diamond Relat. Mater. **2**, 1248 (1993).

[65] C. F. Chen, in *1st Int. Conf. Diamond Sci. and Technol.*, Tokyo, 1988, p. 118.

[66] S. Yugo, T. Kanai, T. Kimura, and T. Muto, Appl. Phys. Lett. **58**, 1036 (1991).

[67] H. C. Shih, C. P. Sung, and W. L. Wan, Surf. Coat. Technol. **54-55**, 380 (1992).

[68] D. M. Gruen, Annual Review of Materials Science **29**, 211 (1999).

[69] P. Ascarelli and S. Fontana, Appl. Surf. Sci. **64**, 307 (1993).

[70] M. Ihara, H. Komiyama, and T. Okubo, Appl. Phys. Lett. **65**, 1192 (1994).

[71] P. A. Dennig and D. A. Stevenson, Appl. Phys. Lett. **59**, 1562 (1991).

[72] K. kobayashi, N. Matsukura, and Y. Machi, Mater. Manufact. Proc. **7**, 395 (1992).

[73] S. J. Lin, S. J. Lee, J. Hwang, C. S. Chang, and H. Y. Wen, Appl. Phys. Lett. **60**, 1559 (1992).

[74] M. Katoh, M. Aoki, and H. Kawarada, Jpn. J. Appl. Phys. **33**, L194 (1994).

[75] J. C. Angus and C. C. Hayman, Science **241**, 913 (1988).

[76] Z. Feng, K. Komvopoulos, I. G. Brown, and D. B. Bogy, J. Appl. Phys. **74**, 2841 (1993).

[77] J. E. Yehoda, R. I. Fuentes, J. C. Tsang, S. J. Whitehair, C. R. Guarnieri, and J. J. Cuomo, Appl. Phys. Lett. **60**, 2865 (1992).

[78] K. Kobayashi, M. Kumagai, S. Karasawa, T. Watanabe, and F. Togashi, Journal of crystal Growth **128**, 408 (1993).

[79] J. Narayan, V. P. Godbole, G. Matera, and R. K. Singh, J. Appl. Phys. **71**, 966 (1992).

[80] Y. Hayashi, W. Drawl, and R. Messier, Jpn. J. Appl. Phys. **31**, L193 (1992).

[81] S.-E. Park and C. H. Lee, J. Mater. Sci. **28**, 1799 (1993).

[82] J. W. Kim, Y. J. Baik, and K. Y. Eun, in *Applications of Diamond Films and Related Materials*, edited by Y. Tzeng, Y. Yoshikawa, M. Murakawa, and A. Feldman (Elsevier, Amsterdam, 1991), p. 379.

[83] Y. Hibino and Y. Hayashi, Surf. Coat. Technol. **54-55**, 365 (1992).

[84] D. Kim, H. Lee, and J. lee, J. Mater. Sci. **28**, 6704 (1993).

[85] B. Singh, O. R. Mesker, A. W. Levine, and Y. Arie, Proc. SPIE **877**, 70 (1988).

[86] S. I. Shah and M. M. Waite, Appl. Phys. Lett. **61**, 3113 (1992).

[87] Y. H. Shing, F. S. Pool, and D. H. Rich, Thin Solid Films **212**, 150 (1992).

[88] N. Othake and M. Yoshikawa, Jpn. J. Appl. Phys. **32**, 2067 (1993).

[89] J. J. Brophy, Phys. Rev. **99**, 1336 (1955).

[90] I. G. Austin and R. Wolfe, Proc. Phys. Soc. **69B**, 329 (1956).

[91] A. T. Collins and A. W. S. Williams, Solid State Phys., 1789 (1970).

[92] M. W. Geis and J. C. Angus, Scientific American **October**, 64 (1992).

[93] R. H. Wentorf and H. P. Bovenkerk, J. Chem. Phys. **36**, 1987 (1959).

[94] N. Fujimori, T. Imai, and A. Doi, Vacuum **6**, 99 (1986).

[95] G. S. Gildenblat, S. A. Grot, and A. R. Badzian, Proc. IEEE **79**, 647 (1991).

[96] K. Okano, H. Kiyota, T. Iwasaki, Y. Nakamura, Y. Akiba, T. Kurosu, M. Iida, and T. Nakamura, Appl. Phys. A-Mater. Sci. Process. **51**, 344 (1990).

[97] J.-P. Lagrange, A. Deneuville, and E. Gheeraert, Diamond Relat. Mater. **7**, 1390 (1998).

[98] K. Okano, H. Naruki, Y. Akiba, T. Kurosu, M. Iida, and Y. Hirose, Jpn. J. Appl. Phys. **27**, L173 (1988).

[99] J. Mort, M. Machonkin, M. Morgan, F. Jansen, K. Okumura, D. Kuhman, Y. M. LeGrice, and R. J. Nemanich, Proc. 1st International Symp. on Diamond and Diamond-Like Films (Electrochemical Society) **89-12**, 420 (1989).

[100] N. Fujimori, Jpn. J. Appl. Phys. **29**, 824 (1990).

[101] J. Mort, K. Okumura, and M. Machonkin, Phil. Mag. B **63**, 1031 (1991).

[102] K. Nishimura, K. Das, and J. T. Glass, Appl. Phys. Lett. **69**, 3142 (1991).

[103] B. A. Fox, B. R. Stoner, D. M. Malta, P. J. Ellis, R. C. Glass, and F. R. Sivazlian, Diamond Relat. Mater. **4**, 382 (1994).

[104] J. F. Prins, Thin Solid Films **212**, 11 (1992).

[105] R. Kalish, C. Uzan-Saguy, A. Samoiloff, R. Locher, and P. Koidl, Appl. Phys. Lett. **64**, 2532 (1994).

[106] F. Fontaine, A. Deneuville, E. Gheeraert, P. Gonon, L. Abello, and G. Lucazeau, Diamond Relat. Mater. **3**, 623 (1994).

[107] K. Hayashi, S. Yamanaka, H. Watanabe, T. Sekiguchi, H. Okushi, and K. Kajimura, J. Appl. Phys. **81**, 744 (1997).

[108] J. Shirafuji and T. Sugino, Diamond Relat. Mater. **5**, 706 (1996).

[109] F. Maier, M. Riedel, B. Mantel, J. Ristein, and L. Ley, Phys. Rev. Lett. **85**, 3472 (2000).

[110] C. E. Nebel, C. Sauerer, F. Ertl, M. Stutzmann, C. F. O. Graeff, P. Bergonzo, O. A. Williams, and R. B. Jackman, Appl. Phys. Lett. **79**, 4541 (2001).

[111] A. T. Collins, in *Properties and Growth of Diamond*, edited by G. Davies (INSPEC, London, 1994), p. 284.

[112] S. Sonoda, J. H. Won, H. Yagi, A. Hatta, T. Ito, and A. Hiraki, Appl. Phys. Lett. **70**, 2574 (1997).

[113] O. A. Williams, S. Curat, J. E. Gerbi, D. M. Gruen, and R. B. Jackman, Appl. Phys. Lett. **85**, 1680 (2004).

[114] S. A. Kajihara, A. Antonelli, and J. Bernholc, Physica B **185**, 144 (1993).

[115] S. Koizumi, M. Kamo, Y. Sato, H. Ozaki, and T. Inuzuka, Appl. Phys. Lett. **71**, 1065 (1997).

[116] A. Tajani, E. Gheeraert, N. Casanova, E. Bustarret, J. A. Garrido, G. Rumen, C. E. Nebel, M. E. Newton, and D. Evans, Phys. Status Solidi A-Appl. Res. **193**, 541 (2002).

[117] M. Nesladek, K. Haenen, J. D'Haen, S. Koizumi, and H. Kanda, Phys. Status Solidi A-Appl. Res. **199**, 77 (2003).

[118] S. Koizumi, K. Watanabe, F. Hasegawa, and H. Kanda, Science **292**, 1899 (2001).

[119] R. Kalish, Diamond Relat. Mater. **10**, 1749 (2001).

[120] D. Saada, J. Adler, and R. Kalish, Appl. Phys. Lett. **77**, 878 (2000).

[121] M. Nishitani-Gamo, E. Yasu, C. Xiao, Y. Kikuchi, K. Ushisawa, I. Sakaguchi, T. Suzuki, and T. Ando, Diamond Relat. Mater. **9**, 941 (2000).

[122] R. Kalish, A. Reznik, C. Uzan-Saguy, and C. Cytermann, Appl. Phys. Lett. **76**, 757 (2000).

[123] E. Gheeraert, N. Casanova, A. Tajani, A. Deneuville, E. Bustarret, J. A. Garrido, C. E. Nebel, and M. Stutzmann, Diamond Relat. Mater. **11**, 289 (2002).

[124] S. Prawer, C. Uzan-Saguy, G. Braunstein, and R. Kalish, Appl. Phys. Lett. **63**, 2502 (1993).

[125] M. N. Yoder, in *Diamond Films and Coatings*, edited by R. F. Davis (Noyes Publications, New Jersey, USA, 1993).

[126] H. Morkoc, W. S. Strite, G. B. Gao, M. E. Lin, B. Sverdlov, and M. Burns, J. Appl. Phys. **76**, 1363 (1994).

[127] H. Windischmann, in *Properties, Growth and Applications of Diamond*, edited by M. H. Nazare and A. J. Neves (INSPEC, The Institution of Electrical Engineers, London, 2000), p. 410.

[128] *Low-Pressure Synthetic Diamond. Manufacturing and Applications*, edited by B. Dischler and C. Wild (Springer-Verlag, Berlin Heidelberg, 1998).

[129] C. Klein, Proc. SPIE **2428**, 517 (1995).

[130] J. A. Savage, C. J. H. Wort, C. S. J. Pickles, R. S. Sussman, C. G. Sweeney, M. R. McClymont, J. R. Brandon, C. N. Dodge, and A. C. Beale, SPIE **3060**, 144 (1997).

[131] M. W. Geis, Proc. IEEE **79**, 669 (1991).

[132] K. Shenai, R. S. Scott, and B. J. Baliga, IEEE Trans. Electron Devices **36**, 1811 (1989).

[133] B. J. Baliga, IEEE Electron Device Lett. **10**, 455 (1989).

[134] K. Shenai, IEEE Electron Device Lett. **11**, 520 (1990).

[135] N. M. Johnson, RCA Review **26**, 163 (1963).

[136] R. W. Keyes, Proc. IEEE **63** (1975).

[137] A. Vescan, I. Daumiller, P. Gluche, W. Ebert, and E. Kohn, Diamond Relat. Mater. **7**, 581 (1998).

[138] A. Aleksov, A. Denisenko, M. Kunze, A. Vescan, A. Bergmaier, G. Dollinger, W. Ebert, and E. Kohn, Semicond. Sci. Technol. **18**, S59–S66 (2003).

[139] A. Aleksov, A. Denisenko, and E. Kohn, Solid State Electron **44**, 369 (2000).

[140] A. Aleksov, A. Vescan, M. Kunze, P. Gluche, T. Borst, and E. Kohn, Diamond Relat. Mater. **8**, 942 (1999).

[141] K. Tsugawa, H. Umezawa, and H. Kawarada, Jpn. J. Appl. Phys. Part 1 - Regul. Pap. Short Notes Rev. Pap. **40**, 3101 (2001).

[142] H. Umezawa, T. Arima, N. Fujihara, H. Taniuchi, H. Ishizaka, M. Tachiki, C. Wild, P. Koidl, and H. Kawarada, Jpn. J. Appl. Phys. Part 1 - Regul. Pap. Short Notes Rev. Pap. **41**, 2611 (2002).

[143] R. D. McKeag and R. B. Jackman, Diamond Relat. Mater. **7**, 513 (1998).

[144] C. P. Beetz, B. Lincoln, D. R. Winn, K. Segall, M. Vasas, and D. Wall, IEEE Transactions on Nuclear Science **38**, 107 (1991).

[145] J. Kaneko and M. Katagiri, Nuclear Instruments and Methods in Physics Research Section A: Accelerators, Spectrometers, Detectors and Associated Equipment **383**, 547 (1996).

[146] C. Manfredotti, F. Fizzotti, E. Vittone, S. Bistolfi, M. Boero, and P. Polesello, Nuclear Instruments and Methods in Physics Research B **93**, 516 (1994).

[147] S. Koizumi, K. Watanabe, M. Hasegawa, and H. Kanda, Science **292**, 1899 (2001).

CHAPTER III
EXPERIMENTAL AND CHARACTERISATION TECHNIQUES

III.1. Introduction
III.2. Surface cleaning and preparation
  III.2.1 Acid bath cleaning of diamond surfaces
  III.2.2 Hydrogenation of diamond surfaces
III.3. Surface characterisation
  III.3.1 Scanning electron microscopy
  III.3.2 Scanning tunnelling microscopy
III.4. Resistive deposition of metal contacts
III.5. Electrical characterisation
  III.5.1 IV measurements
  III.5.2 Hall effect measurements
  III.5.3 Impedance spectroscopy measurements
III.6. References

III.1. INTRODUCTION

This chapter presents descriptions and general principles of the main experimental techniques that have been used during the course of this thesis. Additional details of actual experimental set-ups are given in the experimental sections of the following chapters.

III.2. SURFACE CLEANING AND PREPARATION

III.2.1 Acid bath cleaning of diamond surfaces

The purpose of this treatment is to remove any graphitic or non-diamond carbon from the surface of the diamond sample without etching being observed.

High temperature oxidation using solvents is commonly used to clean surfaces but in this particular case this method is not effective since carbon based surface contaminants are resistant to virtually most solvents. Moreover this approach attacks the surface of the sample. A suitable process is to employ a less aggressive solution for the surface, which is powerful enough to remove the non-diamond carbon on the surface of the film. Mixtures of sulphuric acid with either ammonium persulphate [1] or chromic acid have been used [2-4]. The former solution is the preferred one in our laboratories since this treatment is believed to offer better performance when used during the fabrication of electronic devices [5].

The cleaning process consists of an initial degrease in warm trichloroethylene followed by an immersion at room temperature into two successive solvent baths: acetone and isopropanol. The sample is then transferred into the acid bath. This etching solution is prepared according to the following procedure:

(i) 6 teaspoons of Ammonium Persulphate ($(NH_4)_2S_2O_8$) is added to 30ml of concentrated sulphuric acid (H_2SO_4) to create a super-saturated solution at room temperature.

(ii) This solution is heated up to 200 ^{0}C. When the temperature reaches 85 ^{0}C the sample is placed into the solution and left in the acid bath for 20 minutes starting from the time the temperature reads 170 ^{0}C.

(iii) After the 20 minute countdown the sample is transferred to the 'rinse' solution: 10 ml of Hydrogen Peroxide (H_2O_2) and 10 ml of Ammonium Hydroxide (NH_4OH).

(iv) Following a 10 minute exposure to the 'rinse' solution the sample is rinsed in DI water and blown dry with nitrogen.

III.2.2 Hydrogenation of diamond surfaces

CVD diamonds exhibit high surface *p*-type surface conductivity after removal from the growth chamber due to hydrogen termination of the surface; hydrogen can be removed by oxidation using an acid solution or oxygen ambient annealing methods [3,6]. Since various applications of CVD diamond rely on this conductive surface, rehydrogenation of these surfaces has become an important issue.

Many groups have performed rehydrogenation in a hydrogen plasma using the PECVD growth condition parameters followed by cooling the sample in the hydrogen plasma to room temperature [7,8]. Some others have been using a hot filament apparatus as a source for the atomic hydrogen [9,10]. More recently, Williams *et al.* [11] obtained similar results by immersing these films in a hydrogen plasma for much shorter time lengths and without cooling in the plasma. This latter method has the advantage of preventing substantial surface etching from long duration rehydrogenation [12].

Hydrogenation of samples in this work was conducted in a conventional resonant standing wave CVD diamond growth chamber. The standard conditions used are 500 ^{0}C, 8 torr, 5 minutes. The hydrogen plasma was generated by a 1kW, 2.45GHz microwave power supply.

It was observed that varying the plasma conditions had little effect on the resulting surface conductivity and that the process was successful even with exposure times as short as 2 seconds.

III.3. SURFACE CHARACTERISATION

III.3.1 Scanning electron microscopy

Scanning electron microscopy (SEM) is a form of microscopy that uses a beam of electrons instead of a beam of light (as in optical microscopy), to form an image of a very small object. This has two main advantages: much larger magnifications are possible since electron wavelengths (λ_e) are much smaller than photon wavelengths and the depth of field is much larger.

$$\lambda_e = \frac{h}{mv} = \frac{h}{\sqrt{2qmV}} = \frac{12.2}{\sqrt{V}} \quad (\text{Å}) \qquad \text{(III.1)}$$

where:
λ_e is the electron wavelength
h is Planck's constant
m is the mass of the electron
v is the electron velocity
V is the accelerating voltage

Equation (III.1) shows that when electrons are accelerated by an electric field to velocities where they have a De Broglie wavelength, they can be associated with a considerably shorter wavelength than visible light. For example, electrons accelerated under 10 kV would have a wavelength of 0.12 Å – a wavelength significantly below the 4000-7000 Å wavelength range for visible light. Hence the resolution of SEM can be much higher than that of an optical microscope. In optical microscopes, the resolution is limited by the wavelength of visible light to ≈ 250 nm [13] and the depth of field considerations lead to a maximum useful magnification of ≈ 500×. In contrast, a resolution of 2.5-10 nm can be offered by SEM with a magnification in the range 500× - 40000× and a depth of field ≈ 500 times that of an optical system [14,15].

SEM is not however a direct analogue of optical microscopy in that the scanning of a focused electron beam over a sample's surface causes emission of secondary and back-scattered electrons. X-ray photons will be also induced due to the bombardment of the primary electrons at the sample. Sensing the secondary and/or the back-scattered electrons conventionally produces the image of the sample. In the most common imaging mode, secondary electrons are detected by a scintillator-photomultiplier device and the resulting signal is used to modulate the intensity of a cathode ray tube (CRT) so that the image can be generated. This mode of operation is known as the 'secondary emission' and is the default form of SEM; some units support additional modes of analysis which allow elemental identification or which detect photons to yield cathodoluminescence spectra.

Non-conducting material, such as un-doped diamonds, needed to be pre-coated with a thin layer of conducting material to avoid charging and therefore avoid the measurement to be distorted. Gold was commonly used as a conductive coating.

III.3.2 Scanning tunnelling microscopy

Scanning tunnelling microscopy (STM) is a non-optical microscopy technique, which allows the investigation of electrically conducting surfaces down to the atomic scale. A schematic of the basic implementation is shown in figure III.1.

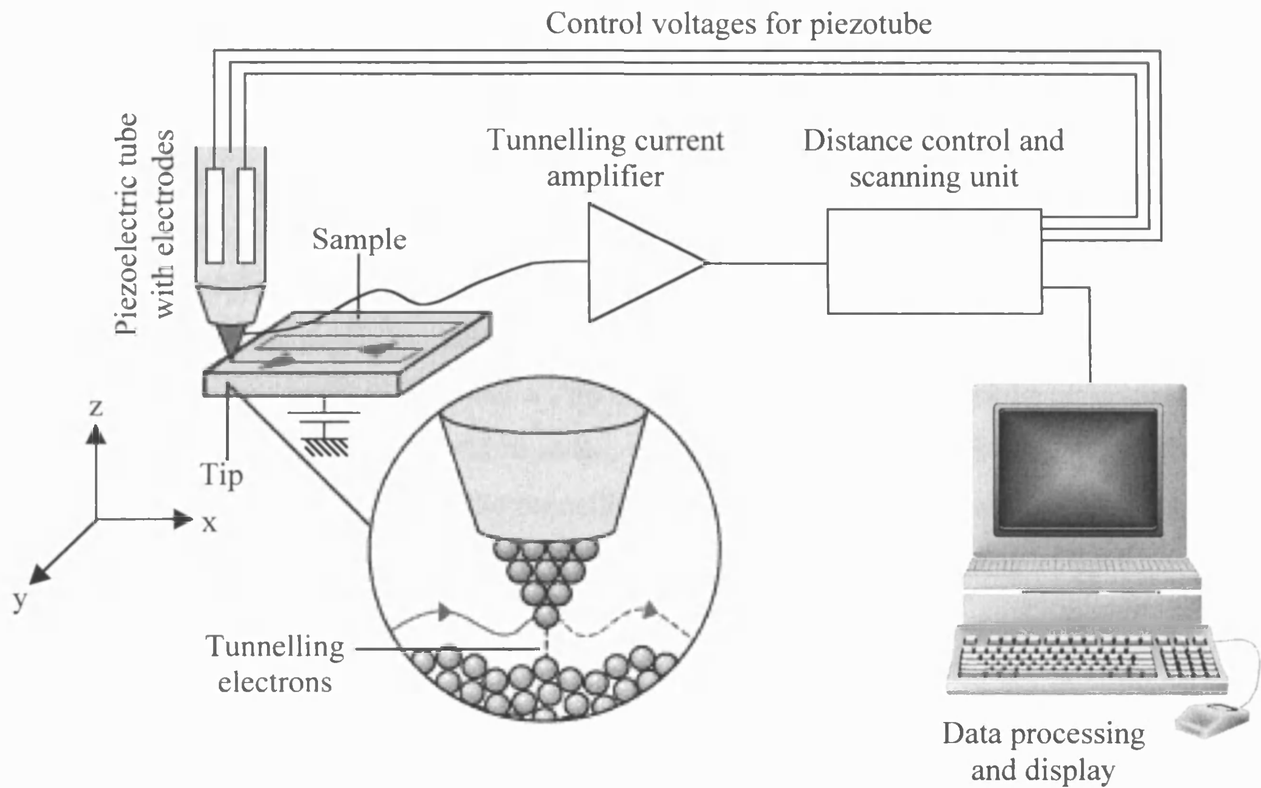

Figure III.1: Basic STM setup

When a very sharp tip - in practice, a needle which has been treated so that a single atom projects from its end - is brought sufficiently close to the surface of the material under study (below ≈1 nm), there is a strong interaction between the electron cloud on the surface and that of the tip atom, and an electric tunnelling current (≈ 1 nA) flows when a small voltage is applied (≈ 0.05 V). At a separation of a few atomic diameters, the tunnelling current rapidly increases as the distance between the tip and the surface decreases. This rapid change of tunnelling current with distance results in atomic resolution and an image of the surface is produced as the probe tip is scanned over the surface using piezoelectric elements.

There are two basic modes of operations: constant current mode and constant height mode. In constant current mode, the distance between the tip and the sample, and hence the tunnelling current, is held constant by the electronics of the system control as the probe is scanned across the surface. Thus the piezoelectric voltage read from the z-direction transducer will be proportional to the vertical displacement. This movement is recorded and can be displayed as an image of the surface topography. In constant height mode, the probe is scanned across the surface with no movement in the z-direction. Hence the current varies as the gap between the surface and the tip changes and a contour plot can be generated from the variation in current. It should be noted, that STM images not only display the geometric structure of the surface since the tunnelling current depends on the electronic density of states of the sample. Therefore scanning the surface gives in reality a map of the density of states.

One problem with STM measurements on diamond is the high resistivity of intrinsic material. This can be solved by either using doped diamond or the hydrogen surface conductivity layer. However, under vacuum, the hydrogen surface conductivity is lost and it is for this reason that STM measurements have been performed in air.

III.4. RESISTIVE DEPOSITION OF METAL CONTACTS

Metal contacts can be deposited via a few techniques namely resistive evaporation, flash evaporation, sputtering and electron beam evaporation. Resistive evaporation will be described in this section as it was the main method for depositing thin metal film for most of the experimental work in this thesis. Evaporation is conducted by passing a current through a high resistance wire, filament or boat until a vapour consisting largely of the required material is produced. The vapour, which is composed of energetic molecules of the material, is then allowed to impinge upon a substrate, which is considerably cooler than the source; the molecules lose energy and remain in contact with the substrate. This process

is carried out at low pressures ($<10^{-6}$ mbar) to prevent collisions between the molecules and the ambient gases which reduce the number of molecules reaching the substrate and contaminate the deposit. The high vacuum, at which the process is carried out, also prevents rapid oxidation of the metallic vapour and lowers the vaporization temperature. The high resistive element is normally made from refractory metals such as tungsten and molybdenum, which have very high melting points (3380°C and 2610°C at atmospheric pressure, respectively). It is preferable that the metal sublimes, as this avoids interaction of the metal liquid phase with the filament or heating elements. Some metals (for example: titanium) form alloys with tungsten at high temperature and this normally leads to the destruction of the filament during evaporation. Aluminium (Al), gold (Au), silver (Ag), tin (Sn), nickel (Ni) and chromium (Cr) can be easily deposited using this method. Other compounds such as calcium fluoride (CaF_2) have also been evaporated using this technique. The key advantage of vacuum evaporation is the very high deposition rate achievable so that thick metal films (500nm) can be formed. This method, however, requires line of sight from the source to the target, as a result complex and irregular shape samples may not be uniformly coated.

The resistive evaporation system used for depositing metal film in this work was an Edwards 306. The base pressure during the evaporation was kept below 10^{-6}mbar. This pressure was achieved by a diffusion pump backed by a rotary pump. Liquid nitrogen cold trap was used in addition to remove unwanted contamination from the diffusion pump and to maintain low pressure during resistive heating itself. Evaporation for Au and CaF_2 was carried out using a molybdenum boat.

III.5. ELECTRICAL CHARACTERISATION

III.5.1 IV measurements

The current-voltage characteristics of a sample were carried out either using a Keithley K487 voltage source/picoammeter or a HP 4145B parameter analyser. The Keithley K487 is capable of providing an output potential up to 500V (subject to a current limit of 2.2 mA) and measures currents in the range 0.01 pA to 2.2mA. The parameter analyser however can measure higher currents (up to 100mA) but is limited to deliver a maximum potential of 100V.

Both instruments were connected to a computer via a GPIB interface for automated measurements. Labview and Testpoint were the two software packages used for instrument control and data acquisition.

Electrical connections to the sample were made either by bonding or by means of manually manipulated needle-probes. The sample was always supported by a solid steel/copper plate inside a grounded metal box or vacuum chamber to reduce the noise generated by electromagnetic interference. For samples exhibiting edge or back face conductivity, an electrically insulating plate (mica or teflon) was inserted between the sample and the solid steel/copper plate. This was to ensure that the current measured was from the sample only and not from the electrically conductive supporting plate.

Sample to system interconnects were made via co-axial or tri-axial low noise cables and BNC connectors.

III.5.2 Hall effect measurements

Hall effect measurements is an electro-magnetic characterisation technique used to determine some of the electrical properties of semiconductors and metals. It gives information on the carrier type, the carrier concentration and the mobility. If in addition the measurements are carried out over a temperature range, information about scattering

mechanisms of carriers, activation energy of dopants and factors governing the resistivity of a material can be gathered.

The Hall effect was named after its founder in 1879 when he measured a potential difference across two sides of a conductor carrying a current in a magnetic field.

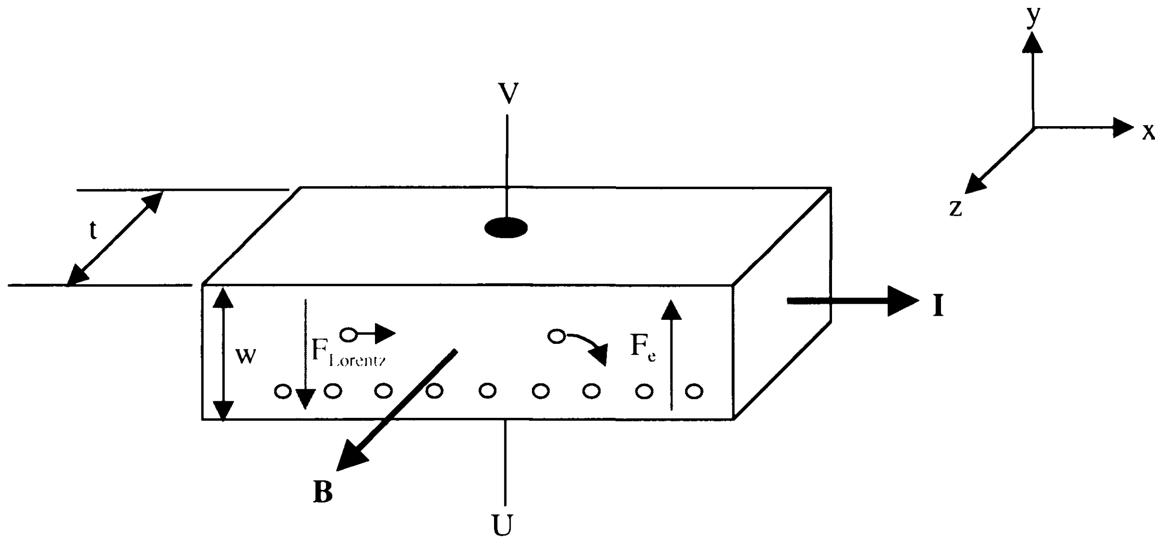

Figure III.2: Hall effect in a *p*-type sample

Figure III.2 shows a *p*-type semiconductor with a carrier (hole) moving from left to right as a current I flows in the x-direction. This current is given by:

$$I = w\, t\, p\, q\, v_{d\,x} \qquad \text{(III.2)}$$

where:
- w is the width of the bar
- t is the thickness
- p is the density of holes
- q is the electric charge
- $v_{d\,x}$ is the average drift velocity of carriers in the x-direction

When a magnetic field B is applied in the z-direction in conjunction with the current flow, a force called the Lorentz force deflects the carriers away from the current line towards the bottom of the sample as indicated in figure III.1 by the hole with the curved arrow. This force is expressed as:

$$\mathbf{F}_{Lorentz} = q\mathbf{v}_d \times \mathbf{B} \qquad \text{(III.3)}$$

The resulting carrier movement builds up a positive charge at the bottom side of the sample establishing a potential gradient between U and V (called the Hall voltage V_H) and an electric force F_e is applied on the carriers. This force is along the same line as the Lorentz force but is oppositely directed.
When the equilibrium is established:

$$\mathbf{F}_{Lorentz} = -\mathbf{F}_e \qquad \text{(III.4)}$$

The Hall voltage can be derived using (III.3) and (III.4):

$$\mathbf{F}_{Lorentz} = -\mathbf{F}_e$$

$$q\mathbf{v}_d \times \mathbf{B} = -\, q\, \mathbf{E}$$ where **E** is the electric field defined as $-V_H/w$

$$v_{d\,x}\, B_z = \frac{V_H}{w}$$

therefore: $$V_H = v_{d\,x}\, B_z\, w \qquad \text{(III.5)}$$

combining (III.2) and (III.5) gives:

$$V_H = \frac{B_z\, I}{t\, p\, q} \qquad \text{(III.6)}$$

From the above expression the density p of free carriers can be determined and from the sign of the Hall voltage the type of carriers can be identified.

The Hall mobility μ_H of the carriers is deduced from equation (III.7) provided the resistivity ρ of the material is known:

$$\mu_H = \frac{1}{\mathrm{p\,q}\,\rho} \quad \text{(III.7)}$$

Equation (III.7) holds only under the assumption of energy-independent scattering mechanisms otherwise the Hall mobility has to be modified by a factor *r*, the Hall scattering factor. This factor depends on the scattering mechanisms in the semiconductor and generally lies between 1 and 2. It is also a function of the magnetic field and temperature. Hence taking into account the scattering factor *r*, the Hall mobility becomes:

$$\mu_H = r\,\mu_p \quad \text{(III.8)}$$

where μ_H is the Hall mobility and μ_p is the conductivity mobility for the holes. Conductivity mobilities can therefore differ significantly from the measured Hall mobilities. However the factor *r* was taken as unity in this work since the scattering mechanisms in diamond are not clearly identified.

The resistivity ρ of the material needs to be known to determine the carrier mobility. The four-point probe method is commonly used to measure the resistivity. The probes are arranged in line and are equidistantly spaced. A voltage drop is then measured between the two inner probes while a current is passed through the outer electrodes [16].

The sheet resistivity $\rho_s = \rho/\mathrm{t}$ (expressed in Ω/□) is normally used in the calculations to determine the mobility when the thickness of the sample is not well defined. Using (III.6) and (III.7) μ_H is given by:

$$\mu_H = \frac{V_H\, t}{B_z\, I\, \rho} = \frac{V_H}{B_z\, I\, \rho_s} \qquad \text{(III.9)}$$

The Hall "bar" or the bridge type configuration [16] is normally the preferred way to derive the resisitivity, the carrier concentration and the Hall mobility. However this geometrical configuration may not be convenient for characterising thin films of material as it is difficult to process the required configuration using such films.

A more general geometry was developed by van der Pauw [17,18]. The Hall effect measurement evaluation is based on a conformal mapping of arbitrary shaped samples (see figure III.3) without the need to know the current flow paths in the sample. The following conditions must however be met:

1. the contacts are at the circumference of the sample
2. the contacts are sufficiently small
3. the sample is uniform in thickness
4. the surface of the sample is singly connected, i.e. the sample does not contain isolated holes

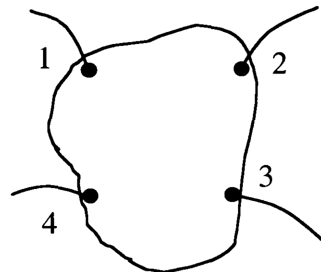

Figure III.3: typical contacts position in the van der Pauw configuration

With reference to figure III.3 the resistivity ρ is given by:

$$\rho = \frac{\pi t}{\ln 2} \frac{(R_{12,34} + R_{23,41})}{2} F \qquad \text{(III.10)}$$

where t is the thickness of the sample

$R_{12,34} = \frac{V_{34}}{I_{12}}$

$R_{23,41} = \frac{V_{41}}{I_{23}}$

with $V_{xy} = V_y - V_x$ and I_{xy} being the current entering the sample through contact x and leaving through contact y.

F is a correction factor and is a function of the ratio of $\frac{R_{12,34}}{R_{23,41}}$. It is a measurement of the deviation from the symmetric situation, e.g. circular or square samples would have F=1.

Hall effect measurements have been performed on samples in the van der Pauw configuration using a Lakeshore 75014 commercial system. This equipment allows data acquisition at temperatures ranging from 10K to 350K under a magnetic field of 10.4 kG. In practice the field was switched from positive to negative values. As a result twice the Hall voltage was measured: $V_H = \frac{\Delta V_{12}}{2}$ where ΔV_{12} is the potential difference between contacts 1 and 2 when the polarity of the magnetic field is changed from positive to negative with the current flowing from contact 3 to 4.

The measurements were performed in such a way to maximise the signal to error ratio.

III.5.3 Impedance spectroscopy measurements

Impedance spectroscopy is a powerful method to characterise many of the electrical properties of materials and their interfaces with electronically conducting electrodes (contacts in the scope of this thesis). The technique may be used to investigate the dynamics of bound and mobile charge in the bulk or interfacial regions of any kind of solid or liquid material: ionic, semiconducting, mixed electronic-ionic materials and even insulators (dielectrics) [19].

The technique consists of measuring the complex impedance as a function of frequency, from which the various contributions such as bulk, grain boundaries and electrode, to total conductivity can be separated. Fitting the experimental impedance data using either theoretical models or empirical equivalent circuits can isolate these contributions. In this thesis, the electrical properties and physical properties were correlated using equivalent circuit models. A succession of resistor-capacitor (R-C) parallel circuits in series was considered because many of the systems encountered in practice are actually modelled using this network [19].

When an alternating signal $v(\mathrm{t}) = V_m \sin(\omega \mathrm{t})$, with single frequency $f = \omega/2\pi$, is applied to a sample, the resulting steady state current $i(\mathrm{t}) = I_m \sin(\omega \mathrm{t} + \theta)$ is measured. Here θ is the phase difference between the voltage and the current; it is zero for purely resistive behaviour. The impedance $Z(\omega)$ is defined as:

$$Z(\omega) = \frac{v(\mathrm{t})}{i(\mathrm{t})} \qquad \text{(III.11)}$$

Its magnitude or modulus is $|Z(\omega)| = V_m/I_m(\omega)$ and its phase angle is $\theta(\omega)$.

The impedance $Z(\omega)$ is a complex number which can be represented either in polar or Cartesian co-ordinates:

$$Z(\omega) = |Z|\, e^{j\theta} \tag{III.12}$$

$$Z(\omega) = ReZ + j\, ImZ = Z' + jZ'' \tag{III.13}$$

where ReZ and ImZ are the real and imaginary part of the impedance respectively. The relationships between these quantities are:

$$ReZ = Z' = |Z| \cos\theta \tag{III.14}$$

$$ImZ = Z'' = |Z| \sin\theta \tag{III.15}$$

$$\theta = \arctan\frac{ImZ}{ReZ} \tag{III.16}$$

$$|Z|^2 = (ReZ)^2 + (ImZ)^2 \tag{III.17}$$

An idealized complex impedance plot and its equivalent successive R-C parallel circuit in series are shown in figure III.4.

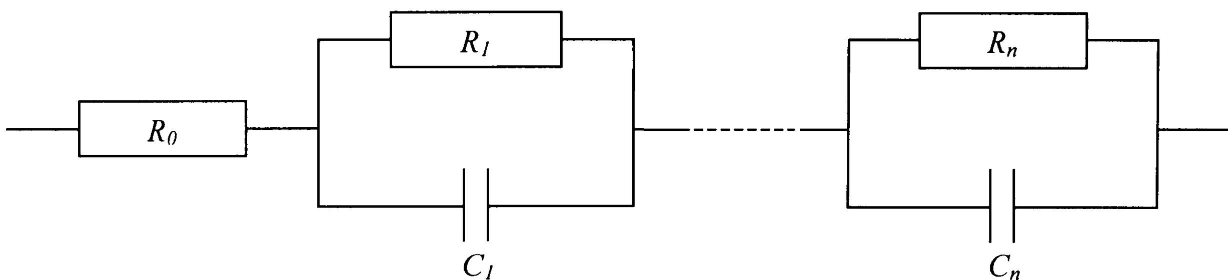

(a) Equivalent circuit

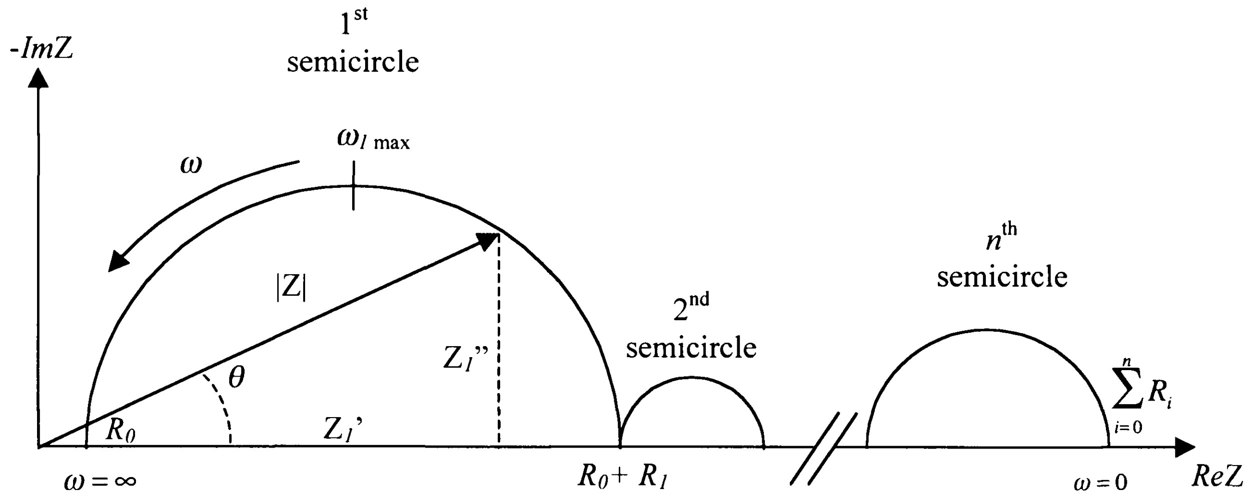

High frequency: $ImZ \rightarrow 0$, $ReZ \rightarrow R_0$

Low frequency: $ImZ \rightarrow 0$, $ReZ \rightarrow \sum_{i=0}^{n} R_i$

(b) Cole-Cole plot in the complex plane

Figure III.4: Idealized impedance plot of a sample showing n conduction paths: (a) equivalent circuit, (b) Cole-Cole plot in the complex plane.

The impedance of the system in figure III.4 is:

$$Z(\omega) = R_0 + \sum_{i=1}^{n} \frac{1}{\frac{1}{R_i} + jC_i\omega} = R_0 + \sum_{i=1}^{n} \frac{R_i}{1+\omega^2 C_i^2 R_i^2} - \sum_{i=1}^{n} \frac{j\omega C_i R_i^2}{1+\omega^2 C_i^2 R_i^2} \qquad \text{(III.18)}$$

where $i \in \mathrm{N}$ and n is the total number of conducting paths in the sample

R_i are the resistance values of the equivalent circuit

C_i are the capacitance values of the equivalent circuit

and $$|Z(\omega)| = \sqrt{\left(R_0 + \sum_{i=1}^{n} \frac{R_i}{1+\omega^2 C_i^2 R_i^2}\right)^2 + \left(\sum_{i=1}^{n} \frac{\omega^2 C_i^2 R_i^2}{1+\omega^2 C_i^2 R_i^2}\right)^2} \qquad \text{(III.19)}$$

when ω tends to zero, $|Z(\omega)|$ tends to $\sum_{i=0}^{n} R_i$

when ω tends to infinity, $|Z(\omega)|$ tends to R_0

The difference between the two limits is $R_0 - \sum_{i=0}^{n} R_i$ The series resistance R_0 is determined by the high frequency intercept, whereas the low frequency intercept yields $\sum_{i=0}^{n} R_i$, the sum of all the resistances. This means that at high frequencies, the capacitor acts as a wire and conducts the current easily. Consequently the impedance is solely due to the resistance R_0; whereas at low frequencies, the capacitor acts as an open-circuit and impedes the current flow. The current therefore flows through the different resistors and the impedance is given by the sum of the resistors. At intermediate frequencies, the impedance takes a value somewhere between R_0 and $\sum_{i=0}^{n} R_i$ and thus has both real and imaginary components. This gives rise to semicircular shapes in the Cole-Cole plot, each of which correspond to an equation. For the ith semicircle, the equation is:

$$\left[Z' - \left(\frac{R_i}{2} + \sum_{i=0}^{n-1} R_i\right)\right]^2 + [Z'']^2 = \left[\frac{R_i}{2}\right]^2 \qquad \text{(III.20)}$$

Equation (III.20) is analogous to the equation of a circle, with a radius of $\frac{R_i}{2}$ and a centre at $(\frac{R_i}{2} + \sum_{i=0}^{n-1} R_i$, 0). In all the materials studied, ω and the R_i values are greater than zero, thus resulting in semicircles on the axis when plotted as function of frequency. $Z(\omega)$ is plotted in

figure III.4(b) in terms of a Cole-Cole plot in the complex plane with the negative imaginary parts above the real axis, as is usually used in electrochemistry.

At the peak of the semicircle, the following condition is obtained:

$$\omega_{i\,\max} R_i C_i = 1 \qquad \text{(III.21)}$$

and hence

$$C_i = \frac{1}{2\pi f_{\max} R_i} \qquad \text{(III.22)}$$

Knowing the values of R_i and the frequency $f_{\max}$, the values of the capacitances C_i can be determined. It is possible to obtain all the parameters from the Cole-Cole plot as shown in figure III.4(b), provided a sufficient frequency range is investigated.

III.6. REFERENCES

[1] S. A. Grot, G. S. Gildenblat, and A. R. Badzian, IEEE Electron Device Lett. **13**, 462 (1992).

[2] G. S. Gildenblat, S. A. Grot, and A. R. Badzian, Proc. IEEE **79**, 647 (1991).

[3] S. A. Grot, G. S. Gildenblat, C. W. Hatfield, C. R. Wronski, A. R. Badzian, T. Badzian, and R. Messier, Electron Device Letters, IEEE **11**, 100 (1990).

[4] F. Fang, C. A. Hewett, M. G. Fernandes, and S. S. Lau, Electron Devices, IEEE Transactions on **36**, 1783 (1989).

[5] B. Baral, S. S. M. Chan, and R. B. Jackman, J. Vac. Sci. Technol. A-Vac. Surf. Films **14**, 2303 (1996).

[6] Y. Mori, Y. Show, M. Deguchi, H. Yagi, H. Yagyu, N. Eimori, T. Okada, A. Hatta, K. Nishimura, M. Kitabatake, T. Ito, T. Hirao, T. Izumi, T. Sasaki, and A. Hiraki, Jpn. J. Appl. Phys. Part 2 - Lett. **32**, L987 (1993).

[7] N. Jiang and T. Ito, J. Appl. Phys. **85**, 8267 (1999).

[8] T. Maki, S. Shikama, M. Komori, Y. Sakaguchi, K. Sakuta, and T. Kobayashi, Jpn. J. Appl. Phys. **31**, L1446 (1992).

[9] J. Ristein, F. Maier, M. Riedel, M. Stammer, and L. Ley, Diamond Relat. Mater. **10**, 416 (2001).

[10] S. G. Ri, T. Mizumasa, Y. Akiba, Y. Hirose, T. Kurosu, and M. Iida, Jpn. J. Appl. Phys. **34**, 5550 (1995).

[11] O. A. Williams, M. D. Whitfield, R. B. Jackman, J. S. Foord, J. E. Butler, and C. E. Nebel, Diamond Relat. Mater. **10**, 423 (2001).

[12] B. Koslowski, S. Strobel, M. J. Wenig, R. Martschat, and P. Ziemann, Diamond Relat. Mater. **7**, 322 (1998).

[13] P. E. J. Flewitt and R. J. Wild, *Physical Methods for Materials Characterisation* (Institude of Physics Publishing, Bristol, 1994).

[14] D. Clarkson, Electronics Today International **24**, 12 (1995).

[15] W. Zhu, in *Diamond: Electronic Properties and Applications*, edited by L. S. Pan and D. R. Kania (Kluwer Academic Press, Massachussets, USA, 1995).

[16] D. K. Schroder, *Semicondcutor Material and Device Characterization*, 2nd ed. (Wiley, New York, 1998).

[17] L. J. van der Pauw, Phil. Res. Rep. **13**, 1 (1958).

[18] L. J. van der Pauw, Phil. Tech. Rev. **20**, 220 (1958).

[19] J. R. Macdonald, *Impedance Spectroscopy: Emphasizing Solid Materials and Systems* (Wiley, New York, 1987).

[20] H. Ye, O. A. Williams, R. B. Jackman, R. Rudkin, and A. Atkinson, Phys. Status Solidi A-Appl. Res. **193**, 462 (2002).

CHAPTER IV
HOMOEPITAXIAL FILMS

IV.1. Introduction

IV.2. Experimental methods

IV.3. Results

IV.3.1. Homoepitaxy on diamond substrates having the same thickness

IV.3.2. Homoepitaxy on diamond substrates having a different thickness

IV.3.3. High growth rate

IV.4. Discussion

IV.5. Concluding remarks

IV.6. References

IV.1. INTRODUCTION

The emergence of chemical vapour deposition (CVD) techniques for the growth of large area free-standing diamond wafers led to considerable interest in the use of this commercially accessible material for active electronics [1-3]. However, to date, progress in this topic has been severely hindered by the polycrystalline nature of such films and difficulty with efficient incorporation of suitable dopant species. Whilst homoepitaxial growth of diamond has been widely demonstrated, substrate cost and dopant incorporation again limit the impact that such material can have on commercial electronic device applications. However, the discovery of *p*-type surface conductivity on hydrogen terminated diamond has dramatically changed the position regarding doping [4]. The appearance of high hole concentrations at, or near, the surface using this approach requires little thermal activation. This is in sharp contrast to other processes such as the incorporation of boron [5]. This property has been used to fabricate some of the most promising diamond-based electronic devices reported over the past few years [6-8]. Whilst

surface hydrogenation is required, it alone is insufficient for the formation of the *p*-type layer; metallic deposits and/or atmospheric adsorbates are additionally required [9,10]. Whilst a lot of recent research effort has concentrated on elucidating the mechanism behind the formation of this *p*-type layer, less attention has been paid to how the density of generated carriers may be controlled. This is important if this technique for carrier generation is to make further progress in terms of advanced device designs, since the design engineer will need to be able to locally control the carrier density that is present. Attempts to control the characteristics of the *p*-type layer by varying the nature of the hydrogenation process have proved mostly futile, with little evidence that, for example, longer hydrogenation periods yield higher carrier levels. Similarly, little control can be achieved by varying the type of diamond used, with single crystal and polycrystalline films revealing surprisingly similar carrier transport characteristics [11,12]. In fact, only when there is a significant level of nitrogen within the diamond does the formation of a *p*-type layer not readily occur [13]. It is from this position that the work presented in this chapter takes its start. HPHT produced Ib single crystal diamonds do not support a *p*-type surface conductive layer following hydrogenation. However, following homoepitaxial growth, strong *p*-type characteristics can be measured on the 'as-grown' films, as shown in §IV.3.1. Similarly, results were obtained on polycrystalline material, as detailed in §IV.3.2. The problem of low growth rates has also been addressed in §IV.3.3, where rates as high as 50 μm/h have been achieved.

A systematic study of the carrier transport characteristics has been carried out, as judged by Hall effect measurements, of 'as-grown' homoepitaxial layers grown on Ib HPHT stones and on polycrystalline diamonds. A clear correlation between overlayer thickness and carrier density has been demonstrated, enabling the device engineer to 'tune' the characteristics of the device structure being made by the choice of overlayer thickness used. Moreover, it was found that surface roughness, both of the HPHT stone and the resultant overlayer, influence the nature of the *p*-type layer formed, and hence control over this parameter must also be exercised. In addition to Hall effect measurements, scanning

electron microscopy (SEM) and scanning tunnelling microscopy (STM) data will be presented. Homo-growth parameters will be revealed for the high growth rates.

IV.2. EXPERIMENTAL METHODS

Homoepitaxial films of various sizes (4-100 mm^2) were deposited on several diamond substrates by microwave plasma enhanced chemical vapour deposition. Sumitomo/Element 6 type Ib {100}/{111} oriented HPHT single crystals were used together with Diamonex HFCVD randomly oriented polycrystalline black diamonds. All these substrates contained substantial nitrogen levels so that hydrogen plasma treatment of the surface alone was not sufficient to produce surface conductivity. Therefore a thin epitaxial layer of high purity diamond was required if surface conductivity was to be observed [13]. Prior to deposition, all the substrates were acid dipped using the process described in section III.2.1. in order to get a surface free of graphitic and any other metallic contaminants that could have arisen from the HPHT process. All films were grown in an Astex PDS-18 plasma deposition system, with a 2.45 GHz 5kW microwave source and a cooled stage. Temperature measurements were made using a Williamson Pro 92 two-colour pyrometer. The growth conditions were 800°C, 120 torr, 2.5-3 kW, with gas flows of 478 sccm hydrogen and 20 sccm methane. Some homolayers were also deposited using an extra flow of 2 sccm oxygen. The temperature was controlled by the incident power. These conditions yield a growth rate in the range 8-50 μm/h [14]. The substrates were ramped to the final microwave power and temperature in an hydrogen plasma to clean the surface and to reduce the misalignment angle [15]. Once the system was stable, the methane gas was added and the microwave power adjusted to stabilise the temperature at 800°C. After the deposition duration, the samples were cooled in an hydrogen plasma. This process is known to remove any non-sp^3 carbon from the surface as a result of the interrupted growth process and generates the *p*-type surface conductivity. However, AFM measurements have revealed that occasionally small graphitic deposits remain on the surface after cooling in hydrogen

ambient. Au contacts were thermally evaporated in the van der Pauw configuration in an Edwards E306 evaporator at a base pressure lower than 2×10^{-7} mbar. Hall measurements were carried out using a modified Lakeshore Cryonics 7504 Hall measurement system, with an advanced research helium atmosphere based cryostat. The surface of the homoepitaxial diamond films have been characterised by STM and SEM. STM measurements were made in air using a nanosurf Easyscan STM under a tip bias of 0.05V with a tip current of 1 nA; the surface conductive layer of the film was connected to ground using silver paint. SEM images of the film surface were obtained using a JEOL 35 CF system.

IV.3. RESULTS

IV.3.1 Homoepitaxy on diamond substrates having the same thickness

Figure IV.1 demonstrates the quality of the surface for homoepitaxial films grown on type Ib HPHT Sumitomo {100} diamond substrates originating from the same batch, using STM. This was to ensure that all the diamond substrates had the same thickness. Figures IV.1(a) and IV.1(b) show respectively the STM images of a 1 μm and 8 μm thick film. The roughness of the 1μm thick film is less than 1 nm and is comparable to that of the substrate. The STM image is also very uniform over this area. On the other hand, the surface of the 8 μm homolayer is significantly rougher, with some particulates on the surface, which could be non-epitaxial crystallites.

(a)

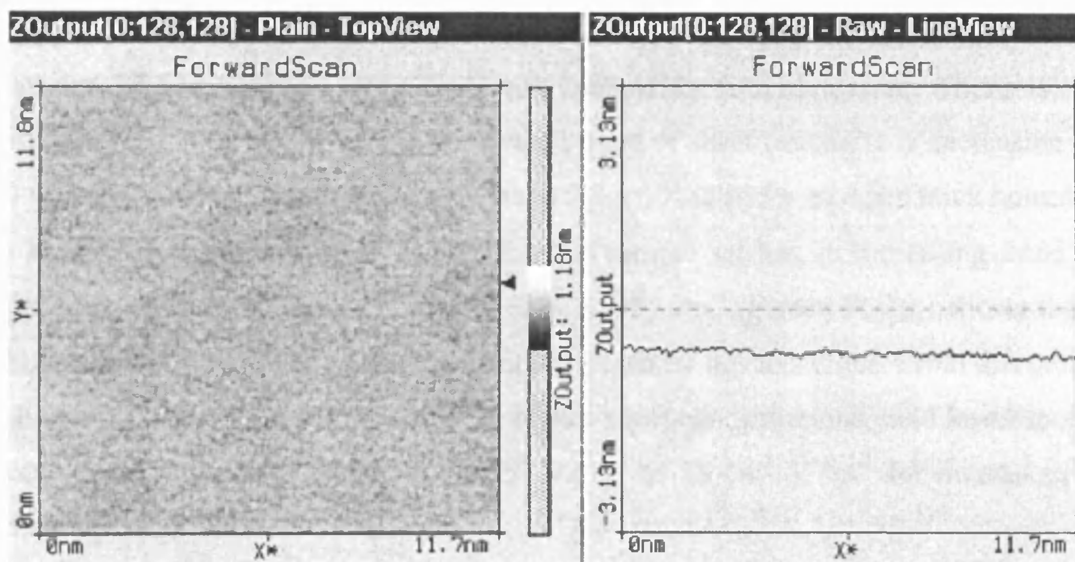

(b)

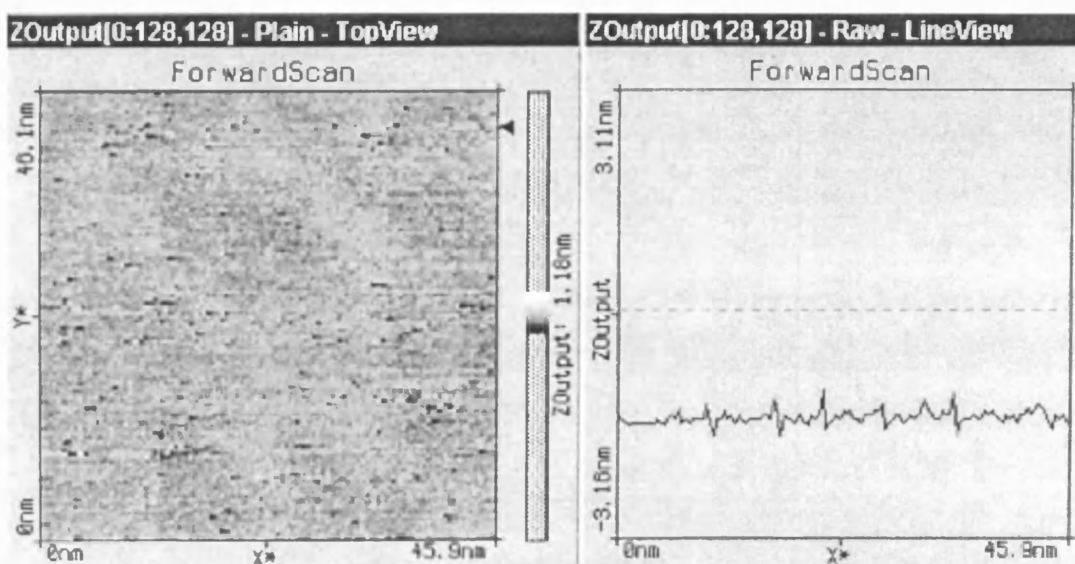

Figure IV.1: STM images of (a) a 1 μm and (b) a 8 μm thick homoepitaxial diamond film grown on HPHT type Ib {100} Sumitomo substrates.

Homoepitaxial films of different thickness were grown, the effect on the Hall characteristics is illustrated in figure IV.2. It can be seen from this figure that the sheet resistivity (figure IV.2(a)) decreases with increasing film thickness. There is some significant scatter on this trend, but the overall trend of sheet resistivity is decreasing from 17.9×10^3 Ω/sq for a 1μm thick homolayer to 7.5×10^3 Ω/sq for an 8 μm thick homolayer. The sheet carrier concentration figures for this sample set has an increasing trend with values ranging from 2.49×10^{12} cm^{-2} to 2.54×10^{13} cm^{-2}. Figure IV.1(c) shows that the mobility against film thickness for the samples grown by this technique. From this graph, it can be seen that the values correlates, i.e. higher sheet concentrations yield lower mobility values. These values range from 140 cm^2 V^{-1} s^{-1} to 18 cm^2 V^{-1} s^{-1} for increasing film thickness.

(a)

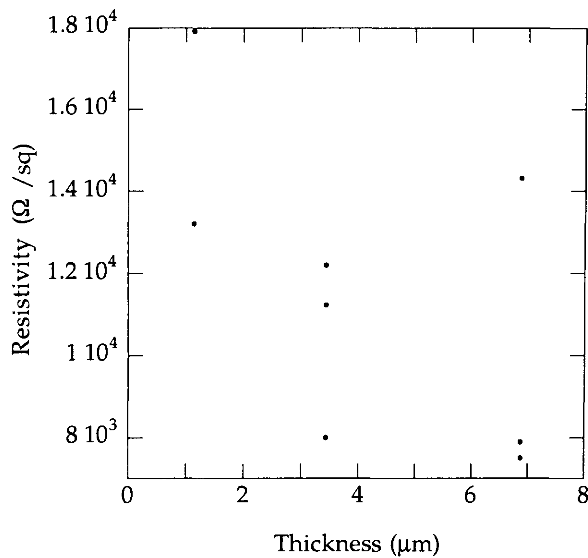

(b)

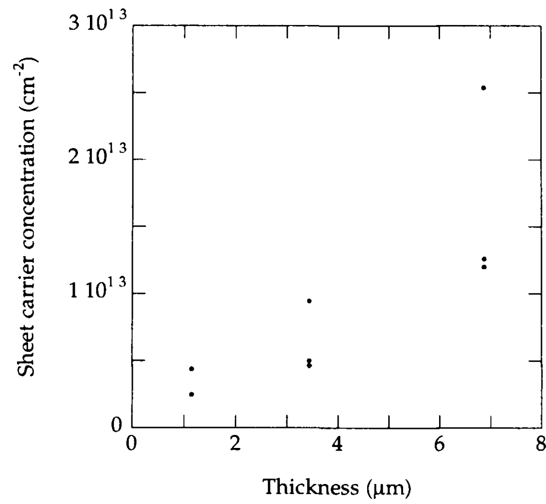

(c)

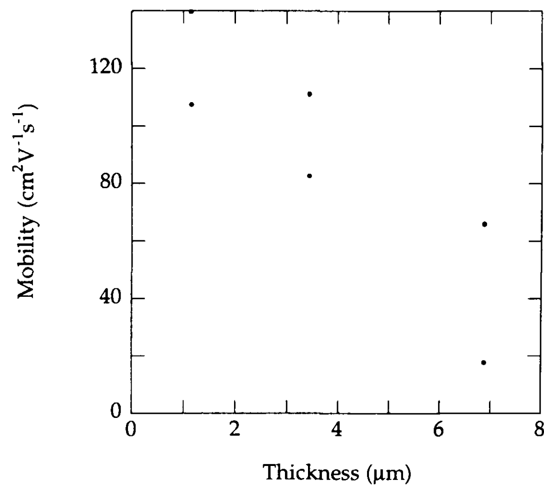

Figure IV.2: (a) the sheet resistivity, (b) the sheet carrier concentration and (c) the mobility against thickness for homoepitaxial diamond films grown on HPHT type Ib {100} Sumitomo substrates.

IV.3.2 Homoepitaxy on diamond substrates having a different thickness

A similar approach was used on black polycrystalline HFCVD diamond substrates. This material has the advantage of much lower cost and offers the possibility of large area deposition. A 1µm thick film was grown on this material whose substrate thickness varied from 100 µm to 1000 µm. SEM pictures of these films are shown in figure IV.3 for substrate thicknesses between 100 µm and 500 µm. The average grain size on the top side of the substrate increases from 10 µm to 60 µm with film thickness. This trend is in accordance with the observations made when polycrystalline diamond films are grown thicker. Figure IV.4 shows an STM image of a homoepitaxial film grown on a 300 µm thick substrate. It can be seen from this figure that even though the structure of the film is fundamentally polycrystalline, the image is bright and uniform within the grain and somewhat darker at the grain boundaries.

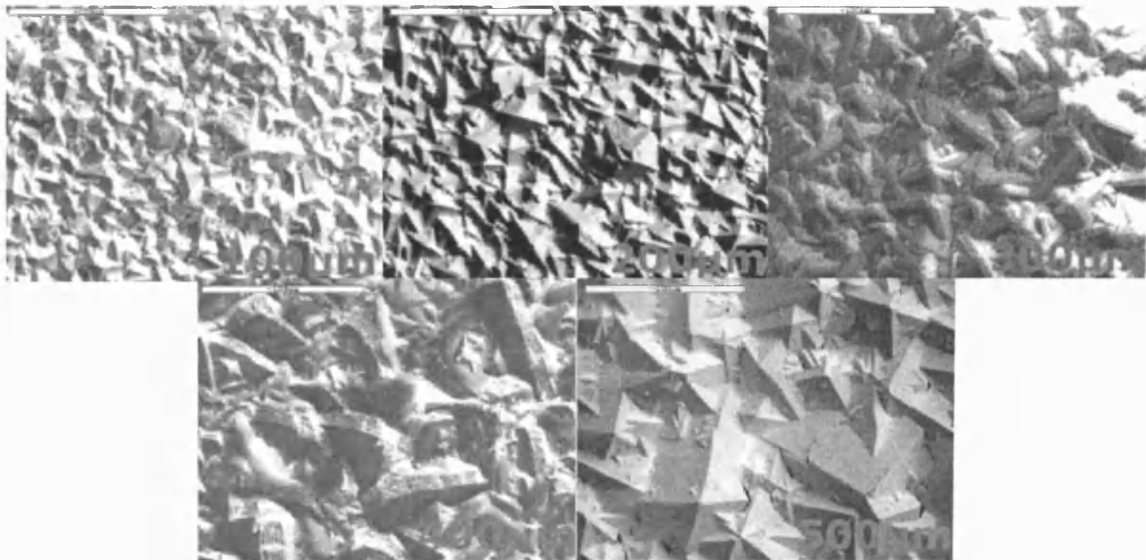

Figure IV.3: SEM pictures of a 1 µm thick homolayer grown on HFCVD polycrystalline black diamond substrates. The thickness of the substrate is indicated at the bottom right of each SEM image.

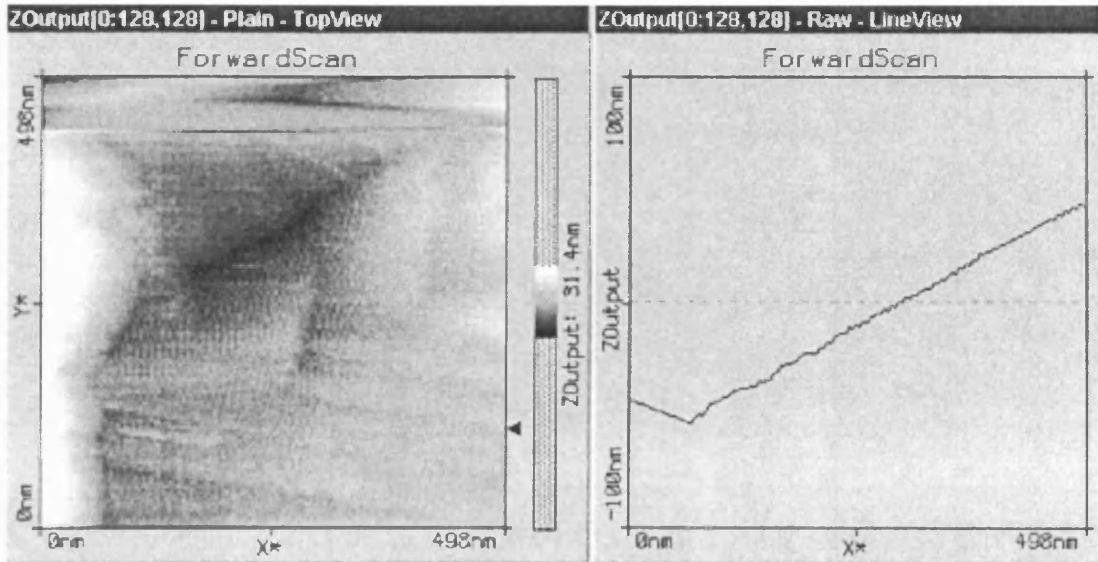

Figure IV.4: STM image of a 1 μm thick film grown on a 300 μm HFCVD polycrystalline black diamond substrate.

The sheet resistivities of these films are plotted in figure IV.5(a), revealing a decrease with increasing substrates thickness from 7.2×10^5 to 3.8×10^3 Ω/sq. This decrease is accompanied by an increase in sheet carrier concentration from 5.6×10^{12} to 9.6×10^{13} cm^{-2} (see figure IV.5(b)). The associated mobilities are plotted in figure IV.5(c). Their values are between 12 and 26 cm^2 V^{-1} s^{-1}. Unlike in the previous section, there is no evident trend emerging from this data as the points are scattered.

(a)

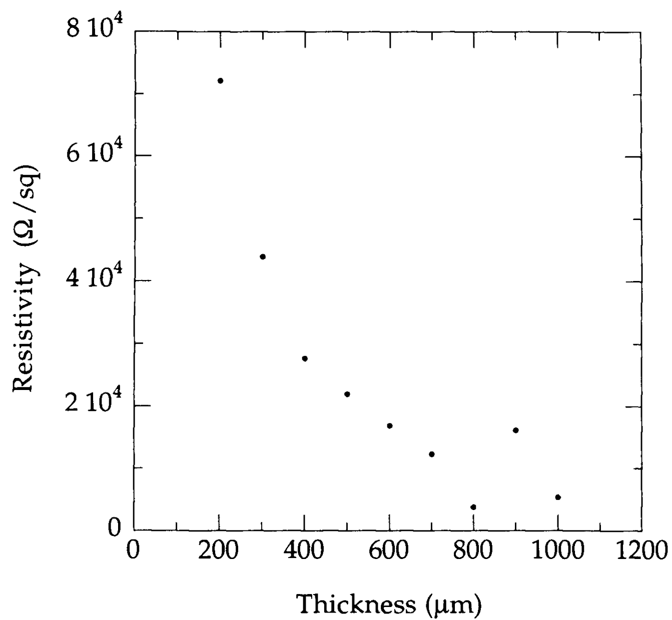

(b)

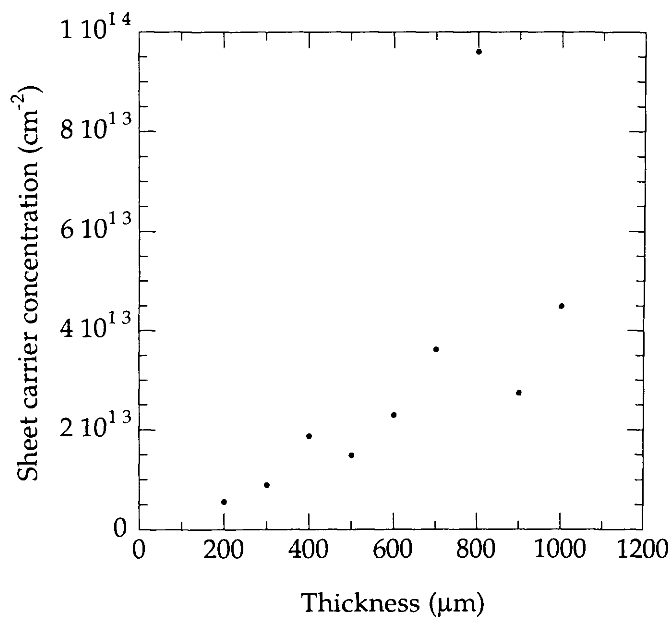

(c)

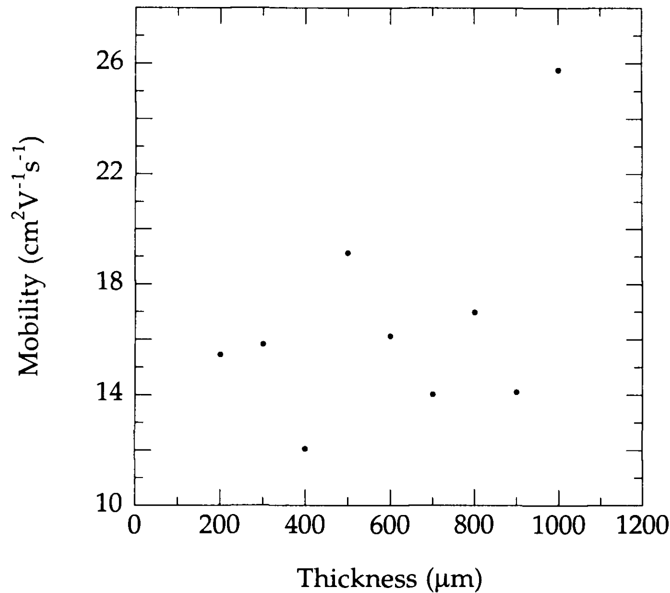

Figure IV.5: (a) the sheet resistivity, (b) the sheet carrier concentration and (c) the sheet mobility against substrate thickness for a 1 μm thick film grown on HFCVD polycrystalline black diamond.

IV.3.3 High growth rates

Films grown at high growth rates were deposited on HPHT type Ib {100} Sumitomo substrates, all of the same thickness. Table IV.1 lists the growth parameters and the growth rates achieved under these conditions. Regime 1 at 800°C, produced films at a moderate growth rate with flat surfaces (see figure IV.1), which yielded high mobility and sheet carrier concentration values (140 $cm^2V^{-1}s^{-1}$ at 2.5×10^{12} cm^{-2}). Figure IV.6 shows SEM images of films grown under regime 2 and 3. The surface of these later films was much rougher than that obtained by regime 1 due to the terraced structure that is observed under these growth conditions.

	Regime 1	Regime 2	Regime 3
Pressure	120 Torr	150 Torr	170 Torr
Power	3 kW	2.65 kW	2.52 kW
Gas Phase	4% CH_4+0.4%O_2+95.6%H_2	4% CH_4+ 96 %H_2	7% CH_4+ 93% H_2
Temperature	800°C	850°C	800°C
Growth Rate	10 μm/h	20 μm/h	50 μm/h

Table IV.1: Process conditions used for the growth of homoepitaxial diamond films on HPHT type Ib {100} Sumitomo substrates.

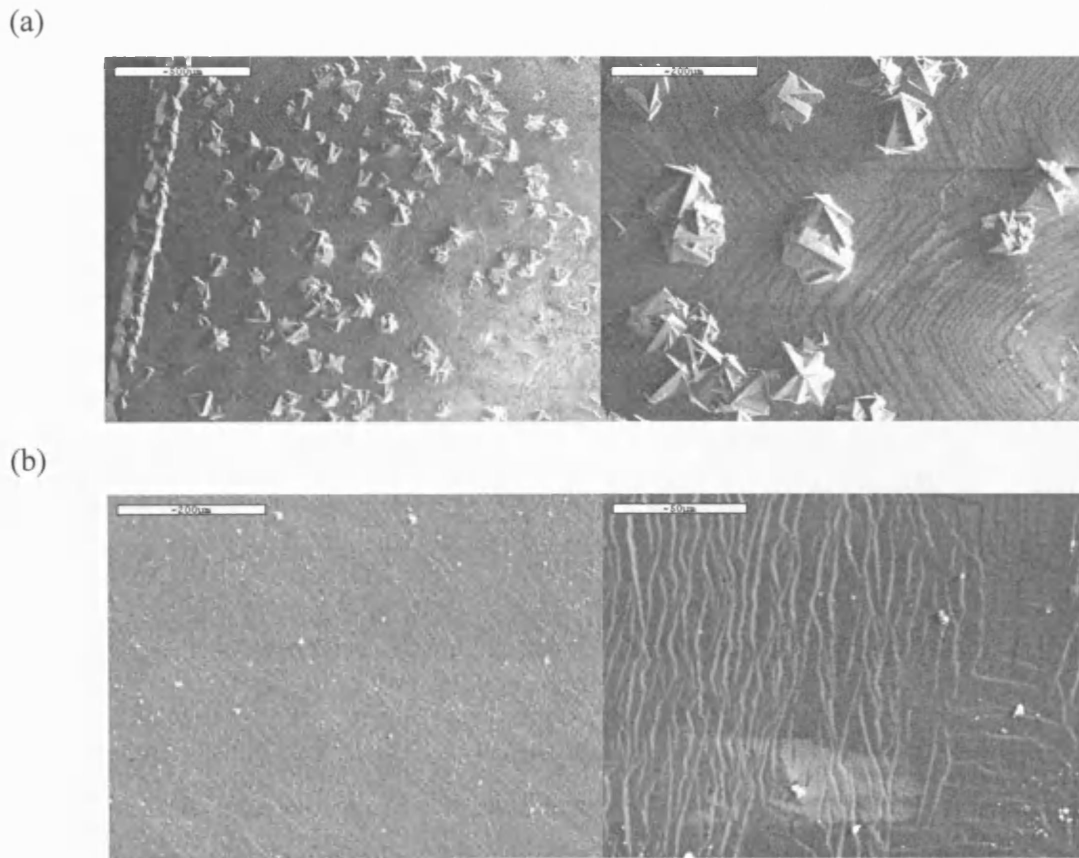

Figure IV.6: SEM images at different magnifications for (a) a film grown at 850°C under regime 2 and (b) a film grown at 800°C under regime 3.

Regime 2 has led to the formation of a high density of non-epitaxial crystallites in the [111] and [110] directions (see figure IV.6(a)). This happened as the temperature reached 850°C during growth due to the inadequacy of the cooling of the substrate. After redesign of the sample holder, it was possible to grow samples at a lower temperature of 800°C under regime 3 so that secondary nucleation was totally suppressed (see figure IV.6(b)). Hall measurements on a film grown using regime 3 showed that the film had reasonable carrier mobilities (~40 $cm^2\ V^{-1}s^{-1}$ at $1 \times 10^{13}\ cm^{-2}$) due to surface conductivity, but inferior to those films grown in regime 1. An STM image of a typical film grown under regime 3 can be seen in figure IV.7. The ridges due to macro step bunching are clearly visible, with a magnitude between 10 and 20 nm per step. It was impossible to perform similar measurements on the films grown by regime 2, due to the extreme roughness of the surface.

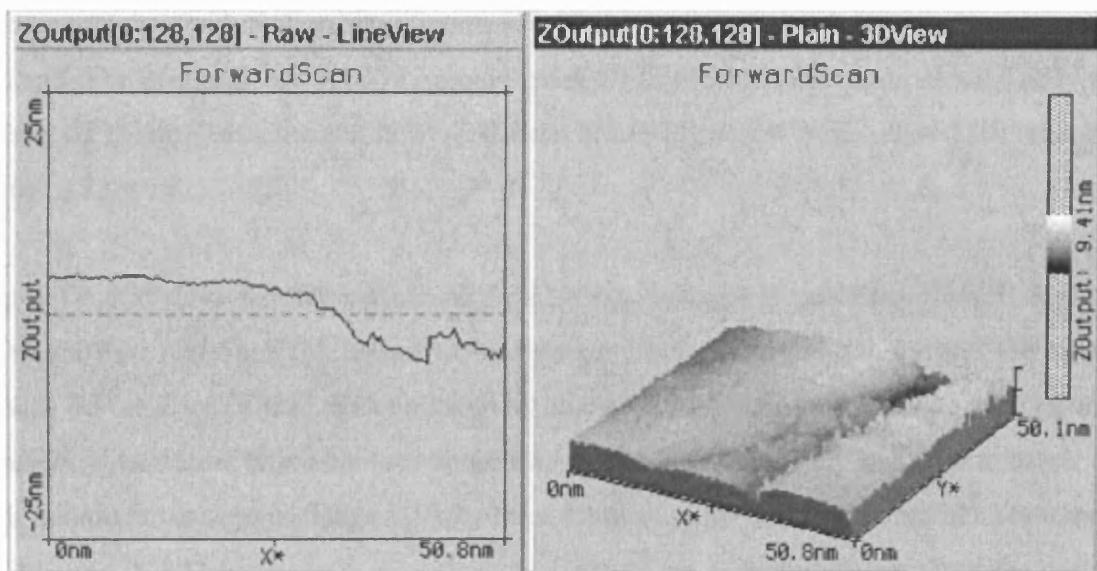

Figure IV.7: STM image of a film grown on a HPHT type Ib {100} Sumitomo diamond substrate at 800°C under regime 3, showing ridges due macro step bunching.

IV.4. DISCUSSION

The growth of homolayers on commercially cheap, low quality diamond substrates is a viable approach for the production of high quality electronic grade material for surface conductive device applications. The origin of this surface conductivity is well documented and has been reviewed elsewhere (see § V.2). Briefly, both the conductivity and the carrier transport observed here are due to the dipole formed by the differing electronegativities of the carbon and hydrogen atoms at the hydrogen terminated surface [16]. It is thought that holes are created in the near-surface region by electron out-diffusion into an adsorbate layer at the diamond surface [9,17,18]. These holes are confined to the near surface by negative charge at the carbon atom in the dipole. At low temperatures, the holes have little thermal energy and become increasingly confined at the surface. To propagate, these holes have to be thermally excited. Hall measurements revealed that the activation energy for this process is small. For instance, for {100} homoepitaxial CVD films, a sheet hole density activation energy of 16 meV was measured by Williams *et al* [19] whilst Nebel *et al.* [20] reported a value of 23 meV.

Figure IV.1(a) show that the surface of the {100} homolayer is extremely smooth. It should be noted that for the STM image to be uniform, both the conductivity and the surface should be uniform. Thus, the conductivity due to hydrogen surface conductivity can be considered uniform. This becomes less true as the roughness of the surface increases with film thickness, as seen in figure IV.1(b) for a 8 μm thick film, where numerous features are visible in the STM. These features are thought to be non-epitaxial crystallites and are characterised by crystallographic faces different from those of the surface the homoepitaxial layer is grown from. In this instance, these non-epitaxial crystallites would be bound by facets, whose crystallographic orientation is other than in the <100> directions. Kawarada [16] has showed that {100} surfaces have a larger density of dangling bonds than other crystallographic planes. Thus, there are more sites for electron out diffusion into the adsorbate layer on the {100} surface than on the facets of the non-

epitaxial crystal. As a consequence, the conductivity of these non-epitaxial crystals is lower, which is observed here by the dark features on the STM.

Hall measurements on the {100} homolayers showed that the sheet carrier density is increasing with film thickness (see figure IV.2(b)). This trend is not generally expected in hydrogen surface conductivity, where carriers have been reported to be confined to a maximum of the first 50 nm from the surface [21]. One possible cause is that the holes due to the hydrogen termination are compensated by deep traps due to the high concentration of nitrogen in the type Ib substrate. This would explain why thicker layers have a higher carrier concentration, because the layer would be growing away from this region. However, this explanation is not sufficient, as it has been empirically shown by others that only a very thin layer (~15 nm) is necessary to achieve high sheet carrier densities (~1×10^{13} cm^{-2}) [13]. What was not reported in this work though was the surface roughness of the resulting film. From STM measurements (figure IV.1), the roughness of the {100} homoepitaxial film here is increasing with film thickness. While the film is still rather smooth, this increased roughness means there is a substantial increase in surface area. With a larger surface area, there will be an increase in the number of surface hydrogen bonds. This will allow more electron out diffusion into any adsorbate layer, resulting in an increased density of holes in the near surface and hence a higher sheet carrier concentration [12].

Inspection of figure IV.2 shows that the increase in sheet carrier density with thickness is accompanied by a decrease in mobility. The origin of this effect cannot be due to increased ionized impurity scattering as the surface conductivity is not a conventional form of doping. Instead, if the increased sheet carrier concentration is due to increasing confinement of the surface dipole, then the mobility can be reduced by the increase of Coulomb interaction and the scattering due to the surface roughness.

Similar effects are seen with growth on polycrystalline diamond, but with the added complication of grain boundaries. Figure IV.4 shows it is possible to obtain STM images

on this macroscopically rough material. This image shows a grain boundary and a grain on either side of it. The grain area is light and reasonably uniform, as it is within a single crystal. However, the uniformity is not as high as in the case of the single crystal shown in figure IV.1. The grain boundary is darker because there are less dangling bonds for hydrogen atoms to bond to. Thus the conductivity is this region is reduced compared to that of the surface of grain. Therefore, when hydrogenated, polycrystalline diamond films should be more resistive in general, and this is borne out in the empirical case [12,22,23]. Figure IV.5(a) demonstrates the reduction in sheet resistivity with substrate thickness. Initially these data are confusing, until one considers the fact that grain size increases with thickness in the case of polycrystalline diamond. This will in turn reduce the total area of grain boundaries, and there will be an increased area for hydrogen termination if one assumes each grain as an isolated single crystal. This is seen in figure IV.5(b) where the sheet carrier concentration increases with increasing thickness of substrate and hence increased grain size. Although there is no trend in mobility for the polycrystalline sample set, it can be noticed that the mobility values are lower than their single crystal counterparts. This could be due to the mobility being limited by grain boundary scattering. Furthermore, the scatter in the data points (see figure IV.5(c)) can be attributed to the variation in substrate material as it should be noted that one 300 μm film can have a very different morphology from another and this will have substantial effects on the surface conductivity.

Hall measurements showed that films grown under regime 1 have carrier transport properties (figure IV.2), which are amongst the highest recorded for surface conductive diamond [12,23]. This is in part due to the very low surface roughness of the films obtained using these growth conditions. The conductivity is also very uniform, as deduced from the uniformity of the STM image of figure IV.1. Growth in regime 1 is adequate for material for electronic applications as it represents a good compromise between growth rate and carrier transport values. However the achievable growth rate is still too low and would not be economically viable if technological applications such as thermal management

applications had to be considered, unless deposition of such films could be done over large areas. With this reactor it would be possible to grow over 2 inch diameter homoepitaxial diamond films in this regime. Growth in regime 2 and 3 represent better alternatives for a wider range of applications, albeit with a lower maximum area coverage. Under these conditions, it is possible to grow diamond films up to 50 μm/h with the penalty of increasing the surface roughness. Higher rates could be achieved by addition of nitrogen [24,25], but at the detriment of losing surface conductivity. It can be seen from figure IV.6(a) that high temperatures result in secondary nuclei, and this effect was seen regardless of the gas phase pressure used. Reducing this effect can be difficult, as increasing the pressure and methane concentration results in an increase in temperature. In order to reduce the temperature, it is necessary to decrease the microwave power. This results in a smaller plasma and hence a smaller maximum area of growth. For homoepitaxy this does not present a problem since most diamond crystals used are less than 5×5 mm, due to cost limitations. However, overheating is still a major problem with this technique, and this required the redesign of the substrate holder to suppress the level of secondary nuclei to the level seen in Fig.IV.6b, where they are no longer visible. Even with the secondary nuclei suppressed, the surface of the films grown at the higher rates (20-50 μm/h) was not as smooth as those grown at lower growth rates, as seen by macro step bunching in figures IV.6(b) and IV.7.

IV.6. CONCLUDING REMARKS

The growth of electronic grade quality diamond films for surface conductive device applications has been carried out using microwave plasma enhanced chemical vapour deposition. High growth rates up to 50 μm/h have been achieved using this process. Furthermore, this growth process was used as a way to control the carrier transport statistics of these films. Electrical characterisation of the surface conductive properties has shown that sheet carrier concentration and mobility values were associated with surface roughness,

which becomes greater with film thickness. It is proposed that the rougher films have an enhanced surface area, and hence more surface hydrogen bonds by which electrons can out-diffuse into a surface based adsorbate layer. This would lead to a higher sheet carrier concentration whilst the mobility is reduced by the roughness of the surface.

This method allows the production of an electronic device grade film from a low quality substrate within a little time. A similar process has been demonstrated on polycrystalline material, but the maximum achievable mobility is significantly lower due to grain boundary scattering. However, considerably larger area material may be realised by this technique.

IV.7. REFERENCES

[1] H. J. Looi, M. D. Whitfield, J. S. Foord, and R. B. Jackman, Thin Solid Films **344**, 623 (1999).

[2] M. Aoki and H. Kawarada, Jpn. J. Appl. Phys. **33**, L708 (1994).

[3] H. Umezawa, H. Taniuchi, T. Arima, M. Tachiki, and H. Kawarada, Diamond Relat. Mater. **10**, 1743 (2001).

[4] M. I. Landstrass and K. V. Ravi, Appl. Phys. Lett. **55**, 975 (1989).

[5] K. Hayashi, S. Yamanaka, H. Okushi, and K. Kajimura, Appl. Phys. Lett. **68**, 376 (1996).

[6] H. Umezawa, T. Arima, N. Fujihara, H. Taniuchi, H. Ishizaka, M. Tachiki, C. Wild, P. Koidl, and H. Kawarada, Jpn. J. Appl. Phys. Part 1 - Regul. Pap. Short Notes Rev. Pap. **41**, 2611 (2002).

[7] H. Taniuchi, H. Umezawa, T. Arima, M. Tachiki, and H. Kawarada, IEEE Electron Device Lett. **22**, 390 (2001).

[8] D. Takeuchi, S. Yamanaka, and H. Okushi, Diamond Relat. Mater. **11**, 355 (2002).

[9] F. Maier, M. Riedel, B. Mantel, J. Ristein, and L. Ley, Phys. Rev. Lett. **85**, 3472 (2000).

[10] J. A. Garrido, C. E. Nebel, M. Stutzmann, E. Snidero, and P. Bergonzo, Appl. Phys. Lett. **81**, 637 (2002).

[11] C. E. Nebel, F. Ertl, C. Sauerer, M. Stutzmann, C. F. O. Graeff, P. Bergonzo, O. A. Williams, and R. B. Jackman, Diamond Relat. Mater. **11**, 351 (2002).

[12] O. A. Williams and R. B. Jackman, Semicond. Sci. Technol. **18**, S34 (2003).

[13] J. Ristein, M. Riedel, M. Stammler, B. F. Mantel, and L. Ley, Diamond Relat. Mater. **11**, 359 (2002).

[14] O. A. Williams and R. B. Jackman, Diamond Relat. Mater. **13**, 557 (2004).

[15] S.-G. Ri, H. Yoshida, S. Yamanaka, H. Watanabe, D. Takeuchi, and H. Okushi, Journal of Crystal Growth **235**, 300 (2002).

[16] H. Kawarada, Surf. Sci. Rep. **26**, 205 (1996).

[17] J. Shirafuji and T. Sugino, Diamond Relat. Mater. **5**, 706 (1996).

[18] S. G. Ri, T. Mizumasa, Y. Akiba, Y. Hirose, T. Kurosu, and M. Iida, Jpn. J. Appl. Phys. **34**, 5550 (1995).

[19] O. A. Williams and R. B. Jackman, Diamond Relat. Mater. **13**, 325 (2004).

[20] C. E. Nebel, C. Sauerer, F. Ertl, M. Stutzmann, C. F. O. Graeff, P. Bergonzo, O. A. Williams, and R. B. Jackman, Appl. Phys. Lett. **79**, 4541 (2001).

[21] A. Denisenko, A. Aleksov, A. Pribil, P. Gluche, W. Ebert, and E. Kohn, Diamond Relat. Mater. **9**, 1138 (2000).

[22] K. Hayashi, H. Watanabe, S. Yamanaka, H. Okushi, K. Kajimura, and T. Sekiguchi, Diamond Relat. Mater. **6**, 303 (1997).

[23] O. A. Williams, M. D. Whitfield, R. B. Jackman, J. S. Foord, J. E. Butler, and C. E. Nebel, Appl. Phys. Lett. **78**, 3460 (2001).

[24] C. S. Yan, Y. K. Vohra, H. K. Mao, and R. J. Hemley, Proceedings of the National Academy of Sciences **99**, 12523 (2002).

[25] W. Muller-Sebert, E. Worner, F. Fuchs, C. Wild, and P. Koidl, Appl. Phys. Lett. **68**, 759 (1996).

CHAPTER V
PASSIVATION OF HYDROGENATED DIAMOND SURFACES

V.1. Introduction
V.2. Electronic properties of hydrogen-terminated diamond surfaces
V.3. Experimental methods
V.4. Results
V.5. Discussion
V.6. Summary
V.7. References

V.1. INTRODUCTION

Hydrogen can modify the electronic properties of diamond. In particular hydrogen at the surface of either polycrystalline or single crystal diamond leads to *p*-type surface conductivity as judged by Hall measurements [1]. Despite intensive work in this field the origin of this effect is not yet fully understood and remains controversial. The models proposed are reviewed in §V.2. below.

Several devices have been fabricated using this *p*-type conductive layer. Schottky diodes display high rectification ratios, near unity ideality factors and high reverse breakdown values [2,3]. Transistors have also been produced with good transconductance values and high power handling capability; relatively high frequency switching has also been demonstrated [4,5]. These devices have been shown to be capable of operation at temperatures up to 250°C in air. Unfortunately, at higher temperatures, the *p*-type character and hence the device operation, is lost when the devices are operated in air. Passivation of these layers becomes a requirement to counter this problem if useful devices are to emerge from this technology.

This chapter investigates the use of both inorganic (Calcium Fluoride) and organic materials (photoresist) as passivation layers. In addition, olive oil has been considered as a protective coating.

V.2. ELECTRONIC PROPERTIES OF HYDROGEN-TERMINATED DIAMOND SURFACES

Hydrogen-terminated diamond surfaces are many orders of magnitude more conductive than those that are oxygen terminated. Lanstrass *et al.* in 1989 have measured resistivities of the order of 10^6 Ω cm in "as grown" CVD diamond films [6] and of the order of 10^5 Ω cm in natural diamonds that have been subjected to the action of atomic hydrogen in a hydrogen plasma [7]. The low resistivity of the hydrogenated samples was thought to be due to the passivation of interband states in the crystal. Landstrass *et al.* have also observed that the conductivity of the hydrogenated samples was lost following thermal annealing but that it could be retrieved following rehydrogenation. These observations have led to the conclusion that the change in resistivity is a reversible process by hydrogenation and annealing treatment. The mechanism leading to the formation of this kind of surface conductivity is not fully understood yet and several controversial models have been proposed. The current understanding of this field is outlined below.

Albin *et al.* [8] were one of the first groups after Landstrass *et al.* to investigate the electrical properties of hydrogenated diamond. Their study was based on current-voltage (I-V) characterisation of polycrystalline thin film and bulk diamond before and after hydrogenation. Like their predecessors, they have observed that the samples were more conductive by several orders of magnitude following hydrogenation. The conductivity was thought to be due to trap compensation as hydrogen is diffusing into the diamond film during hydrogenation. This theory was supported by Muto *et al.* [9] who have explained the increase of conductance in hydrogenated diamond by the passivation of traps at 0.62 eV

and 1.38 eV. In a later publication the same group proposed another model, known as the "band bending model" based on Kelvin probe and X-ray photoelectron spectroscopy measurements [10]. This model suggests that hydrogen-terminated surfaces show upward energy band bending which results in the formation of a hole accumulation layer. In contrast, oxygen-terminated surfaces show downward band bending so that a depletion layer for holes is formed. In order for such surface band bending to occur, acceptor-type surface states must be present well below the bulk Fermi level for the accumulation layer to be formed in the case of hydrogenated surfaces, and donor-type surface states above the valence band are required for a hole depletion layer to be formed in the case of oxygenated surfaces. Although this model did not account for the origin of these surface states, an hypothesis was made that surface defects, which may not be directly associated with adsorbates, may be responsible for band bending. This model is illustrated in figure V.1.

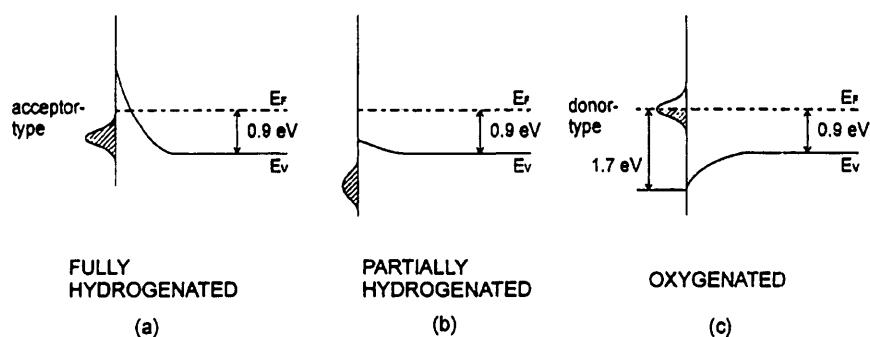

Figure V.1: Energy band diagrams of undoped diamond surfaces: (a) fully hydrogenated, (b) partially hydrogenated and (c) oxygenated surfaces. (Reproduced from Ref. [10])

In an effort to clarify the origin of the high conductivity layer formed in the hydrogenated diamond, Hayashi *et al.* [11] have investigated the effect of hydrogen on electrical and optical properties of homoepitaxial CVD diamond films. Hall effect measurements have been carried out in the temperature range 120-400K and showed that the conducting surface layer of hydrogenated diamond was *p*-type. The carrier density per unit area was around

10^{13} cm^{-2} at 297K and remained nearly constant over the temperature range. A hole concentration of 2×10^{18} cm^{-3} was derived assuming a thickness of 20 nm, which is the distance from the surface where a high density of hydrogen was observed using secondary ion mass spectroscopy (SIMS). The mobility was measured to be 30 cm^2/Vs at 297K and was proportional to $T^{1.1}$. This relationship suggests that the incorporated hydrogen in the subsurface region of hydrogenated samples generate shallow acceptor levels. The authors have also carried out cathodoluminescence (CL) measurements. The CL spectra showed a broad peak at around 540 nm in the near surface of hydrogenated films which disappears after subsequent oxidation treatment, indicating the existence of deep hydrogen-related gap states in the subsurface region in addition to the shallow acceptor states. An alternative model was therefore proposed in which the energy-band diagram is equivalent to a p^+-i junction, as illustrated in figure V.2. The Fermi level E_f of the p^+ region is located close to the valence band due to the high concentration of holes, resulting in upward movement of the valence band of the surface region. The main difference with the model proposed by Shirafuji *et al.* (see figure V.1) is the existence of both deep and shallow hydrogen-related gap states in the near surface of hydrogenated diamond films.

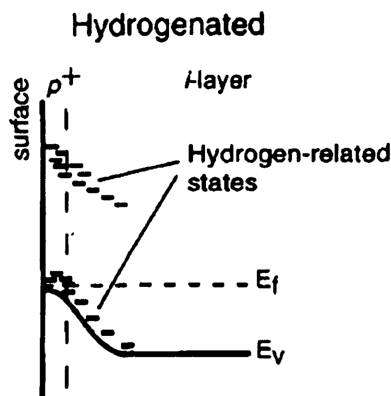

Figure V.2: Energy band diagram of hydrogenated diamond films. E_f and E_v indicate the energy of the Fermi level and the valence band top, respectively. Due

to the high density space charge the valence band of the surface region moves upwards. (Reproduced from Ref. [11])

Ri *et al.* [12] have studied the formation mechanisms of the *p*-type surface conductive layer on diamonds films deposited by hot-filament CVD. The *p*-type conduction of hydrogenated diamond was examined with and without contamination by exposure to air. The resistance near the surface region of diamond immediately after deposition was found to be high (10^{10} Ω), but decreased by four orders of magnitude within ten minutes after removing the deposited film from the CVD chamber. The decrease of resistance was attributed to air exposure which was thought to contribute to the formation of the *p*-type conductive layer. The change in resistance was monitored when the sample was under vacuum and when it was immersed in any of the main components of air (nitrogen N_2, oxygen O_2, carbon dioxide CO_2 and hydrogen H_2) or in dry air, but no effect on the conductivity was observed in any case. In contrast, a significant decrease of resistivity (four orders of magnitude) was noted when the surrounding atmosphere contained hydrochloric acid (HCl), sulfuric acid (H_2SO_4) and nitric acid (HNO_3). Also, introducing atmospheres containing ammonia (NH_3) or sodium hydroxide (NaOH) restored the high resistivity state of the sample, presumably through neutralisation of the acid by alkaline substances. Since typical substances contained in normal air are hydrochloric acid (HCl) and sodium chloride (NaCl) a model was proposed in which the acid dissolves in water vapor to give oxonium ions (H_3O^+) so that they can accept an electron from a hydrogen atom at the diamond surface. Hydrogen atoms on the surface of the diamond film are then positively charged as a valence electron contributing to the valence bond is attracted by the positively charged H_3O^+ ion. The lack of valence electrons in the bond corresponds to the presence of holes. Once all the hydrogen atoms of the surface region have contributed to the creation of holes, an accumulation layer of holes is formed beneath the surface of the diamond. Finally, the negatively charged Cl^- ions are absorbed onto the hydrogenated diamond surface to compensate the positive electric charge due to the holes. The proposed model by Ri *et al.* is illustrated in figure V.3.

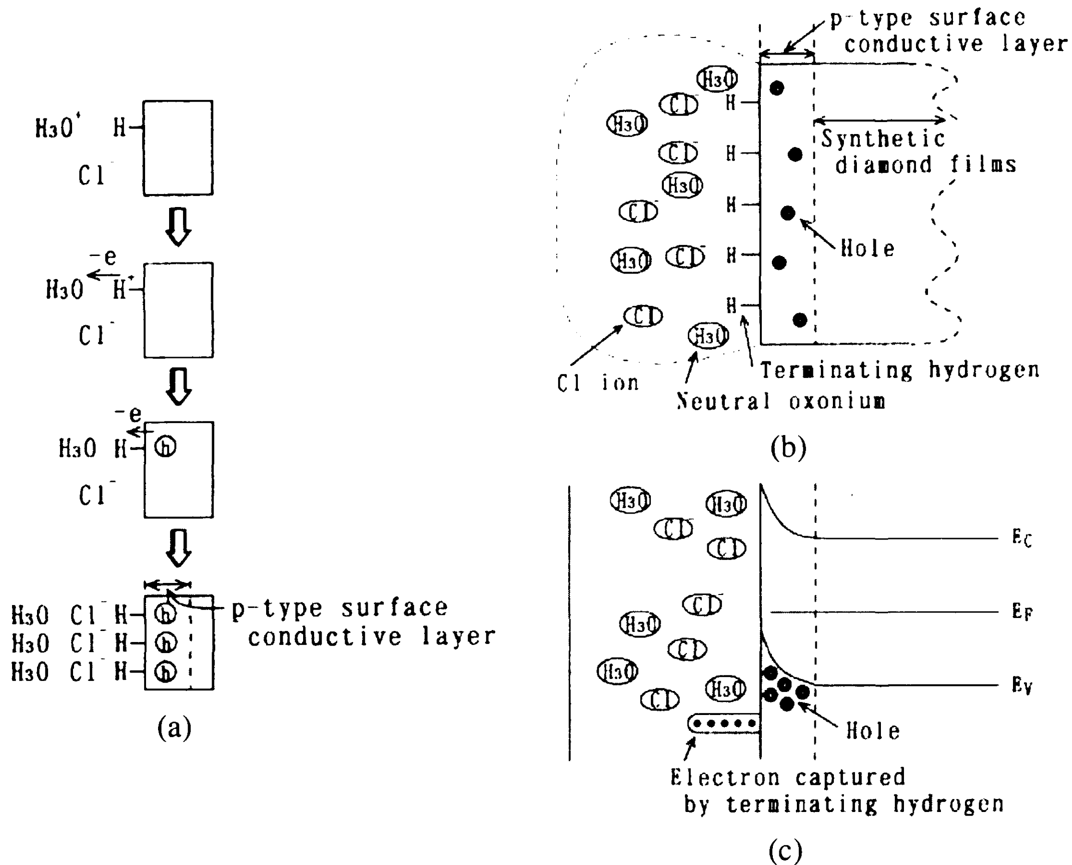

Figure V.3: (a) The process of hole creation in diamond films. (b) Schematic of the surface region after the formation of the *p*-type surface conductive layer. (c) Proposed band model. (Reproduced from Ref. [12].)

More recently Maier *et al.* [13] have given experimental evidence that "the hydrogenation of diamond is a necessary but not sufficient condition for high surface conductivity" to be observed. The conductivity of an undoped homoepitaxial (100) diamond was measured in air and in ultra high vacuum (UHV) by placing two gold tips separated by a distance of 2

mm on the surface. The conductance of the samples was high (10^{-4} A/V) following hydrogenation. After annealing in UHV at 420 ± 20 °C for 15 min the sample returned to its high resistive state as the conductance dropped to 10^{-10} A/V. However the hydrogen on the surface remained intact as demonstrated by the negative electron affinity (NEA) property of the surface as seen in the total photoelectron yield spectrum. In fact, Maier *et al.* pointed out that thermal desorption of chemisorbed hydrogen does not occur below 700°C in UHV. Half of the sample was then masked and the hydrogen was removed from the other half by electron beam induced desorption. This treatment did not have an effect on the conductance as long as the sample remained in UHV (see figure V.4 below). However when it was vented to air, the conductance of the masked (i.e. hydrogenated) area rose by four orders of magnitude. In contrast, the dehydrogenated part of the sample (i.e. unmasked area) remained in its low conductance state with no change being observed.

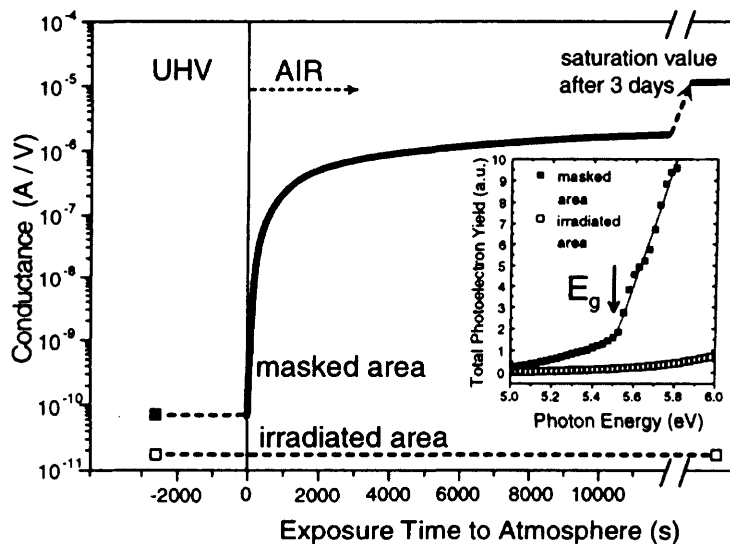

Figure V.4: Surface conductance of the hydrogenated (masked) and the hydrogen-free (irradiated) part of a homoepitaxial diamond (100) layer in UHV and during exposure to air. The inset shows the total photoelectron yield spectra of the two halves after exposure to air. (Reproduced from Maier *et al.* [13])

Maier *et al.* explained their results using a model similar to that previously suggested by Ri *et al.* [12] in which a thin water layer, as it forms naturally on all surfaces exposed to atmosphere, provides an electron system which can act a a surface acceptor for diamond. The electron exchange from the diamond to the water layer in this model is governed by the following redox reaction:

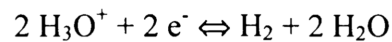

$$2\,H_3O^+ + 2\,e^- \Leftrightarrow H_2 + 2\,H_2O$$

In contrast with the model proposed by Ri *et al.* [12], the positive charge due to the hole accumulation layer is compensated by HCO_3^- anions that are left uncompensated by the reduction of the oxonium ions and not Cl^-.

It has been seen above that hydrogen termination of diamond promotes the formation of high surface conductivity. This observation was confirmed by several groups revealing the *p*-type nature of the conductive surface layer [14,15] which has typical sheet hole densities between 10^{12} and 10^{14} cm^{-2} [15,16] and mobilities between 3 and 70 $cm^2/V\,s$ [16,17]. Several models have been proposed to explain this *p*-type conductivity (see models above in §V.2). Nebel *et al.* [1,18] have performed Hall effect measurements on hydrogen terminated CVD poly- and monocrystalline HPHT diamonds in the temperature range 0.34 - 350 K. The sheet hole densities were found to be weakly temperature dependent above a critical temperatureT_c (20 K $\leq T_c \leq$ 70 K) whilst below T_c carrier freeze out was observed. A transport model [18,19] was introduced in which holes propagate in the valence band where a disorder-induced tail of localised states is present. This model adopts the band bending model of Shirafuji *et al.* [10], where the transport of holes takes place in the vicinity of the diamond surface, and the transfer doping model initially proposed by Ri *et al.* [12] and Maier *et al.* [13]. Here, a hole accumulation layer is generated in the valence band by transfer of valence electron into the surface adsorbate layer which acts as an electron sink. In addition, hydrogen on the surface may not be arranged in a perfectly periodic way and adsorbates which are negatively ionised may generate electronic dipole

disorder. The resulting disorder is said to affect the up-bending of the valence band, generating electronic traps for holes (see figure V.5 left). These traps are distributed in energy (see figure V.5 right). A tail of localised states above a mobility edge causes trapping of hole whereas below the mobility edge the holes are delocalised and can propagate. At temperatures below T_c most of the holes are trapped. To propagate they have to be thermally excited into extended states. The activation energy was found to be shallow. For instance, a sheet hole density activation energy of 23 meV was measured for the {100} homoepitaxial CVD film.

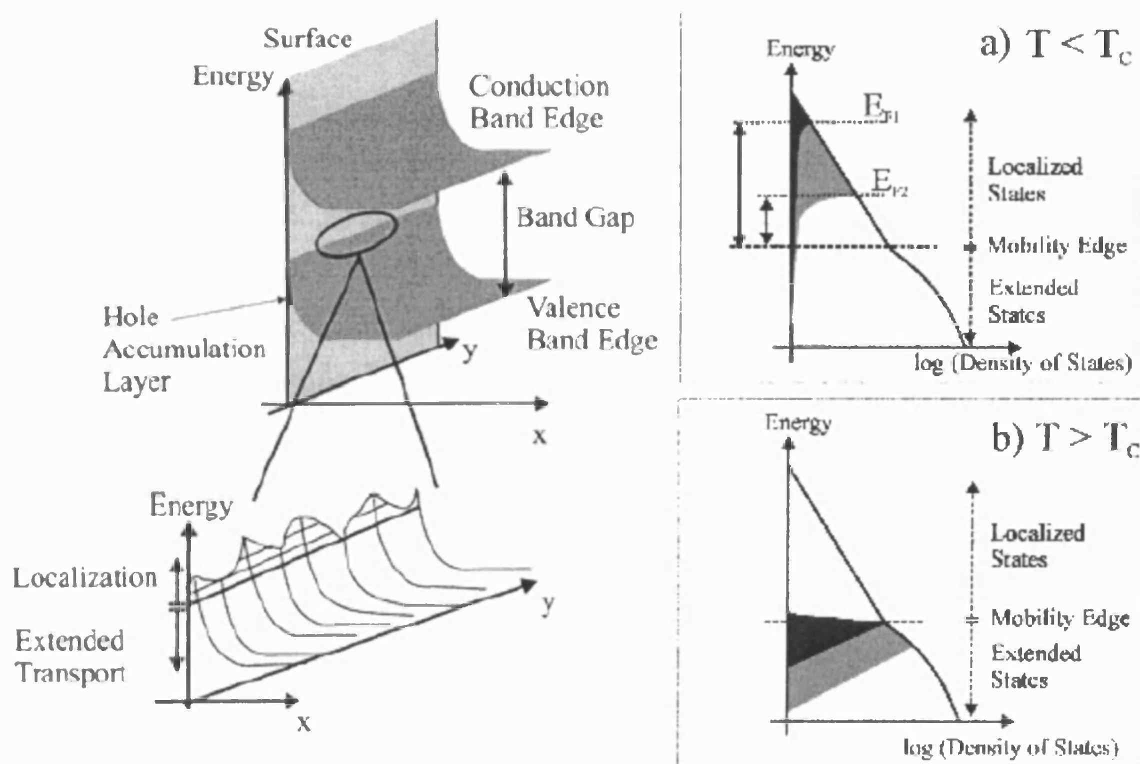

Figure V.5: Left: Schematic description of the density of states at the surface of hydrogenated diamond. The out-diffusion of valence band electrons induces an up-bending, a hole accumulation layer is generated. Due to disorder of ionised adsorbates on and non-perfect hydrpogen termination of the surface, localised

states are generated (see amplified part) which trap holes at low temperature. Right: Exponential tail of localised states at the valence band edge. At temperature below T_c holes are localised in the tail. Only a small fraction can propagate in extended states (a). Above T_c most of the holes are thermally excited into extended states of the valence band (b). The black and grey regions represent two holes densities. E_{F1} and E_{F2} are the activation energies of the trapped holes. (Reproduced from Refs. [18,19])

V.3. EXPERIMENTAL METHODS

Polycrystalline CVD and type IIa natural single crystal diamonds were used throughout this study. Prior to use, the samples were acid dipped following the process described in chapter III to remove contaminants and leave a hydrogen free oxidised surface [20]. The samples were then hydrogenated according to the process also described in section III.2.2. Following this treatment, the surface which was probed using an HP 4145B parameter analyser, was found to be conductive. Typical current values were of the order of the milliAmp (mA) at 10V in air and at room temperature in both samples. Previous studies have shown that the surface was *p*-type in character displaying sheet carrier concentrations within the range $10^{12} - 10^{13}$ cm^{-2}, with carrier mobility values as high as 70 cm^2/Vs [16,21]. For measurement purposes two gold ohmic contacts were placed on the surface of each sample. They were evaporated in a coplanar configuration up to a thickness of 300nm using an Edwards E306 vacuum evaporator. The contacts were separated by a gap of ≈ 1 mm and wire bonded with silver paste. The passivation layer was deposited to cover the gap between the contacts and the I-V measurements were recorded using a Keithley 487 picoammeter/voltage source. The current value was measured every 10°C at 10V in air between room temperature and 350°C.

Different electrically insulating passivation layers were deposited on the diamond surface: Calcium fluoride (CaF_2) capped the polycrystalline material while S1818 positive

photoresist and olive oil covered in turn the IIa diamond sample. CaF_2 in crystal form was evaporated using an Edwards E306 evaporator at a base pressure of 8.10^{-7}mbar to obtain a 3μm thick layer on the diamond surface. The sample was then immersed in an oxygen plasma (100 W RF power, 1 mTorr, 2 min) to leave a hydrogen-free surface around the CaF_2 capping area. Droplets of photoresist or olive oil were deposited on the surface of the IIa diamond to cover the gap between the contacts.

V.4. RESULTS

I-V measurements showed that the samples were all conductive after hydrogenation. Current levels at room temperature before the deposition of the passivating layer of 1.75 mA and 0.86 mA were recorded at 10V in the IIa sample and in the polycrystalline material, respectively. However these values were altered after the deposition of the passivating layers. CaF_2 lead to a total loss of conductivity. The region capped by the calcium fluoride was too resistive for the current to be measured by the Keithley 487 picoammeter. The IIa diamond sample coated with either photoresist or olive oil showed completely opposite results. The surface conductivity was preserved although it decreased slightly after the photoresist or the olive oil had been laid on the surface. The behaviour of the surface conductivity was investigated upon heating both with and without a passivating layer. Figure V.6 shows current measurements for the hydrogenated IIa diamond sample without a resist overlayer, plotted as a function of temperature. Figure V.7 shows similar measurements for the sample having the resist overlayer. In both cases, the sample was heated at 350°C and cooled down twice to room temperature without holding the temperature at 350°C.

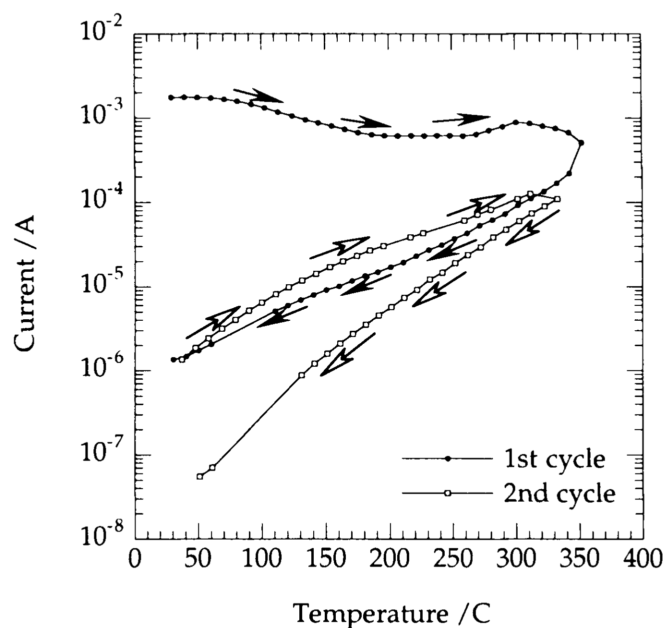

Figure V.6: Current measurements at 10V between room temperature and 350°C on the hydrogenated IIa diamond without S1818 photoresist for two successive heating and down cooling cycles. The temperature was not held at 350°C before the sample was cooled down.

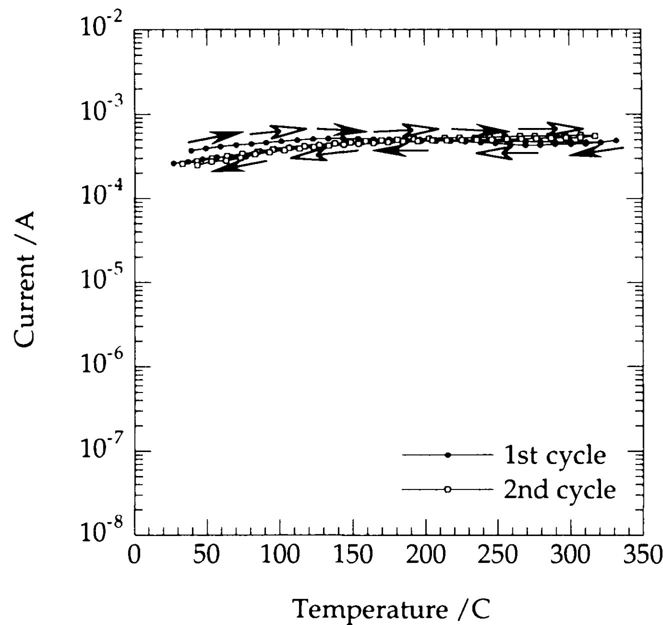

Figure V.7: Current measurements at 10V between room temperature and 350°C on the hydrogenated IIa diamond with S1818 photoresist capping the surface for two successive heating and cooling down cycles. The temperature was not held at 350°C before the sample was cooled down.

At room temperature it can be seen that the current reduces by almost one order of magnitude from 1.7×10^{-3} A to 2.5×10^{-4} A after the resist has been laid on the surface. However, heating the sample and cooling it down does not affect the conductivity as it stays almost constant over the temperature range explored here (20-350°C). On the other hand, the conductivity of the hydrogenated sample without resist varies by nearly 5 orders of magnitude from 1.7×10^{-3} A to 50×10^{-9} A when it is heated and cooled twice. This value indicates that the sample has almost returned to its previous and original high resistive state.

Figure V.8 shows similar data but the temperature was held for 30 minutes at 350°C before the sample was cooled down to room temperature. The conductivity at the high temperature

point is observed to decrease with time and to drop by nearly a factor of three. Further, the current does not return to its original value upon cooling, but instead drops by two orders of magnitude down to a final value of ~4 μA. At this point, inspection of the sample revealed that the photoresist had carbonised.

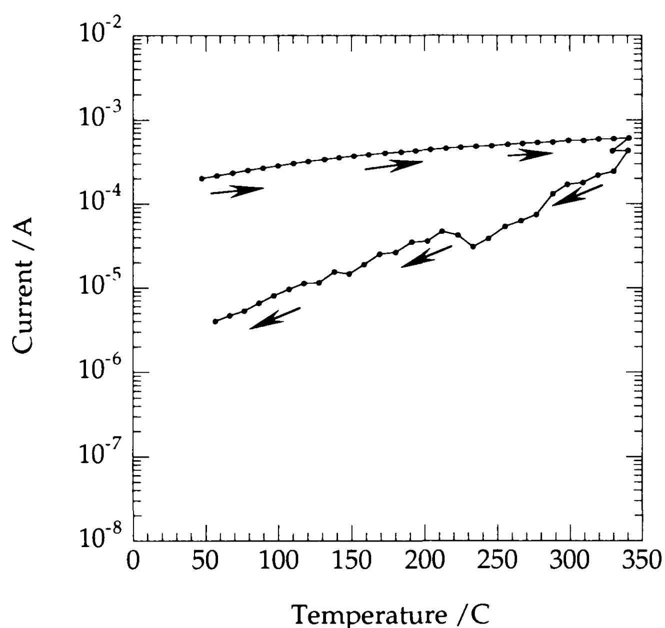

Figure V.8: Current measurements at 10V between room temperature and 350°C on the hydrogenated IIa diamond with S1818 photoresist capping the surface. The temperature was held at 350°C for 30 minutes before the sample was cooled down.

Similar experiments were performed on the IIa diamond sample covered with olive oil, with the results being shown in figures V.9 and V.10.

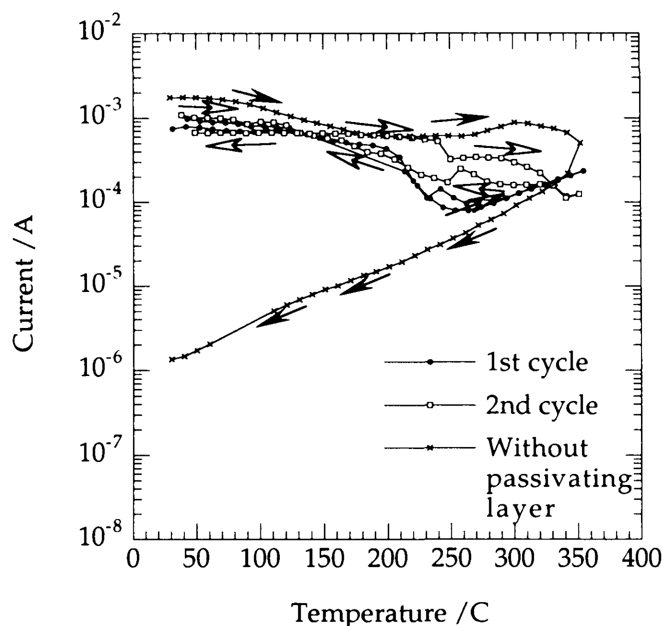

Figure V.9: Current measurements at 10V between room temperature and 350°C on the hydrogenated IIa diamond with olive oil capping the surface for two successive heating and down cooling cycles. The temperature was not held at 350°C before the sample was cooled down.

The olive oil reduces the conductivity level in a manner similar to that of the photoresist after its deposition on the surface. The current intensity drops from 1.7×10^{-3} A to about 10^{-3} A, which is less than with the photoresist (see figure V.9). The current level still returns to its original value upon heating and cooling the sample, but with the difference that it does not keep the same value over the whole temperature range. Current fluctuations appears at 200°C and above leading to a reduction of the current level by nearly one order of magnitude when the tempearture reaches 350°C. However, when the sample is held for half an hour at 350°C, it behaves like it did when it was capped with phototresist and the current level drops by two orders of magnitude from 6×10^{-4} A to about 4×10^{-6} A (see figure V.10).

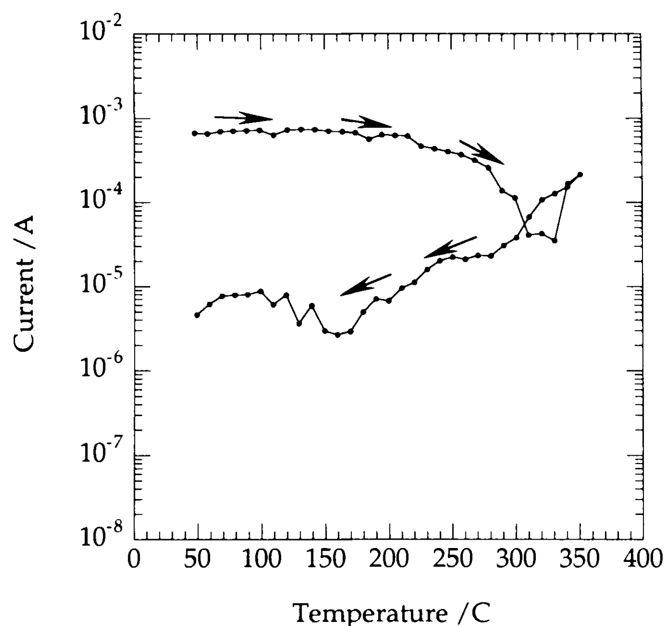

Figure V.10: Current measurements at 10V between room temperature and 350°C on the hydrogenated IIa diamond with olive oil capping the surface for two successive heating and cooling down cycles. The temperature was held at 350°C before the sample was cooled down.

V.5. DISCUSSION

In this study, the aim was to form electrically insulating layers on hydrogenated diamond displaying *p*-type surface conductivity. The objective was to passivate the surface against any loss of adsorbates or against the formation of an additional adsorbate layer that may lead to a change of the observed level of surface conductivity.

For this role thermally deposited calcium fluoride (CaF_2), has not proved successful. Although CaF_2 is an insulator itself, its presence on the hydrogenated surface led to a loss of conductivity. This observation is in contrast with the work reported on MISFET

transistors where impressive device characteristics have been achieved using the same insulating layer for the gate on hydrogen terminated diamond homolayers [22,23]. That our observations relate to the conductivity underneath the layer is important, as adsorbates on the bare diamond surface adjacent to the CaF_2 gate of the MISFET could explain its successful operation. In the present case, the hydrogen termination on the surrounding diamond was intentionally removed with an oxygen plasma to prevent this from occuring. The loss of conductivity seen here could have been predicted however and can be explained. Lanstrass *et al.* have reported that hydrogenation of diamond surfaces led to high conductive surfaces [6] but according to Maier *et al.* this is not a sufficient condition on its own for surface conductivity to be observed [13]. An adsorbate layer is also required. The loss of conductivity is probably due to the requirements of the CaF_2 depostion process. Thermal evaporation of this material requires a good base pressure. Typical pressures used are below 10^{-6} mbar. At these low pressures most of the adsorbates would be removed from the evaporator's chamber and the diamond surface. Therefore, at least one conditions stated by Maier *et al.* in [13] would not be satisfied leading to the loss of surface conductivity.

Photoresist is another electrically insulating material that has been tried to passivate hydrogen terminated diamond surfaces. It is an organic material commonly used in photolithography and it does not require any elaborate deposition process such as thermal evaporation to coat the diamond surface. A drop of liquid is normally sufficient. The results that were obtained constrast with those obtained with calcium fluoride as the photoresist material did not lead to the destruction of the surface conductive layer, although a slight decrease in conductivity was observed. It is believed that this is due to the fact that the adsorbates are capped altogether with the hydrogen atoms when the photoresist is layed on the diamond surface.

Surfaces with resist layers did not show any conductivity change of bare hydrogenated surfaces. This is a promising result if device fabrication should arise from this technology as device stability should be enhanced by the presence of such layers. Moreover the thermal loss of surface conductivity, normally seen around 300°C when a bare hydrogenated

surface is heated in air, does not occur when resist coating is used (see figure V.7). However if the resist coated samples are held at temperatures above 300°C for a long period of time, the photoresist begins to degrade allowing the adsorbates to desorb from the diamond surface. Loss of conductivity is then inevitable in air. The themal properties of the coating layer need to be more rugged and not to degrade at these elevated temperatures for this technology to have a future.

Very similar results have been achieved when olive oil has been used as coating layer instead of photoresist but it is thermally degraded when heated at temperatures greater than 200°C in air. The only advantage of olive oil over photoresists is that it is more stable under intense UV illumination since it does not change its structure.

V.6. CONCLUDING REMARKS

The use of hydrogen terminated diamond surfaces is currently one of the most interesting ways to produce electronic device structures. The method is simple and easy. It does not require doping the material for the surface to become conductive. Hydrogenation alone is sufficient to achieve this goal. However this approach suffers from instabilities. Atmospheric effects make these layers more or less conductive and reproducibility between devices on different sample surfaces is not guaranteed. This study has therefore sought to find a way to counter these fluctuations by capping the conductive hydrogenated surface with insulating layers. These layers act to maintain constant surface conditions underneath them so that the device is passivated against environmental changes.

Calcium fluoride, which was deposited by thermal evaporation to form a highly insulating layer on diamond, has not proved to be a suitable candidate for this purpose, as no conductivity persisted under the CaF_2 layer following deposition. On the other hand, the organic layers used in this experiment achieved better results as both photoresist and olive oil, whilst being insulating themselves, preserved the conductivity and passivated the

conductive layer from any atmospheric influence. However both forms of coating suffered from thermal degradation when heated in air to temperatures above 200°C causing the conductivity of the layer beneath to be eventually lost. This suggests that more temperature resilient organic coatings should be found and used if reliable devices are to emerge from hydrogenated diamond technology.

V.7. REFERENCES

[1] C. E. Nebel, F. Ertl, C. Sauerer, M. Stutzmann, C. F. O. Graeff, P. Bergonzo, O. A. Williams, and R. B. Jackman, Diamond Relat. Mater. **11**, 351 (2002).

[2] H. J. Looi, M. D. Whitfield, J. S. Foord, and R. B. Jackman, Thin Solid Films **344**, 623 (1999).

[3] M. Aoki and H. Kawarada, Jpn. J. Appl. Phys. **33**, L708 (1994).

[4] H. Umezawa, T. Arima, N. Fujihara, H. Taniuchi, H. Ishizaka, M. Tachiki, C. Wild, P. Koidl, and H. Kawarada, Jpn. J. Appl. Phys. Part 1 - Regul. Pap. Short Notes Rev. Pap. **41**, 2611 (2002).

[5] H. Umezawa, H. Taniuchi, T. Arima, M. Tachiki, and H. Kawarada, Diamond Relat. Mater. **10**, 1743 (2001).

[6] M. I. Landstrass and K. V. Ravi, Appl. Phys. Lett. **55**, 975 (1989).

[7] M. I. Landstrass and K. V. Ravi, Appl. Phys. Lett. **55**, 1391 (1989).

[8] S. Albin and L. Watkins, Appl. Phys. Lett. **56**, 1454 (1990).

[9] Y. Muto, T. Sugino, K. Kobashi, and J. Shirafugi, Jpn. J. Appl. Phys. **31**, L4 (1992).

[10] J. Shirafuji and T. Sugino, Diamond Relat. Mater. **5**, 706 (1996).

[11] K. Hayashi, S. Yamanaka, H. Watanabe, T. Sekiguchi, H. Okushi, and K. Kajimura, J. Appl. Phys. **81**, 744 (1997).

[12] S. G. Ri, T. Mizumasa, Y. Akiba, Y. Hirose, T. Kurosu, and M. Iida, Jpn. J. Appl. Phys. **34**, 5550 (1995).

[13] F. Maier, M. Riedel, B. Mantel, J. Ristein, and L. Ley, Phys. Rev. Lett. **85**, 3472 (2000).

[14] T. Maki, S. Shikama, M. Komori, Y. Sakaguchi, K. Sakuta, and T. Kobayashi, Jpn. J. Appl. Phys. **31**, L1446 (1992).

[15] K. Hayashi, S. Yamanaka, H. Okushi, and K. Kajimura, Appl. Phys. Lett. **68**, 376 (1996).

[16] H. J. Looi, R. B. Jackman, and J. S. Foord, Appl. Phys. Lett. **72**, 353 (1998).

[17] R. S. Gi, K. Tashiro, S. Tanaka, T. Fujisawa, H. Kimura, T. Kurosu, and M. Iida, Jpn. J. Appl. Phys. **38**, 3492 (1999).

[18] C. E. Nebel, C. Sauerer, F. Ertl, M. Stutzmann, C. F. O. Graeff, P. Bergonzo, O. A. Williams, and R. B. Jackman, Appl. Phys. Lett. **79**, 4541 (2001).

[19] C. Sauerer, F. Ertl, C. E. Nebel, M. Stutzmann, P. Bergonzo, O. A. Williams, and R. B. Jackman, Phys. Status Solidi A-Appl. Res. **186**, 241 (2001).

[20] Y. Mori, H. Kawarada, and A. Hiraki, Appl. Phys. Lett. **58**, 940 (1991).

[21] H. J. Looi, L. Y. S. Pang, A. B. Molloy, F. Jones, J. S. Foord, and R. B. Jackman, Diamond Relat. Mater. **7**, 550 (1998).

[22] H. Umezawa, H. Taniuchi, T. Arima, M. Tachiki, K. Tsugawa, S. Yamanaka, D. Takeuchi, H. Okushi, and H. Kawarada, Jpn. J. Appl. Phys. Part 2 - Lett. **39**, L908 (2000).

[23] Y. Yun, T. Maki, H. Tanaka, Y. Shirakawa, and T. Kobayashi, Jpn. J. Appl. Phys. Part 2 - Lett. **37**, L1293 (1998).

CHAPTER VI
ULTRANANOCRYSTALLINE DIAMOND: HALL EFFECT MEASUREMENTS

VI.1. Introduction
VI.2. Experimental methods
VI.3. Results
VI.4. Discussion
VI.6. Concluding remarks
VI.7. References

VI.1. INTRODUCTION

Diamond has a number of extreme properties, such as its wide bandgap and high breakdown field strength, which make it ideal for high performance electronics. However, to date, problems with doping diamond *n*-type - in part due to its high atomic density - have hindered its development as a device material. *p*–type doping can be achieved with substitutional incorporation of boron, yielding an activation energy of 0.37 eV, and hence fewer than 1% of the holes are activated at room temperature [1]. Hydrogen-induced surface conductivity can also be utilised to generate holes with an extremely low activation energy [2,3], and high performance devices have been demonstrated using this type of layer [4,5]. *n*–type doping has been much more difficult, with success in substitutional phosphorus doping achieved by relatively few laboratories [6]; an activation energy of 0.6 eV also makes phosphorus an unsuitable dopant for many applications. However, *pn* junctions have been demonstrated utilising the boron-phosphorus interface [7]. A shallow donor species is still sought for diamond.

Ultrananocrystalline diamond (UNCD) is a unique form of diamond grown from an Ar/CH_4 gas phase plasma [8], where the conductivity of the material is strongly influenced by the addition of nitrogen into the source gases [9]. The material becomes conductive with an apparently low thermal activation energy. This is in stark contrast to the case in conventional single-crystal diamond, where the activation energy of substitutional nitrogen is 1.7 eV [10]. Here, Hall effect measurements are presented, which characterise the nitrogenated UNCD conductivity as unequivocally *n*-type.

VI.2. EXPERIMENTAL METHODS

Ultrananocrystalline diamond films were produced at Argonne National Laboratories (ANL) by microwave plasma enhanced chemical vapour deposition (MWPECVD) with various concentrations of nitrogen added to the gas phase, on highly insulating ($>10^9\Omega$) commercially available type Ib HPHT {100} diamond substrates with dimensions of about 2×2×1 mm. The films were grown using a $CH_4(1\%)/Ar/N_2$ gas mixture at a total gas pressure of 100 Torr and 800W microwave power. As nitrogen was added into the gas mixture, the relative partial pressure of Ar was reduced, so that when X% of N_2 was added, the exact composition was 1% CH_4, (99-X)% Ar and X% N_2.

Au contacts were thermally evaporated in the van der Pauw configuration at a base pressure lower than 2 x 10^{-7}mbar. Previous work has shown that Au makes an ohmic contact to UNCD [11], and the ohmic nature of the contacts used here was again confirmed by I/V measurements. The samples were then mounted into a cryostat and wire bonded with silver paint onto the gold contacts. Hall and resistivity measurements were performed in a Lakeshore 7504 Hall Measurement System with an Advanced Research Systems helium atmosphere based cryostat. The magnetic field was swept between ± 1 T under a constant excitation current, the magnitude depending on the sample resistivity. Field sweeps were run at each temperature point throughout the 40-350 K temperature range.

VI.3. RESULTS

Figure VI.1 shows two examples of Hall effect sweeps at a given temperature. Figure VI.1(a) shows the case for a standard *p*-type, boron doped polycrystalline diamond control sample. It can be seen that the hall signal is periodic and 180° out of phase with the applied magnetic field; note that the actual Hall voltage is half the magnitude of the oscillation. Figure VI.1(b) shows the case for a nitrogen doped UNCD sample. It shows a similar effect, but with a voltage that is in phase with the magnetic field; this material is therefore *n*–type due to the opposite direction of the force exerted by the magnetic field. The oscillation amplitude differences between figures 1(a) and 1(b) are due to the differences in carrier concentrations and excitation currents in each sample.

(a)

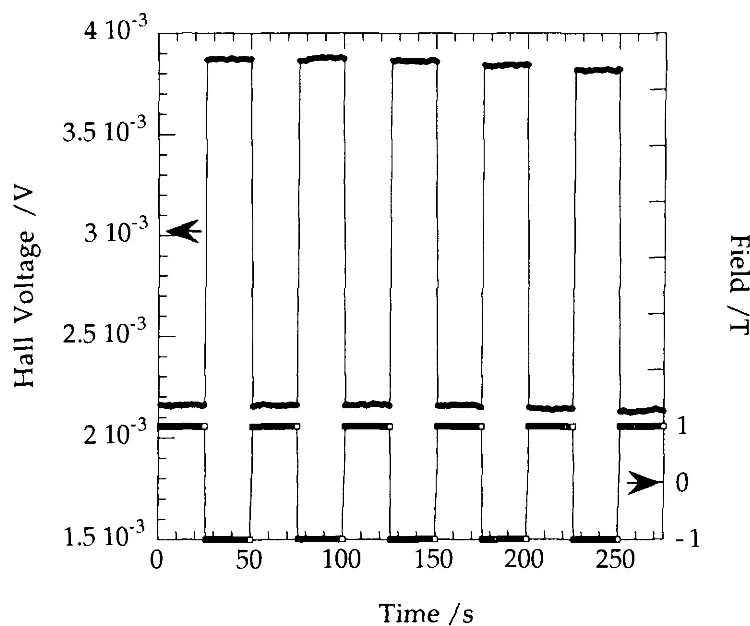

(b)

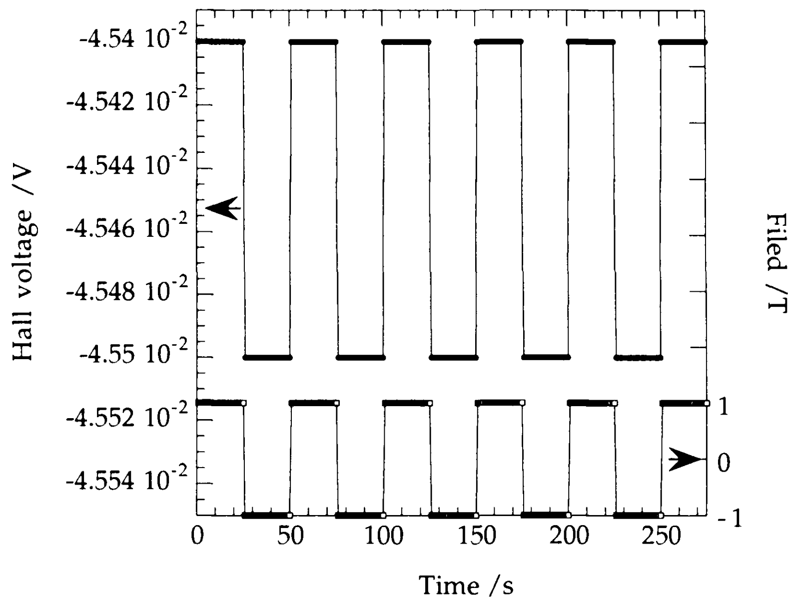

Figure VI.1: a) Hall effect measurements for boron doped microcrystalline diamond, where the Hall voltage is plotted as a function of time as the magnetic field is switched in polarity and b) similar measurements for UNCD grown with nitrogen added to the gas mixture.

The resistivity and carrier concentrations of nitrogen-incorporated UNCD can be tuned by the amount of nitrogen added to the growth plasma. The temperature-dependent sheet-resistivity values of the films grown with 5-20% N_2 in the gas phase are shown in the Arrhenius plot in figure VI.2 over the range 15-300K. It was found that the higher plasma nitrogen content films exhibited both lower resistivities and lower temperature variations of the resistivity. At room temperature (RT) the 5%, 10% and 20% N_2 samples have respectively sheet resistivities of ~2.5×10^4 Ω/sq, ~9×10^2 Ω/sq and~20 Ω/sq. These are the lowest values of sheet resistivity reported for *n*-type diamond [6]. Also, it can be seen that with increasing nitrogen content in the gas mixture, the sheet resistivity of the film becomes less temperature dependent. The 10% N_2 and 20% N_2 samples with values varying

respectively from 878 Ω/sq at RT to 2685 Ω/sq at 50K and from 22 Ω/sq at RT to 38 Ω/sq at 15K, are almost temperature insensitive compared to the 5% sample, which shows sheet resisitivity variations over 3 orders of magnitude from 2.485×10^4 Ω/sq at RT to 4.5×10^7 Ω/sq at 50K. This shows that the former samples display an extremely low thermal activation energy. Further, these curves are clearly not straight lines in the Arrhenius plot, which is indicative of multiple, thermally activated conduction mechanisms with different activation energies. At temperatures between 150K and 300K, the resistivities for the 5%, 10% and 20% N_2 sample are activated respectively with an energy E_{a1} of 81 meV, 11 meV and 3 meV, whereas there are activated respectively with an energy E_{a2} of 27 meV, 4 meV and 1 meV over the temperature range 50-130K.

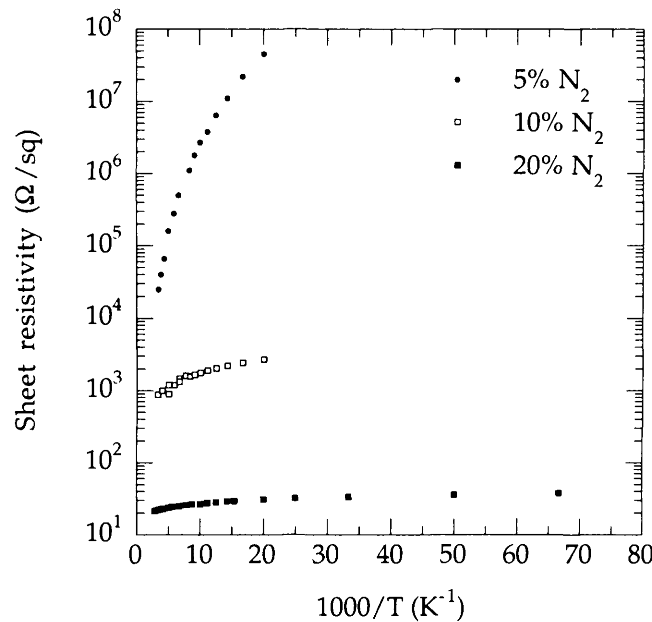

Figure VI.2: Arrhenius plot of sheet resistivity obtained in the temperature range 15-300K for a series of films synthesised using different nitrogen concentrations in the gas phase.

The differences in carrier concentrations for UNCD samples grown with 5%, 10% and 20% nitrogen in the growth plasma are plotted in figure VI.3. It can be seen that the sheet carrier concentrations of these samples reduce with decreasing temperature, although the decrease is less pronounced as nitrogen concentration in the gas mixture is increased. At room temperature the 20% N_2 sample has a sheet carrier concentration of 1.8×10^{17} cm^{-2} and decreases to 1.3×10^{17} cm^{-2} at 15K. The 10% N_2 sample's sheet carrier concentration varies from 4.8×10^{15} cm^{-2} at RT to 2.2×10^{15} cm^{-2} at 50K, a more significant variation but still slight. Finally, the 5% N_2 sample shows larger variations with values ranging from $1.4x10^{14}$ cm^{-2} at RT to $9.1x10^{12}$ cm^{-2} at 50K. Samples grown with lower N_2 content in the plasma did not yield strong Hall signals. This is due to the large resistivity and low mobility values of those films. The films were grown to be about 1 μm thick, yielding bulk carrier concentrations of 10^{17} – 1.8×10^{21} cm^{-3}, which are extremely high for diamond at room temperature. The *n*-type nature of the films was also confirmed by the positive electromotive force generated at the hot probe with respect to the cold probe during Seebeck measurements [12], and thus this material does not exhibit a sign anomaly despite the possibly disordered nature of its grain boundaries [13]. The sign anomaly is more often found in amorphous materials with mobility values below 10^{-1} cm^2 V^{-1} s^{-1}, such as a-Si, and the correct signal is usually observed in microcrystalline Si where the grain size can be as small as 3-5 nm, i.e. comparable with the material characterized here [13].

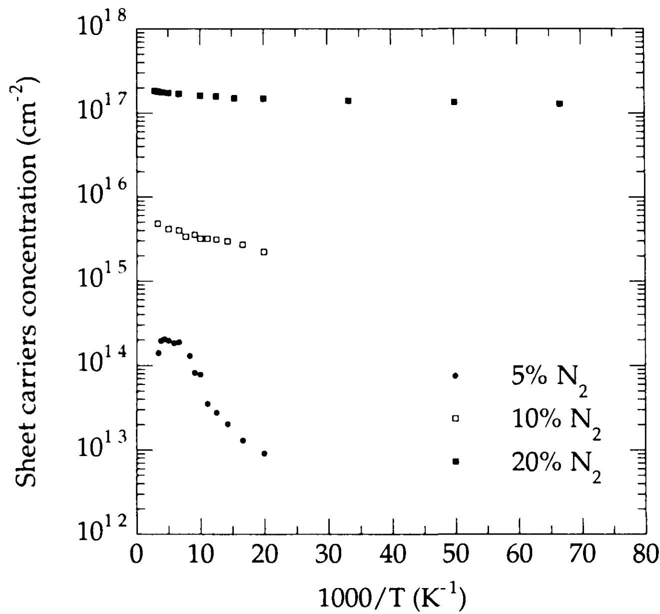

Figure VI.3: Sheet carrier concentrations, determined from Hall effect measurements in UNCD grown with nitrogen as a function of temperature.

The variations in mobility against temperature and plasma nitrogen content are shown in figure VI.4. At room temperature, the values for the mobility are around 1.5 $cm^2V^{-1}s^{-1}$ for the 20% N_2 and the 10% N_2 sample, and are again rather insensitive to temperature. The mobility values for the 5% sample, however, extend over two orders of magnitude in the temperature range 50-300K. The 20% N_2 sample varies from 1.565 $cm^2V^{-1}s^{-1}$ at 300K to 1.285 $cm^2V^{-1}s^{-1}$ at 15 K whereas the 10% N_2 sample varies from 1.485 $cm^2V^{-1}s^{-1}$ at 300K to 1.045 $cm^2V^{-1}s^{-1}$ at 50 K. Again the reduction is more significant in the 10% N_2 sample, but the overall variation is slight. On the other hand, a larger variation from 1.788 $cm^2V^{-1}s^{-1}$ at 300K to 1.5×10^{-2} $cm^2V^{-1}s^{-1}$ at 50 K is observed for the 5% N_2 sample. These values of mobility were derived from the sheet carrier concentration and resistivity values.

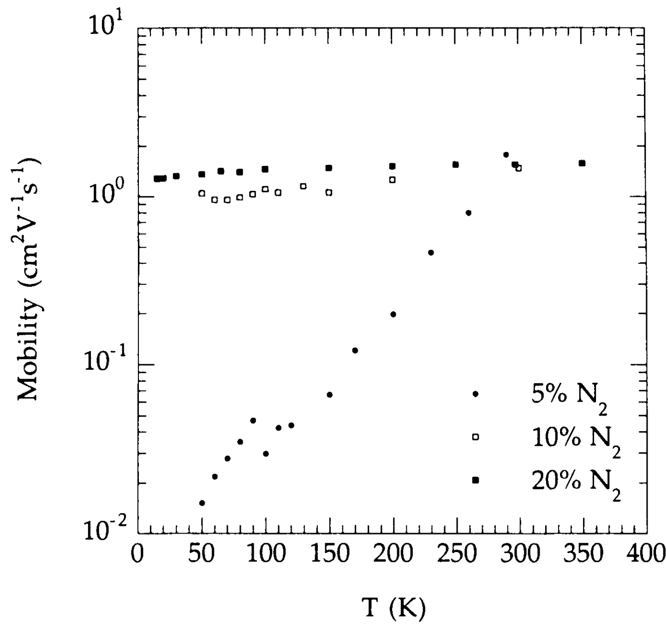

Figure VI.4: Hall mobilities in nitrogen doped UNCD as a function of temperature.

VI.4. DISCUSSION

The enhanced conductivity in UNCD films due to nitrogen is unconventional in the diamond semiconducting field. This is due to several reasons. (i) Nitrogen in single crystal and microcrystalline diamond usually forms a deep donor level with an activation energy of 1.7 eV below the conduction band [14]. A close inspection of the sheet resistivity of UNCD as a function of temperature (see figure VI.2) does not show a single line, which would normally lead to this conclusion. Instead a curvature is observed, suggesting that multiple, thermally activated conduction mechanisms with different activation energies are responsible for the enhanced conductivity. (ii) The sheet resistance associated with these films is much lower than that of diamond containing substantial levels of nitrogen, where values of at least 1×10^9 Ω/sq are normally reported for type Ib diamonds. The reduction in resistivity with nitrogen has however been observed in amorphous carbons such as

"diamond like carbon" (DLC) and "tetrahedrally bonded carbon" (ta-C) in the past, but the resulting mobility values were generally in the 10^{-6} cm^2 V^{-1} s^{-1} range [15,16], i.e. six orders of magnitude lower than nitrogenated UNCD. The conductivity in DLC and ta-C was attributed to hopping mechanisms. A similar conduction mechanism for UNCD was discussed by Zapol *et al.* [17] based on theoretical modelling. Their model predicts that the topographical disorder at the grain boundary region introduces a number of electronic states in the fundamental gap of diamond that can participate in hopping conduction. When nitrogen is incorporated in the grain boundaries, new electronic states associated with carbon and nitrogen are introduced in the bandgap of diamond. In this model, it is important to note that this increase of bandgap states does not require the substitutional electron donor doping configuration of nitrogen, but can occur for other configurations of nitrogen at the grain boundaries. As the concentration of nitrogen in the grain boundaries is increased, the number of states increases in the bandgap, leading to a semi-metallic conduction. This semi-metallic conduction has been observed experimentally here but it is not thought to be due to hopping conduction since the mobility values measured are a few orders of magnitude too high for this mechanism to be responsible. Typically hopping mobility values are lower by at least 4 orders of magnitude with respect to band conduction mobilities [18,19].

A process which involves an impurity band conduction seems to be more probable. According to conventional semiconductor theory, the carrier concentration values should fall as the temperature is decreased. This behaviour is not seen for samples grown with more than 10% of nitrogen in the gas phase, although sample 5% forms an exception and seems to behave in this manner. Hung *et al.* [20,21] were the first to describe this type of behaviour by explaining that the majority of carriers were attached to impurity centres but that they were still able to move about by jumping from one impurity centre to another. Alternatively, if the wave functions of the impurity centres overlapped slightly they would interact to form a narrow band which, when not completely full, would permit movement of carriers through the crystal, although with a very low mobility. For band conduction to take

place, a high concentration of centres is required. This is normally achieved by the presence of a high degree of compensation in the semiconductor material. Mott and Twose [22] showed that the presence of dislocations provide a high enough concentration of defect centres, which have the same compensating effect.

Edwards and Sienko [23] assembled a large set of experimental data and presented an equation to predict the critical impurity concentration at which impurity band conduction occurs:

$$N_{cr}^{1/3}\alpha_H = 0.3 \qquad \text{(VI.1)}$$

where N_{cr} is the critical impurity concentration, α_H is the effective Bohr radius in a hydrogen-like impurity. Using the electron effective mass of diamond, $m^* = 0.2\ m_o$ and the static dielectric constant, $\varepsilon_s = 5.7$ [24], we can obtain the effective Bohr radius as follows:

$$\alpha_H = \frac{4\pi\varepsilon_s\varepsilon_o\hbar^2}{q^2 m^*} = 0.529\frac{\varepsilon_s}{m^*}\ (\text{Å}) \qquad \text{(VI.2)}$$

which yields, $\alpha_H \approx 15$ Å, and by using equation (VI.1), a critical concentration of $N_{cr} = 8\times10^{18}$ cm^{-3} is obtained. This value is lower than the carrier concentration figures measured for the 10% N_2 and the 20% N_2 UNCD samples, therefore suggesting that impurity band conduction takes place in these samples. Additional evidence supporting this assertion is given by the mobility values (around 1-10 cm^{2}V^{-1}s^{-1}), which were found to be consistent for impurity band transport.

For the all the measured samples, no freeze out of carriers was observed. In the case of the 5% N_2 and the 10% N_2 samples, this could be due to the fact that the measurements were not carried out down to low temperatures enough. Nevertheless, based on the considerations mentioned above, the freeze out of carriers is not expected to occur for the 10% sample, even if a fall of carrier concentration values with decreasing temperature is

observed and is predicted by conventional semiconductor theory. In the case of the 5% N_2 sample, the stronger dependence of carrier concentration with temperature together with the low mobility values measured at low temperature indicate that another conduction mechanism rather than impurity conduction is taking part for the lower temperatures.

An examination of the sheet resistivity as a function of temperature provides further insights into the conduction mechanism of UNCD. At about 150K, a bend in all the curves is observed, with activation energy E_{a2} (for 50K-130K) being always smaller then E_{a1} (for 150K-300K). This transition at about 150K corresponds to a change in the conduction mechanism. Between 300K and 150K, the increase of resistivity with decreasing temperature is thought to be partially due to the scattering of the carriers at ionised impurities but mostly due to the electrons depopulating the conduction band. Below 150K, the conduction with activation energy activation energy E_{a1}, induced by electron excitation from the impurity states into the conduction band, is replaced by hopping conduction with a constant activation energy E_{a2} (much lower than E_{a1}), the energy necessary to hop from an occupied to an unoccupied state in the impurity band. As a test for the validity of the hopping hypothesis, the data of figure VI.2 from which the activation energies have been extracted has been re-plotted has ln(sheet resistivity) as a function of $T^{-1/4}$ (see figure VI.5 below). The data, when plotted in this way, follows a linear relationship over the temperature range 50K-150K, which is consistent with a variable range hopping mechanism for the observed conductivity.

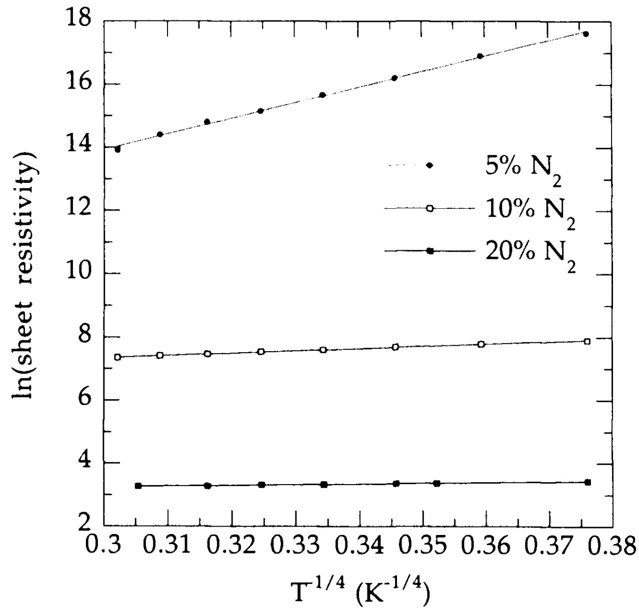

Figure VI.5: data of figure VI.2 re-plotted as ln(sheet resistivity) as a function of $T^{-1/4}$ for temperatures between 50K and 150K.

Besides, the temperature dependence of sheet resistivity for the investigated UNCD samples (figure VI.2) shows a diminution of the activation energy values E_{a2} and E_{a1}, determined for 50K < T < 150K and 150K < T < 300K, with increasing nitrogen in the gas mixture so that the activated conduction is replaced by a semi-metallic type conduction.

For the 10% N_2 and 20% N_2 samples, the mobility does not change (saturation reached) which is characteristic of electron mobility in the impurity band. With increasing impurity concentration the mobility in the impurity band increases at a fixed temperature as is clear from figure VI.4. This increase is due to a widening of the impurity band, which in turn increases the mean free path of the electrons. In the 10% N_2 and 20% N_2 samples the mobilities at high and low temperature have a tendency to equality and this is indicative of an overlap of the impurity and the conduction band.

VI.5. CONCLUDING REMARKS

The transport properties of nitrogenated UNCD films have been investigated using Hall effect measurements. The effect of nitrogen incorporation on the electronic properties of the material is dramatic. The conduction becomes *n*-type and the resistivitiy is found to decrease with increasing nitrogen content in the gas phase. The activation energies vary accordingly and are very low, i.e. only a few meV. This contrasts to the case in single and polycrystalline diamond, where the activation energy of substitutional nitrogen is 1.7 eV, suggesting that nitrogen is not substitutional in UNCD films. Instead, nitrogen introduces shallow donor states, which leads to a curious increase in carrier population at low temperatures, perhaps linked with an impurity band conduction process. The critical impurity concentration for this process to happen has been calculated to be 8×10^{18} cm^{-3}, which is in good agreement with the carrier concentration measurements. Finally, the resistivity data follows a $T^{-1/4}$ law below 150K suggesting that hopping is also contributing to the conduction.

VI.6. REFERENCES

[1] M. W. Geis and J. C. Angus, Scientific American **October**, 64 (1992).

[2] C. E. Nebel, C. Sauerer, F. Ertl, M. Stutzmann, C. F. O. Graeff, P. Bergonzo, O. A. Williams, and R. B. Jackman, Appl. Phys. Lett. **79**, 4541 (2001).

[3] O. A. Williams, M. D. Whitfield, R. B. Jackman, J. S. Foord, J. E. Butler, and C. E. Nebel, Appl. Phys. Lett. **78**, 3460 (2001).

[4] A. Hokazono, H. Kawarada, T. Ishikura, K. Nakamura, and S. Yamashita, Diamond Relat. Mater. **6**, 339 (1997).

[5] A. Aleksov, A. Denisenko, U. Spitzberg, T. Jenkins, W. Ebert, and E. Kohn, Diamond Relat. Mater. **11**, 382 (2002).

[6] S. Koizumi, T. Teraji, and H. Kanda, Diamond Relat. Mater. **9**, 935 (2000).

[7] S. Koizumi, K. Watanabe, F. Hasegawa, and H. Kanda, Science **292**, 1899 (2001).

[8] D. M. Gruen, Annual Review of Materials Science **29**, 211 (1999).

[9] S. Bhattacharyya, O. Auciello, J. Birrell, J. A. Carlisle, L. A. Curtiss, A. N. Goyette, D. M. Gruen, A. R. Krauss, J. Schlueter, A. Sumant, and P. Zapol, Appl. Phys. Lett. **79**, 1441 (2001).

[10] G. Davies, *The Optical Properties of Diamond* (Mercel Dekker, New York, 1977).

[11] J. E. Gerbi, O. Auciello, J. Birrell, D. M. Gruen, B. W. Alphenaar, and J. A. Carlisle, Appl. Phys. Lett. **83**, 2001 (2003).

[12] D. K. Schroder, *Semiconductor Material and Device Characterization*, 2nd ed. (Wiley, New York, 1998).

[13] C. E. Nebel, M. Rother, M. Stutzmann, C. Summonte, and M. Heintze, Philosophical Magazine Letters **74**, 455 (1996).

[14] J. Robertson and C. A. Davis, Diamond Relat. Mater. **4**, 441 (1995).

[15] W. Mycielski, E. Staryga, A. Lipinski, S. Mitura, and A. Sokolowska, Diamond Relat. Mater. **3**, 858 (1994).

[16] L. Klibanov, M. Oksman, A. Seidman, and N. Croitoru, Diamond Relat. Mater. **6**, 1152 (1997).

[17] P. Zapol, M. Sternberg, L. A. Curtiss, T. Frauenheim, and D. M. Gruen, Physical Review B (Condensed Matter and Materials Physics) **65**, 045403 (2002).

[18] H. Fritzsche, Phys. Rev. **99**, 406 (1955).

[19] C. L. Chang, S. P. Shukla, W. Pan, V. Venkataraman, J. C. Sturm, and M. Shayegan, Thin Solid Films **321**, 51 (1998).

[20] C. S. Hung and J. R. Gliessman, Phys. Rev. **79**, 726 (1950).

[21] C. S. Hung and J. R. Gliessman, Phys. Rev. **96**, 1226 (1954).

[22] N. F. Mott and T. D. Twose, Adv. Phys. **10**, 107 (1961).

[23] P. P. Edwards and M. J. Sienko, Phys. Rev. B **17**, 2575 (1978).

[24] S. M. Sze, *Physics of Semiconductors* (John Wileys & Sons, Inc., New York, 1981).

CHAPTER VII
ULTRANANOCRYSTALLINE DIAMOND: IMPEDANCE SPECTROSCOPY

VII.1. Introduction
VII.2. Experimental methods
VII.3. ANL Analysis of UNCD films
VII.4 Results: Impedance spectroscopy measurements
VII.5. Discussion
VII.6. Concluding remarks
VII.7. References

VII.1. INTRODUCTION

The remarkable properties of diamond, i.e. exceptional hardness, thermal conductivity, electrical resistance, chemical inertness, optical transmittance, electrical carrier mobility, and dielectric breakdown strength, etc., combined with the emergence of chemical vapour deposition (CVD) technique for the growth of thin film diamond has led to a widespread interest in the use of this material for electronic applications as it enables large surface area samples to be grown. The focus of most growth studies to date has been in the production of high quality, large grain polycrystalline diamond, with the realisation of large area single crystalline material remaining a key aim of the diamond research community. Early reports on fine grain nanocrystalline diamond received less attention since they did not appear to fit with these aims [1,2]. However, this position has recently changed with the properties of nanocrystalline and ultrananocrystalline films themselves being recognised as potentially useful for many applications including enhanced field emission [3], electrochemical electrodes [4], tribology, cold cathodes, corrosion resistance, and conformal coatings on MEMs devices [5].

For the last few years, Argonne National Laboratory (ANL) has produced ultrananocrystalline diamond (UNCD) films by microwave plasma enhanced chemical vapour deposition [6,7]. This technique involves using C_{60}/Ar or CH_4(1%)/Ar plasmas which are thought to lead to the generation of C_2 molecular precursors, which in turn result in the growth of UNCD films with 2-5 nm grain sizes and 0.3-0.4 nm-wide grain boundaries [8]. Incorporation of impurities into UNCD films, and in particular the incorporation of nitrogen via the addition of N_2 gas to the CVD gas reactants leads to changes in morphology and enhances electronic transport within the film.

Birrel *et al.* [9] have reported that both the grain size and the grain boundary widths increase with the addition of N_2 in this material. In addition, the electrical conductivity of the nitrogen doped UNCD films increases by five orders of magnitude with increasing nitrogen content [10]. Conductivity and Hall measurements made as a function of temperature down to 4.2K indicate that these films have the highest *n*-type conductivity and carrier concentration demonstrated for phase-pure diamond films. It is proposed that grain boundary conduction be responsible for the remarkable transport properties of these films [10]. However, no direct experimental evidence is available to support such a proposal. In this chapter, impedance spectroscopy has been used to gain further insight into the conduction mechanism(s) of this type of material. This technique has previously been used to characterise polycrystalline and nanocrystalline CVD diamond films where the contribution from the grains, grain boundaries and contacts were observed [11-14]. This chapter presents new results on how grain boundary and/or grain interior conduction dominate within UNCD films, using impedance spectroscopy.

VII.2. EXPERIMENTAL METHODS

The UNCD films studied here were produced at Argonne National Laboratory by microwave plasma enhanced chemical vapour deposition onto synthetic Ib {100} HPHT

diamond substrates with dimensions of about 2×2×1 mm. The samples were grown at 800°C using a $CH_4/Ar/N_2$ gas mixture at a total gas pressure of 100 Torr and 800W microwave power. The gas composition was 1% CH_4, 99% Ar for the sample with no nitrogen incorporation. As nitrogen was added into the plasma, the relative partial pressure of Ar was reduced so that a "X% N_2" film was grown with a gas composition of 1% CH_4, (99-X)% Ar and X% N_2. The composition of the gas reactants for the set of samples (I, II, III and IV) used in this chapter are summarised in table VII.1.

Sample	**Reactant gas content**		
	N_2	**CH_4**	**Ar**
(I)	0%	1%	99%
(II)	5%	1%	94%
(III)	10%	1%	89%
(IV)	20%	1%	79%

Table VII.1: Reactant gas composition in the plasma for UNCD samples (I), (II), (III) and (IV).

The changes in morphology and bonding in the grains and grain boundaries of the UNCD films grown with different amount of nitrogen in the gas mixture were investigated at ANL using high-resolution transmission electron microscopy (HRTEM) and electron energy-loss spectroscopy (EELS). HRTEM samples were prepared via mechanical polishing, followed by ion milling at grazing incidence angles. HRTEM was performed using a JEOL 4000EX microscope at 400kV. EELS was performed using a JEOL 2010F scanning transmission electron microscope with a Gatan 666 parallel EELS detector operated at 200 kV, using a nanoprobe of 1nm in diameter to determine the local bonding structure both at the grain boundaries and in the diamond grains themselves. To locate suitable areas for the grain boundary EELS, the samples were first studied using bright field HRTEM so that when a suitable grain boundary was found, the electron probe was placed on the area corresponding

to the grain boundary and the spectrum was taken. HRTEM was chosen to assay the changes in nanoscale morphology in these films because conventional dark-field techniques have some difficulties with grain overlap when measuring grains as small as those of UNCD (2-16nm).

In this study, silver paint was deposited on the UNCD films' surface to form ohmic contacts. The electrical measurements were taken between two symmetric contacts across the sample's surface in a vacuum of 10^{-2} Torr. The effect of current flow through the Ib diamond substrate on the measured resistance was ignored due to the near-perfect insulating properties of this type of diamond. A similar assumption has been used previously by others [15]. Impedance measurements of the film were carried out using an impedance spectroscopy system (Solartron 1260A) in the frequency range 0.1 Hz to 10 MHz, from 25°C up to 350°C. The set up parameters were 0.05V of ac amplitude, one second integration time, and no delay time.

VII.3. ANL ANALYSIS OF UNCD FILMS

HRTEM micrographs taken at ANL for samples similar to (I) to (IV) shown on figure VII.1(a)-VII.1(d) indicate that adding nitrogen to the plasma has a profound impact on the nanostructure of the UNCD film. Electron diffraction patterns are also shown as insets in figure. VII.1. Clearly, for nitrogen concentration in the plasma from 0% to 20%, the UNCD films retain a grain and a grain boundary morphology, with both the grain size and the grain boundary width increasing with nitrogen concentration. The size of the grains gradually increases from about 4 to 16 nm, as the nitrogen content in the plasma is changed from 0% to 20%. The grain-boundary width increases as well, from about 0.5 to 2.2 nm [9].

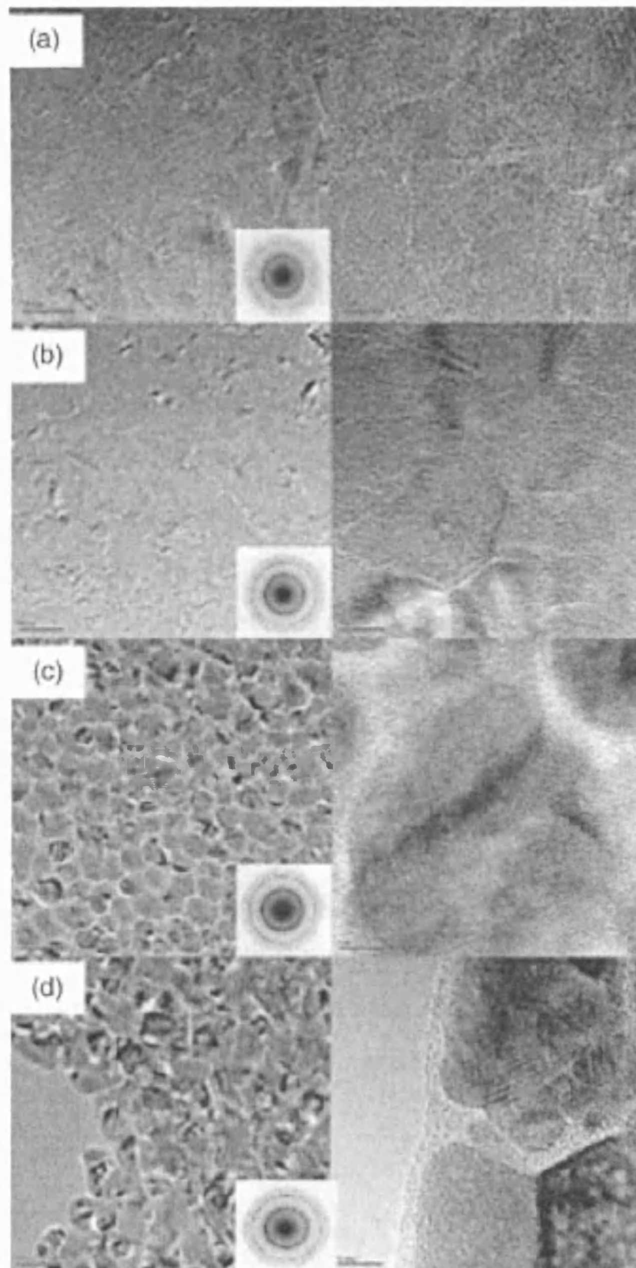

Figure VII.1: Low- and high-resolution TEM micrographs of UNCD sample set: (a) sample (I), (b) sample (II), (c) sample (III) and (d) sample (IV). The low-resolution micrographs are on the left, the high resolution ones are on the right. Figures are scaled so that the low-resolution micrographs are 350 nm × 350 nm and the high-resolution ones are 35 nm × 35 nm. (Reprinted from [9]).

To assess the atomic origins of the sp^2 bonding in these films, small-spot EELS measurements were used to compare the bonding structure in the diamond grains and the grain boundaries of the UNCD films that were grown with an increasing amount of nitrogen in the plasma. Figure VII.2(a) shows a typical EELS spectrum obtained with the electron beam positioned on one UNCD grain. It indicates that it is phase pure diamond, as evidenced by the near-edge electronic structure of the peak. The well-defined absorption edge at 289.5 eV and the presence of the second band-gap feature clearly shows that the diamond grains are sp^3-bonded carbon atoms with a high degree of short-range ordering [16]. This does not change as nitrogen is added to the plasma, showing that there is no change in the electronic structure within the grains. The grain boundary spectra (figure VII.2(b)) show a very slight variation as nitrogen is incorporated into the plasma. Specifically, the π^* peak at 285 eV increases slightly when nitrogen is incorporated into the UNCD film. The σ^* feature that peaks at ~289 eV, which is associated with sp^3 bonding [17], is unchanged. The relative intensities of the sp^2 versus sp^3 peaks in the spectra of figure VII.2(b) indicate that the amount of sp^2 bonding increases only slightly within the grain boundaries when nitrogen is added to the plasma. This indicates that the level of sp^2 bonding within the grain boundaries remains relatively unchanged as nitrogen is incorporated into UNCD. It is therefore concluded that the increase in sp^2 content in the film as a whole is due to a slight increase in grain-boundary area in the film, and not a change in the local bonding structure within the grains or grain boundaries [9].

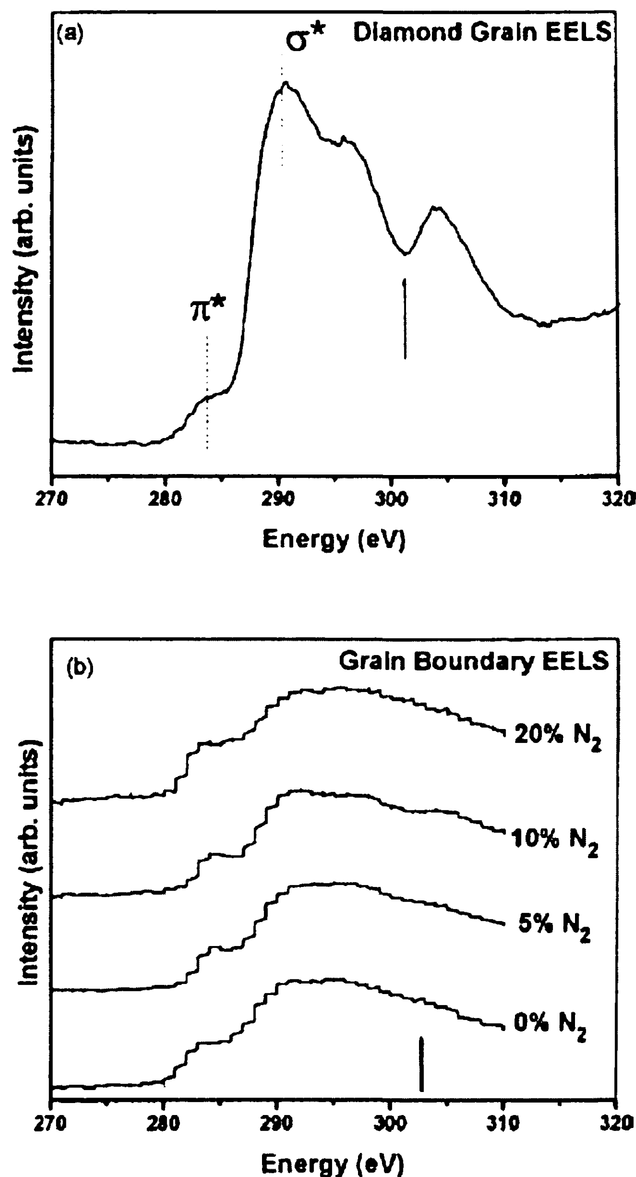

Figure VII.2: EELS spectra using an electron nanoprobe of (a) an individual representative UNCD grain, and (b) a series of nitrogen-doped UNCD thin films with the nanoprobe located on a grain boundary. The energy of the π* (σ*) conduction-band states for sp^2 (sp^3)-bonded carbon are shown by the dashed lines. The arrow marks the energy position of the second band gap in diamond, which is clearly present in the grains and absent in the grain boundaries. (Reprinted from [9]).

VII.4 RESULTS: IMPEDANCE SPECTROSCOPY MEASUREMENTS

The Cole-Cole plots for sample (I) from 25°C to 350°C are shown in figure VII.3, where the semicircle on the right hand side (RHS) appears at lower frequencies and the semicircle on the left hand side (LHS) at high frequencies. Over the temperature range 25°C-150°C, two semicircles are visible, labelled I and II. At 200°C, it is clearly seen that a tail occurs on the right hand side, which becomes a full semicircle at T=300°C and 350°C, denoted as III. Meanwhile the shape of semicircle II changes. It becomes a bit flat at 250°C and 300°C, and appears as tail on the RHS of semicircle I at 350°C.

The resistance and the capacitance values for each semicircle were obtained by fitting each curve or arc based on a single R-C parallel equivalent circuit using Zview, a software package supplied by Solartron Inc. These values are shown in table VII.2. In the case of sample (I), data with subscript *GB* corresponds to semicircle II over the temperature range 25°C-200°C whereas it corresponds to semicircle III for temperatures between 250°C and 350°C. An example of the fitting process is shown in figure VII.3(a) but for clarity of presentation is admitted for the other cases.

Over the whole temperature range, the capacitance C_{GI} of semicircle I lies within the pF range while the capacitance C_{GB} of semicircles II and III lies in the nF range. The subscripts *GI* and *GB* refer to grain interiors and grain boundaries respectively. The origin of this assignment will be explained later in the discussion. With increasing temperatures, the semicircle on the LHS becomes larger with respect to the one on the RHS. This behaviour is normally attributed to a progressive change in the dominating conduction path with increasing temperatures, as evidenced by a change in the relative resistance ratio R_{GI}/R_{GB} between the resistance values R_{GB} and R_{GI}, for the right and left hand side semicircles, respectively, which is increasing from 0.172 at 25°C to 3.39 at 350°C. The order of magnitude of the x-axis also decreases significantly from 10^8 Ω at 25°C to 10^5 Ω at 350°C, indicating that the overall resistance of the sample ($R_{high\,freq} - R_{low\,freq}$) has dropped by three orders of magnitude.

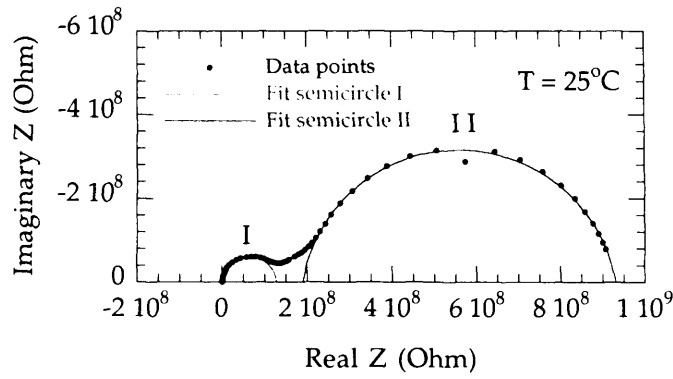

(a) UNCD sample (I) at 25°C

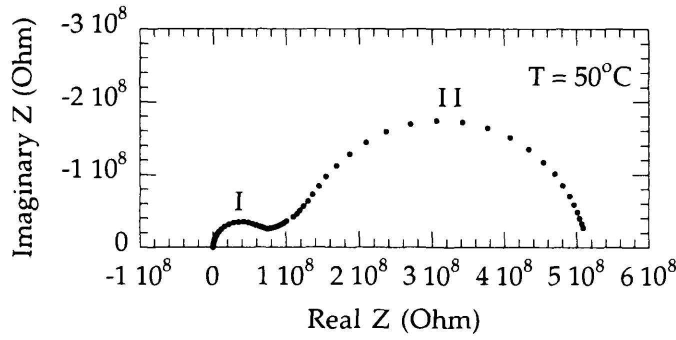

(b) UNCD sample (I) at 50°C

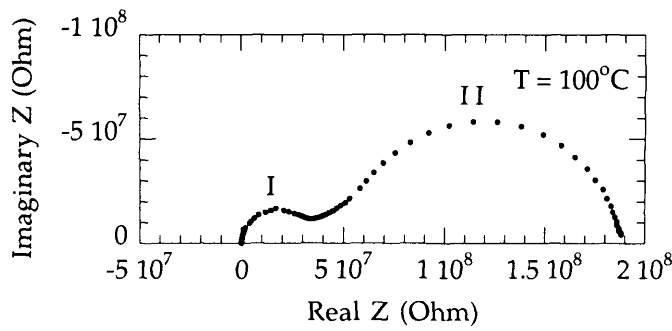

(c) UNCD sample (I) at 100°C

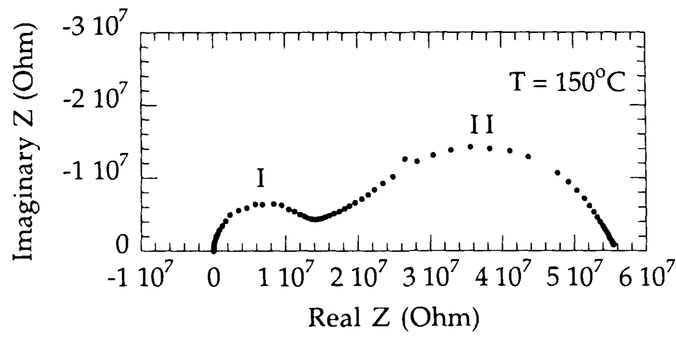

(d) UNCD sample (I) at 150°C

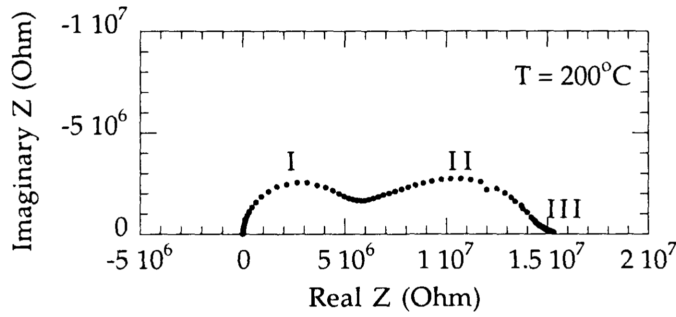

(e) UNCD sample (I) at 200°C

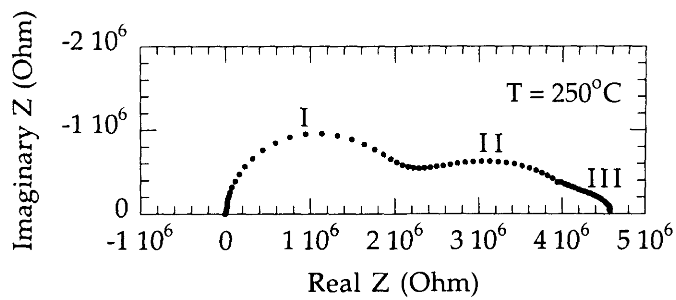

(f) UNCD sample (I) at 250°C

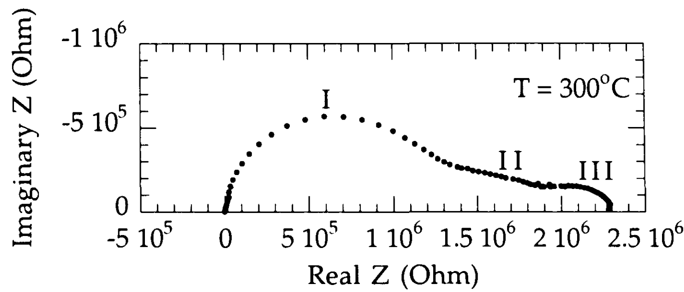

(g) UNCD sample (I) at 300°C

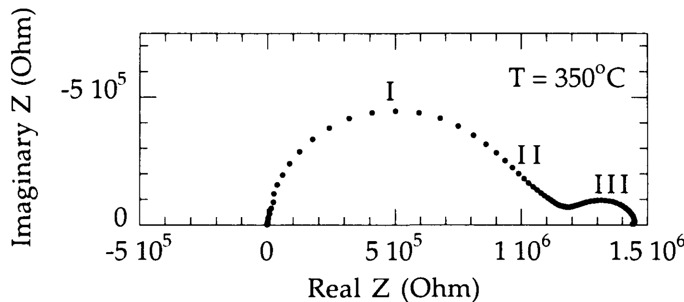

(h) UNCD sample (I) at 350°C

Figure VII.3: Cole-Cole plots of UNCD sample (I) at different temperatures: (a) 25°C, (b) 50°C, (c) 100°C, (d) 150°C, (e) 200°C, (f) 250°C, (g) 300°C and (h) 350°C.

A behaviour similar to that of sample (I) was observed for sample (II). For all given temperatures, the Cole-Cole response is formed by three semicircles, only two of which, namely I on the LHS and III on the RHS, are clearly observed. Semicircle II is hardly visible as it is masked by the intensity of semicircle III, but it can be seen as a tail on the left hand side of semicircle III. At temperatures above 200°C, semicircle I extending to higher frequencies becomes an arc. This transition from a perfect semicircle to an imperfect arc is due to the limitation of the equipment, which can only take measurements for frequencies between 0.1Hz and 10MHz [15]. For convenience and clarity, only impedance

data at the two temperature ends (25°C and 350°C) are shown in figure VII.4. The simulated resistance and the capacitance values are listed for the whole temperature range in table VII.2. Note that values for semicircle II were not obtained, as this semicircle is not properly resolved and could not be fitted. Hence the subscripts *GI* and *GB* refer to semicircles I and III, respectively. At 25°C, semicircle I has a resistance R_{GI} of 61 kΩ and a capacitance C_{GI} of 1.55 pF while semicircle III has a resistance R_{GB} of 314 kΩ and a capacitance C_{GB} of 0.15 nF. The relative resistance ratio R_{GI}/R_{GB} is thus 0.194. As the temperature increases, both R_{GI} and R_{GB} decrease so that the overall resistance of the sample drops by two orders of magnitude, from 430 kΩ at 25°C to 11.3 kΩ at 350°C. At 350°C, the ratio R_{GI}/R_{GB} is 1.219, which is 6 times greater than at 25°C, indicating that there is a transition in the dominating conduction path, as it was the case of sample (I).

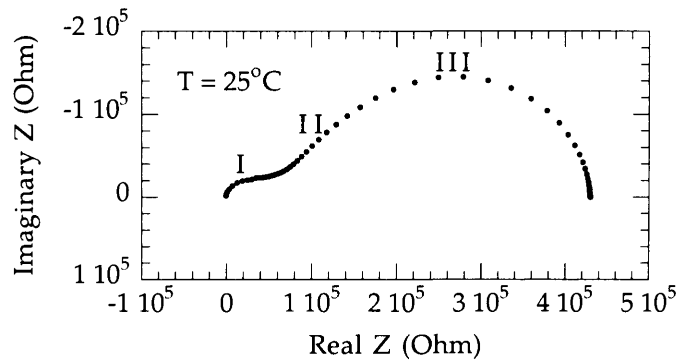

UNCD sample (II) at 25°C

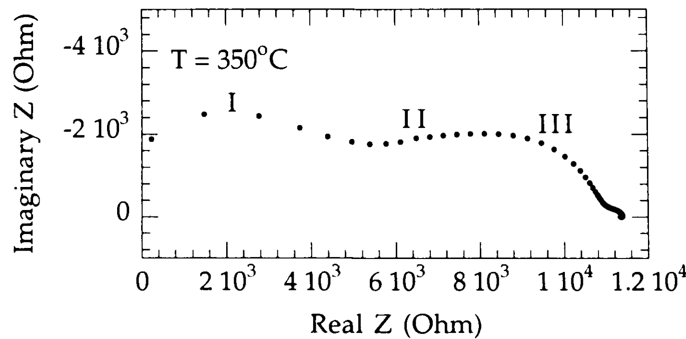

(b) UNCD sample (II) at 350°C

Figure VII.4: Cole-Cole plots of UNCD sample (II) at different temperatures: (a) 25°C and (b) 350°C.

The impedance response of sample (III) shows two semicircles, with a tail being apparent on the left hand side of the semicircle occurring at low frequencies. Here, the semicircle at high frequencies (labeled I) has almost disappeared over the temperature range, indicating that the resistance values R_{GI} are approaching zero. Because the impedance response for sample (III) shows identical characteristics at all temperatures, only the Cole-Cole plots for 25°C and 320°C have been represented in figure VII.5. Semicircle II could not be fitted and hence the resistance and capacitance values associated with this semicircle could not be obtained. However, a fit of the semicircle for the lower frequencies (denoted III on figure VII.5) yielded the resistance values R_{GB} and the capacitance values C_{GB} listed in table VII.2. For this semicircle, R_{GB} varies from 6884 Ω at 25°C to 1919 Ω at 320°C and the capacitance values C_{GB} are all within the nF range. As for samples (I) and (II), the overall resistance of the sample, decreases with increasing temperature from 8.5 kΩ at 25°C to 2.7 kΩ at 320°C.

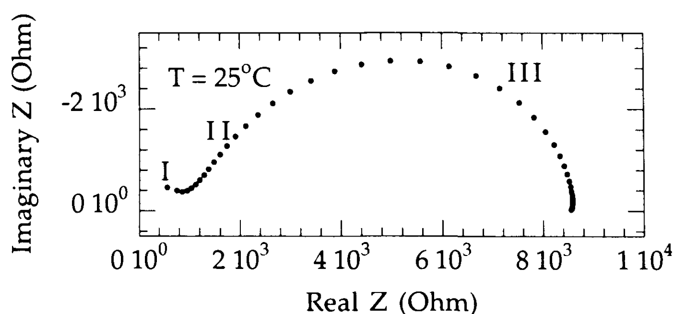

(a) UNCD sample (III) at 25°C

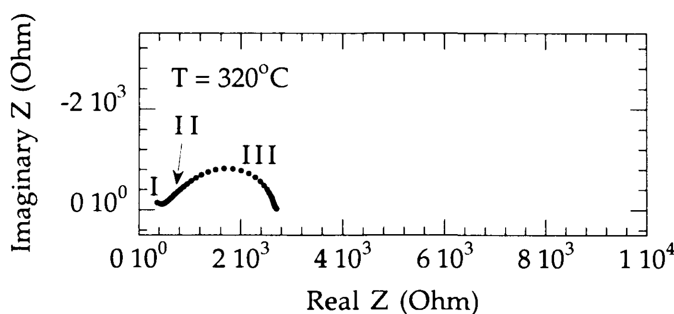

(b) UNCD sample (III) at 320°C

Figure VII.5: Cole-Cole plots of UNCD sample (III) at different temperatures: (a) 25°C and (b) 320°C.

Impedance data for sample (IV) is not available. This is because sample (IV) with 20% nitrogen in the gas reactants behaves like a metallic conductor. The measurement of impedance for a conductive material is beyond the limitation of the equipment.

Sample	T (°C)	R_{GI} (Ω)	C_{GI} (F)	R_{GB} (Ω)	C_{GB} (F)	R_{GI}/R_{GB}
(I)	25	$1.2748\ 10^{8}$	$9.9031\ 10^{-13}$	$7.4074\ 10^{8}$	$2.0141\ 10^{-10}$	0.172
	50	$7.3513\ 10^{7}$	$8.6059\ 10^{-13}$	$4.0004\ 10^{8}$	$2.0784\ 10^{-10}$	0.184
	100	$3.5586\ 10^{7}$	$9.2467\ 10^{-13}$	$1.4043\ 10^{8}$	$1.9305\ 10^{-10}$	0.253
	150	$1.3456\ 10^{7}$	$9.2604\ 10^{-13}$	$3.8379\ 10^{7}$	$2.1135\ 10^{-10}$	0.351
	200	$5.7355\ 10^{6}$	$9.448\ 10^{-13}$	$9.1303\ 10^{6}$	$1.2149\ 10^{-10}$	0.628
	250	$2.1239\ 10^{6}$	$1.0763\ 10^{-12}$	$2.4191\ 10^{6}$	$1.0708\ 10^{-10}$	0.878
	300	$1.3049\ 10^{6}$	$1.0757\ 10^{-12}$	$4.6608\ 10^{5}$	$1.864\ 10^{-8}$	2.800
	350	$9.6857\ 10^{5}$	$9.9803\ 10^{-12}$	$2.8585\ 10^{5}$	$1.7455\ 10^{-8}$	3.388
(II)	25	60923	$1.5523\ 10^{-12}$	$3.1384\ 10^{5}$	$1.5306\ 10^{-10}$	0.194
	50	42066	$1.4595\ 10^{-12}$	$2.3601\ 10^{5}$	$1.4927\ 10^{-10}$	0.178
	100	28481	$1.7058\ 10^{-12}$	$1.1744\ 10^{5}$	$1.6963\ 10^{-10}$	0.243
	150	18640	$2.107\ 10^{-12}$	54162	$1.7107\ 10^{-10}$	0.344
	200	12558	$2.5075\ 10^{-12}$	27988	$1.329\ 10^{-10}$	0.449
	250	9448	$3.3209\ 10^{-12}$	13719	$1.6619\ 10^{-10}$	0.689
	300	7619.5	$3.2258\ 10^{-12}$	7752.5	$1.6047\ 10^{-10}$	0.983
	350	6486	$3.393\ 10^{-12}$	5322.7	$8.5643\ 10^{-11}$	1.219
(III)	25	0	-	6884.2	$2.3452\ 10^{-10}$	-
	50	0	-	5463	$2.6812\ 10^{-10}$	-
	100	0	-	6617.2	$3.4647\ 10^{-10}$	-
	150	0	-	10952	$5.1712\ 10^{-10}$	-
	226	0	-	10486	$5.6664\ 10^{-10}$	-
	265	0	-	5870.4	$5.8652\ 10^{-10}$	-
	300	0	-	2754	$5.7039\ 10^{-10}$	-
	320	0	-	1919.5	$5.55\ 10^{-10}$	-
(IV)	Metallic					

Table VII.2: Temperature dependence of grain interior and grain boundary resistance and capacitance values of UNCD samples (I), (II), (III) and (IV).

The resistance values derived from fitting the semicircles of the Cole-Cole plots with an R-C parallel equivalent circuit are presented in a logarithmic plot against reciprocal temperature for samples (I), (II) and (III) in figures VII.6, VII.7 and VII.8, respectively. On figures VII.6 and VII.7, the temperature dependence of the simulated resistance R_{GI} for the higher frequency semicircular response (semicircles I) of sample (I) and (II) show data points that are sufficiently aligned to be considered on a straight line. From the slope of these lines, an activation energy of 0.25 eV for sample (I) and 0.11 eV for sample (II) was estimated. In contrast, the temperature dependence of the simulated resistance R_{GB} for the lower frequency semicircular response (semicircles II and III) for samples (I), (II) and (III) did not give a straight line. For sample (I) and (II), there is clearly a curvature over the temperature range whereas the data points for sample (III) are scattered and show no trend. Therefore it was not possible to find out an activation energy value for the electrical conduction that is assigned to this conduction path.

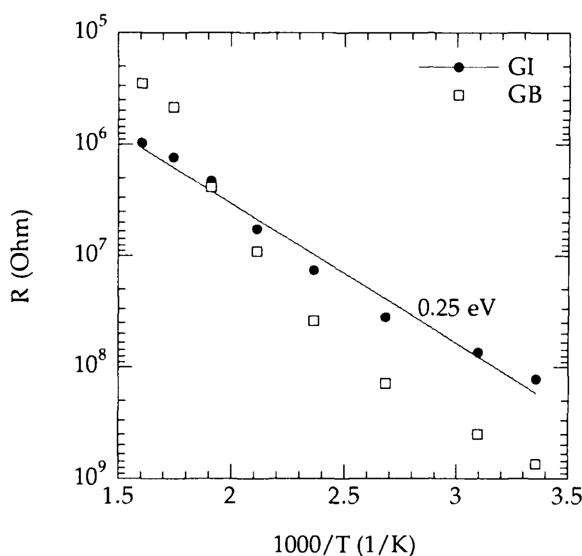

Figure VII.6: Temperature dependence of the grain interior (GI) resistance and of the grain boundary (GB) resistance for UNCD sample (I).

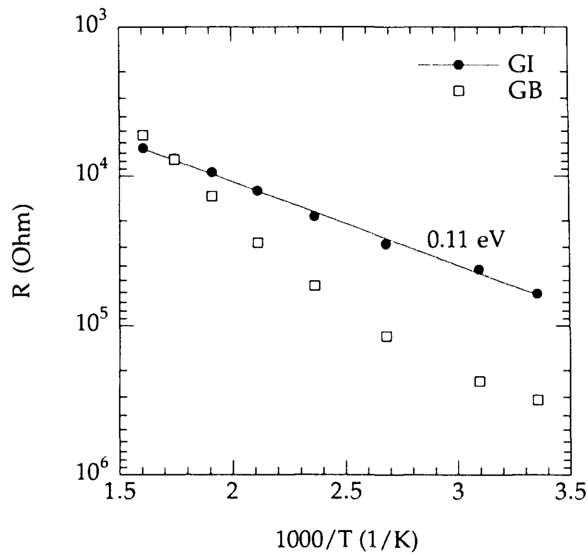

Figure VII.7: Temperature dependence of the grain interior (GI) resistance and of the grain boundary (GB) resistance for UNCD sample (II).

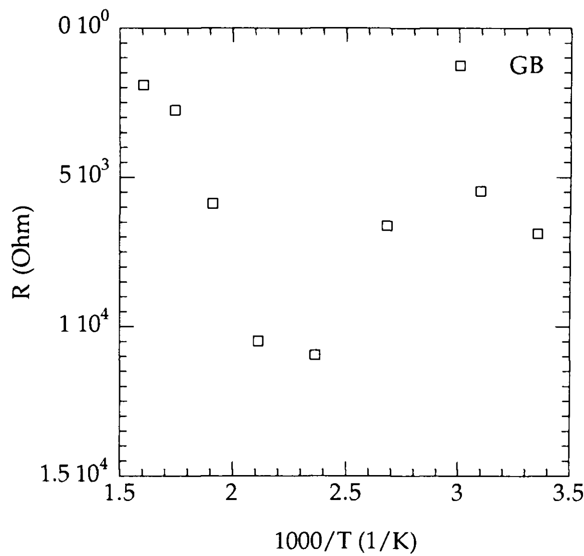

Figure VII.8: Temperature dependence of the grain interior (GI) resistance and the grain boundary (GB) resistance for UNCD sample (III).

VII.5. DISCUSSION

UNCD is a unique form of diamond grown from an Ar/CH_4 gas phase, where the electronic properties of the material are strongly influenced by the addition of nitrogen into the source gases. Conductivity and Hall effect measurements made as a function of temperature showed that UNCD films have the highest *n*-type conductivity and carrier concentration for phase-pure diamond thin films (see chapter VI). Zapol *et al.*, based on theoretical modelling, proposed that the main route of electronic conduction in these films is via hopping at the grain boundaries [18]. This view seems to be over-simplified since impedance spectroscopy measurements clearly identify several conduction paths, each conduction path being represented by a distinct semicircle in the Cole-Cole plot representation.

Each semicircle has been fitted with a parallel R-C equivalent circuit to simulate the dielectric behaviour of the UNCD films. Details of the model used can be found in chapter III, and the R and C parameters are given in table VII.2. The value of the simulated capacitance is of great importance in this work as it permits one to determine whether the electrical conductivity is due to a contribution from the contacts, the grain boundaries or the grain interiors. It has been established in the literature that a capacitance value falling in the μF range corresponds to a contribution from the contacts, whereas values in the nF and pF range are admitted to be due respectively to contributions from the grain boundaries and grain interiors [13,19-22].

An inspection of the capacitance values in table VII.2 shows that values of all three semicircles lie outside the μF range, suggesting that contributions from the contacts are not significant. In fact, this has been observed for single crystal and polycrystalline diamond, where different contact configuration effects have been investigated. The results showed no significant variation in impedance spectroscopy due to the large resistance discrimination between diamond and contact [12]. For semicircle I, all the capacitance values C_{GI} are in the pF range whilst for semicircles II and III all the C_{GB} values are in the nF range. This

implies that the former semicircular response is from grain interiors and that the latter two are from grain boundaries.

The conduction path associated with grain interiors shows an activation energy that is lower when nitrogen is incorporated in UNCD than when it is a substitutional impurity in diamond, for which it is known to give a deep donor level of 1.7 eV below the conduction band edge [23]. Assuming that the substitutional energy in the bulk of the UNCD grain is close to that in diamond crystals, it is therefore unlikely that the enhanced conductivity in UNCD is due to nitrogen doping of the grains. Evidence of this has been given by the HRTEM and EELS measurements described above, which have shown no change in the grain interiors structure, and hence in its electronic structure, when nitrogen is added to the film. Furthermore, theoretical calculations predict that nitrogen is preferentially incorporated in the grain boundary rather than in the grain interiors [18]. It is therefore suggested that the low activation energy observed here, may be due to some defect in the grain interior. Defects with similar activation energies have been observed in diamond and have been studied by thermally stimulated current (TSC) experiments [24,25].

The conduction at the grain boundaries is not an activated single energy process, unlike for the grain interior case. Whatever the nitrogen level in the films, a clear and visible curvature is seen in the Arrhenius plot for the grain boundary contribution (see figures VII.6-8). This indicates that multiple thermally activated conduction mechanisms take place in the grain boundary. This behaviour has been observed in Hall effect experiments and the conduction was attributed to an impurity band mechanism (see chapter VI). Further, with increasing nitrogen content in the source gas, the impurity band was found to widen until the impurity band overlaps with the conduction band, leading to a semi-metallic behaviour. This behaviour has been observed experimentally here. Indeed, the overall resistance of the samples varies from ~ 10^9 Ω for the sample grown without nitrogen to ~ 0 Ω when 20% of nitrogen is introduced in the source gases. This variation clearly shows that the electronic

behaviour of the samples goes from insulating to semi-conducting as the nitrogen concentration is increased up to 20%.

The response for the grain boundary conduction is given by two semicircles, namely II and III. Usually, for each conduction path, corresponds a distinct semicircle in the Cole-Cole plot. Therefore it can be assumed that the conduction at the grain boundaries is due to two different processes. The first one, as mentioned above, is due to the incorporation of nitrogen in the grain boundaries and is shown by semicircle III. Note however, that this semicircle is visible even for the sample grown without intentional nitrogen addition. SIMS measurements performed at ANL by Bhattacharyya *et al.* on a similar sample set, showed that a nitrogen concentration of 5×10^{19} cm^{-3} was present in the 0% N_2 film [10]. It is therefore legitimate to assume that the growth chamber suffered from nitrogen contamination. As a result, some nitrogen was unintentionally incorporated in the 0% N_2 film, thus giving an impedance response. The second path, given by semicircle II and that is observed in all samples, yields an activation energy of 212 meV between 25°C and 100°C in sample (I). This value is close to the one reported by Ye *et al.* [12] who studied intrinsic polycrystalline diamond using impedance spectroscopy. The authors suggested that the grain boundaries were dominating the conduction path in their sample. This observation, together with the fact the grain boundary is made of an admixture of sp^2/sp^3 or sp^2 bonded carbon atoms [9,26], leads us to think that the path shown by semicircle (II) in UNCD is due to non-diamond carbon bonding in the grain boundary.

VII.6. CONCLUDING REMARKS

Nitrogen incorporation in UNCD films results in substantial structural changes that effect the properties of these films. HRTEM showed that both the grain size and the width of the grain boundaries in this material increase with nitrogen incorporation, whilst EELS measurements verified that UNCD is composed of phase pure diamond grains and distorted carbon grain boundaries with mixed sp^2/sp^3 bonding. Impedance spectroscopy was used to

correlate the physical properties and the electronic properties in UNCD samples with different nitrogen incorporation levels. Regardless of the nitrogen content in the film, three semicircular responses have been seen in the Cole-Cole plots between 25°C and 350°C, indicating that three main conduction paths exist within the samples. The Cole–Cole plots can be accurately represented by a RC parallel circuit model and the results show good curve fitting when simulated using Zview. For one semicircle (labeled I in the text), the equivalent capacitance value was maintained in the pF range suggesting a conduction path via grain interiors. The capacitance value for the other two semicircles (labeled II and III) lied in the nF range and was attributed to grain boundary conduction. From the temperature dependence of the resistance, the conduction for the grain interior path was found to be thermally activated with a single activation energy of a few hundred meV. This is in stark contrast to the case of conventional diamond where the activation energy of substitutional nitrogen is 1.7 eV, therefore suggesting that the conduction via the grain interiors is due to some defects. Conduction at the grain boundaries takes two paths. The first one is thought to be due to nitrogen incorporation at the grain boundaries, which induces multiple thermally activated conductivity, maybe ascribed to an impurity band conduction mechanism. The second path is thought to be due to due to non-diamond carbon bonding in the grain boundary.

VII.7. REFERENCES

[1] R. B. Jackman, J. Beckman, and J. S. Foord, Appl. Phys. Lett. **66**, 1018 (1995).

[2] J. Beckman, R. B. Jackman, and J. S. Foord, Diamond Relat. Mater. **3**, 602 (1994).

[3] A. R. Krauss, O. Auciello, M. Q. Ding, D. M. Gruen, Y. Huang, V. V. Zhirnov, E. I. Givargizov, A. Breskin, R. Chechen, E. Shefer, V. Konov, S. Pimenov, A. Karabutov, A. Rakhimov, and N. Suetin, J. Appl. Phys. **89**, 2958 (2001).

[4] Q. Y. Chen, D. M. Gruen, A. R. Krauss, T. D. Corrigan, M. Witek, and G. M. Swain, J. Electrochem. Soc. **148**, E44 (2001).

[5] A. R. Krauss, O. Auciello, D. M. Gruen, A. Jayatissa, A. Sumant, J. Tucek, D. C. Mancini, N. Moldovan, A. Erdemir, D. Ersoy, M. N. Gardos, H. G. Busmann, E. M. Meyer, and M. Q. Ding, Diamond Relat. Mater. **10**, 1952 (2001).

[6] D. M. Gruen, S. Liu, A. R. Krauss, and X. Pan, J. Appl. Phys. **75**, 1758 (1994).

[7] D. M. Gruen, S. Z. Liu, A. R. Krauss, J. S. Luo, and X. Z. Pan, Appl. Phys. Lett. **64**, 1502 (1994).

[8] D. Zhou, T. G. McCauley, L. C. Qin, A. R. Krauss, and D. M. Gruen, J. Appl. Phys. **83**, 540 (1998).

[9] J. Birrell, J. A. Carlisle, O. Auciello, D. M. Gruen, and J. M. Gibson, Appl. Phys. Lett. **81**, 2235 (2002).

[10] S. Bhattacharyya, O. Auciello, J. Birrell, J. A. Carlisle, L. A. Curtiss, A. N. Goyette, D. M. Gruen, A. R. Krauss, J. Schlueter, A. Sumant, and P. Zapol, Appl. Phys. Lett. **79**, 1441 (2001).

[11] H. T. Ye, C. Q. Sun, H. T. Huang, and P. Hing, Thin Solid Films **381**, 52 (2001).

[12] H. Ye, O. A. Williams, R. B. Jackman, R. Rudkin, and A. Atkinson, Phys. Status Solidi A-Appl. Res. **193**, 462 (2002).

[13] H. Ye, C. Q. Sun, H. Huang, and P. Hing, Appl. Phys. Lett. **78**, 1826 (2001).

[14] H. Ye, R. B. Jackman, and P. Hing, J. Appl. Phys. **94**, 7878 (2003).

[15] K. Miyata and D. L. Dreifus, Jpn. J. Appl. Phys. **33**, 4526 (1994).

[16] F. Coffman, R. Cao , P. Pianetta, S. Kapoor, M. Kelly, and L. Terminello, Appl. Phys. Lett. **69**, 568 (1996).

[17] D. M. Gruen, A. R. Krauss, C. D. Zuiker, R. Csencsits, L. J. Terminello, J. A. Carlisle, I. Jimenez, D. G. J. Sutherland, D. K. Shuh, W. Tong, and F. J. Himpsel, Appl. Phys. Lett. **68**, 1640 (1996).

[18] P. Zapol, M. Sternberg, L. A. Curtiss, T. Frauenheim, and D. M. Gruen, Physical Review B (Condensed Matter and Materials Physics) **65**, 045403 (2002).

[19] J. R. Macdonald, *Impedance Spectroscopy: Emphasizing Solid Materials and Systems* (Wiley, New York, 1987).

[20] S.-E. Park, H.-M. Kim, K.-B. Kim, and S.-H. Min, Thin Solid Films **341**, 52 (1999).

[21] J.-C. M'Peko, D. L. Spavieri, J. , and M. F. de Souza, Appl. Phys. Lett. **81**, 2827 (2002).

[22] A. Huanosta, O. Alvarez-Fregoso, E. Amano, C. Tabares-Munoz, M. E. Mendoza-Alvarez, and J. G. Mendoza-Alvarez, J. Appl. Phys. **69**, 404 (1991).

[23] J. Robertson and C. A. Davis, Diamond Relat. Mater. **4**, 441 (1995).

[24] C. De Blasi, S. Galassini, G. Micocci, L. Ruggiero, and A. Tepore, Nuclear Instruments and Methods **163**, 121 (1979).

[25] D. Tromson, P. Bergonzo, A. Brambilla, C. Mer, F. Foulon, and V. N. Amosov, Physica Status Solidi A: Applied Research **174**, 155 (1999).

[26] J. Narayan, J. Mater. Res. **5**, 2414 (1990).

CHAPTER VIII
PHOSPHORUS-DOPED DIAMOND: IMPEDANCE SPECTROSCOPY

VIII.1. Introduction
VIII.2. Experimental methods
VIII.3. Results
VIII.3.1. Current-voltage characteristics
VIII.3.2. Impedance spectroscopy measurements
VIII.4. Discussion
VIII.6. Concluding remarks
VIII.7. References

VIII.1. INTRODUCTION

Diamond has a combination of extreme physical, chemical, and electrical properties which makes it an attractive material for high power and high temperature electronic applications [1]. However, although high quality chemical vapour deposition (CVD) diamond thin films have been produced for a number of years, development of diamond electronics has been hindered due to the difficulty of obtaining *n*-type semiconducting diamond. It has been reported that lithium ion implantation can successfully transform intrinsic diamond into an n-type semiconductor [2,3]. However, implanting ions causes an irrevocable graphitisation in the diamond; the conductivity being more correctly assigned to damage sites within the diamond [4]. Other reports mentioned growing *n*-type diamond using sulphur [5], with or without intentional co-doping with boron [6], or a combination of boron doping followed by a deuterium treatment [7]. Unfortunately none of these approaches has led to reproducible n-type behaviour in diamond. Phosphorus doping of diamond during the CVD process has been studied [8-10]. *N*-type conductivity was claimed but it was not confirmed by Hall effect measurements. One of the difficulties in obtaining *n*-type diamond was

suggested to be the passivation of the P donors by the presence of hydrogen or crystalline imperfections in the doped film. Indeed some studies showed that for the case of P doping by the use of phosphine gas during CVD diamond growth, large amounts of hydrogen were incorporated into the growing film [4,11]. For these films, neither *n*-type conduction nor sometimes even electrical conduction could be obtained. The situation has significantly improved recently, with phosphorus-based *n*-type doping with good reproducibility, together with the growth of high quality diamond, being achieved by several groups in Japan [12] and Europe [13,14]. The *n*-type character of the films was clearly demonstrated using Hall effect measurements and thermal activation energy values, within the range 0.43-0.6 eV [12,15-18], were derived from the temperature dependence of the carrier density. A number of experimental studies have been focused on the exact determination of the ground level of phosphorus donor in diamond using a range of optical spectroscopic techniques. An ionisation energy of (630±50) meV has been derived from cathodoluminescence measurements [19], while photoionisation energy values of (0.56±0.03) eV [20] and later (0.59±0.03) eV [21] have been reported from constant photocurrent measurements. Gheeraert *et al.* [22,23], using infrared absorption spectroscopy, observed an absorption threshold at 510 meV and further showed that the excited states of P in diamond could be correctly described by the effective-mass approximation. On this basis they were able to deduce a value of (600±20) meV for the optical ionisation energy of P in diamond [22]. There is therefore a growing amount of experimental evidence indicating that P introduces a donor level at 0.6 eV below the bottom of the conduction band. A breakthrough in the CVD diamond electronic device was achieved combining both P and boron (*p*-type) doping with a p-n junction being successfully constructed [24].

In addition to the identification of the activation energy for the phosphorus donor level, it is important to identify any electrically active defect states (that therefore also contribute to conductivity within the film) that may accompany the introduction of phosphorus to diamond. To this end, we have previously reported charge-based deep level transient

spectroscopy (Q-DLTS) measurements on P-doped diamond [25]. Four distinct peaks were observed in the Q-DLTS spectra, corresponding to states within the range 0.42–0.6eV; poor Schottky contacts were thought to be influencing the measurements, through the introduction of re-trapping effects caused by high leakage currents at the metal-diamond interface. In this chapter impedance spectroscopy, which conventionally uses ohmic contacts to the semiconductor concerned, has been used to gain further insight into this important system. Impedance spectroscopy has been widely utilised to study the conduction paths within a range of conducting and less conducting material [26-28], but its application to diamond films is relatively limited. This technique has been previously used to characterise polycrystalline and nanocrystalline CVD diamond films [29-31] where the contributions from the grains, grain boundaries and electrodes were observed. The strength of the impedance technique lies in its ability to identify the individual components that contribute to the overall conductivity; in the present case, which involves phosphorus-doped single crystal diamond, two contributions are clearly identified.

VIII.2. EXPERIMENTAL METHODS

The sample used throughout was a phosphorus doped homoepitaxial diamond film, grown by microwave enhanced plasma chemical vapour deposition onto a high pressure high temperature (HPHT) synthetic Ib diamond {111} substrate with a top surface of about 2×2 mm^2. The sample was grown at the National Institute of Research in Inorganic Materials, Tsukuba, Japan, according to a growth process described elsewhere [17]. Four phosphorus heavily doped regions were formed at its square corners (referred to as P^+ contacts in the text) and were capped by Au to form electrodes on the surface [32]. Hall effect measurements, using Van de Pauw geometry, confirmed that the P-doped sample was *n*-type in character with a donor density of 6×10^{17} cm^{-3}.

All the electrical measurements were taken between two symmetric electrodes across the sample's surface in air. A picoammeter-voltage source (Keithley 487) was used to record the current-voltage (I-V) characteristics between -10 V and 10V. An increment of 500 mV was used. Impedance measurements of the film were carried out using an impedance spectroscopy system (Solartron 1260A) in the frequency range 0.1 Hz to 10 MHz, from 27°C up to 300°C. The set up parameters were 0.05V of ac amplitude, one second integration time, and no delay time.

VIII.3. RESULTS

VIII.3.1 Current-voltage characteristics

The I-V characteristics of the sample were recorded at different temperatures between room temperature (RT) and 300°C (figure VIII.1(a)). It can be seen that when the current was measured between two symmetrical Au-P^+ contacts, a good linearity was observed at room temperature. However an upward curvature was visible at 75°C, becoming stronger with increasing temperature (figure VIII.1(b)). This S-shape behaviour clearly indicates that the contact departs from ideal ohmic behaviour at temperatures greater than 75°C.

(a)

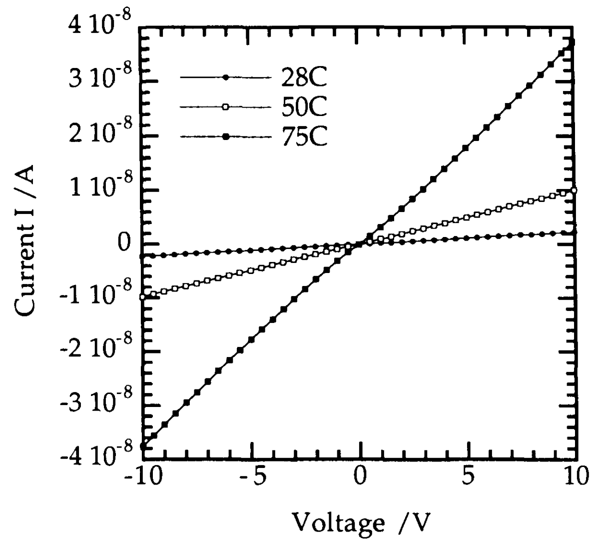

(b)

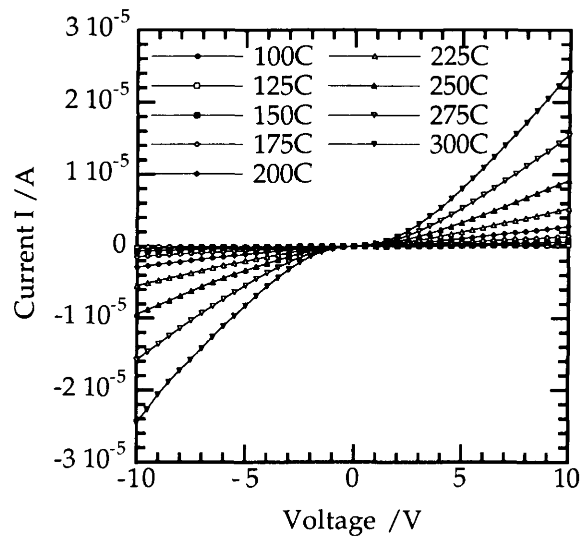

Figure VIII.1: Current-voltage characteristics (I-V) of the P-doped diamond film measured between 2 Au-P^+ contacts, from (a) 28°C to 75°C and from (b) 100°C to 300°C.

VIII.3.2 Impedance spectroscopy measurements

The temperature dependence of the Cole-Cole plots measured for the P-doped sample is shown in figure 2. Figure VIII.2(a) presents the data measured at 27°C and 50°C. At these temperatures, a semicircular response with some scatter in the data at the low frequency impedance range (right-side) is present. However, beyond 75°C (figure VIII.2(b) to VIII.2(f)) the semicircular response is accompanied by an additional semicircle (or an arc at 75°C) which extends to low frequencies. The resistance and the capacitance value for each semicircle can be obtained by fitting each curve or arc based on a single R-C parallel equivalent circuit. The resistance and the capacitance values which have been simulated for each semicircle using Zview software supplied by Solartron Inc. are shown in table VIII.1. With increasing temperature, it is found that the semicircle on the right hand side gets larger with respect to the one on the left hand side. This transition is normally attributed to a progressive change in the dominating conduction path with increasing temperature since each conduction path is associated with a semicircle. The order of magnitude of the x-axis also decreases significantly from 10^9 Ω at 27°C to 10^6 Ω at 300°C, indicating that the overall resistance of the sample has dropped by three orders of magnitude.

(a)

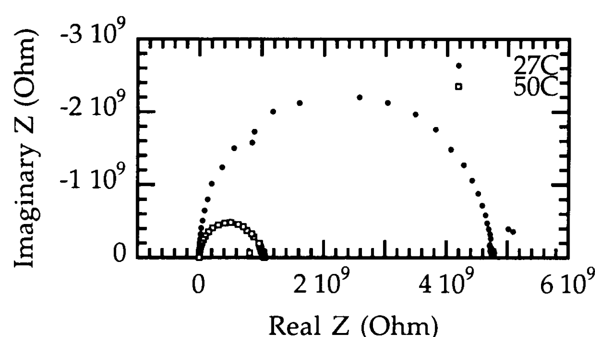

(b)

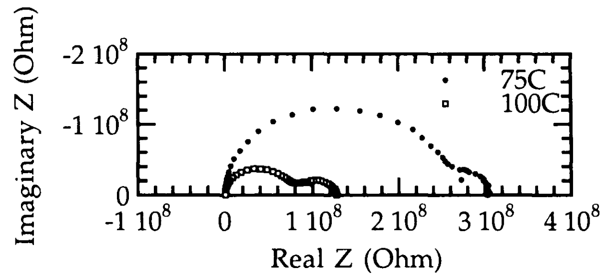

(c)

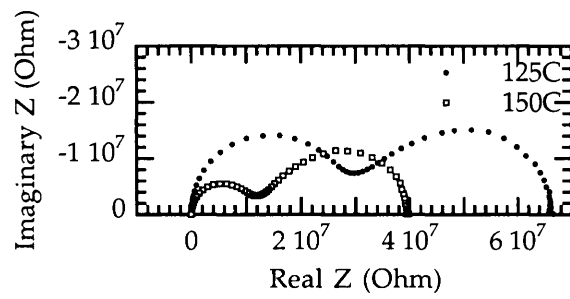

(d)

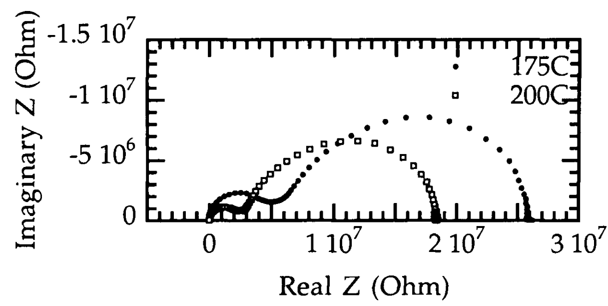

(e)

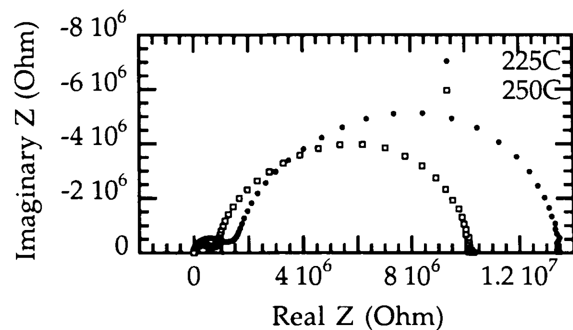

(f)

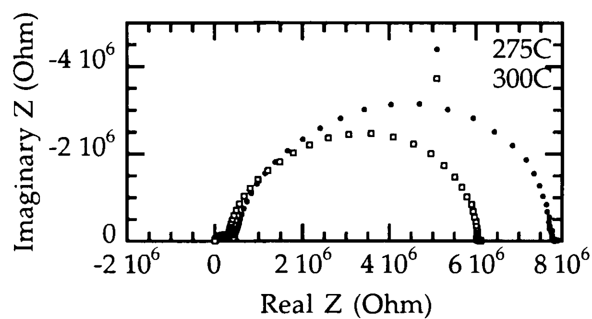

Figure VIII.2: Cole-Cole plots on the P-doped single crystalline diamond film at different temperatures: (a) 27°C and 50°C, (b) 75°C and 100°C, (c) 125°C and 150°C, (d) 175°C and 200°C, (e) 225°C and 250°C, and (f) 275°C and 300°C.

Temperature (°C)	R_1 (Ω)	C_1 (F)	R_2 (Ω)	C_2 (F)
27	4.7362×10^{9}	7.5799×10^{-13}	-	-
50	9.5288×10^{8}	8.3535×10^{-13}	-	-
75	2.4228×10^{8}	8.2696×10^{-13}	5.2331×10^{7}	1.2737×10^{-10}
100	7.1975×10^{7}	7.2381×10^{-13}	5.0151×10^{7}	1.0216×10^{-10}
125	2.7678×10^{7}	7.3377×10^{-13}	2.9344×10^{7}	1.6944×10^{-10}
150	1.087×10^{7}	6.8548×10^{-13}	2.2164×10^{7}	1.773×10^{-10}
175	4.6325×10^{6}	6.8548×10^{-13}	1.7455×10^{7}	1.6754×10^{-10}
200	2.2677×10^{6}	7.0171×10^{-13}	1.3706×10^{7}	1.7165×10^{-10}
225	1.1486×10^{6}	8.7368×10^{-13}	1.0631×10^{7}	1.7554×10^{-10}
250	5.9474×10^{5}	6.7217×10^{-13}	8.5078×10^{6}	1.7219×10^{-10}
275	3.1446×10^{5}	7.3869×10^{-13}	6.3384×10^{6}	1.9193×10^{-10}
300	2.4924×10^{5}	8.2023×10^{-13}	5.0932×10^{6}	1.9086×10^{-10}

Table VIII.1: Temperature dependence of the resistance and capacitance for the conduction paths within the P-doped sample.

In figure VIII.3 the resistance values derived from fitting the semicircles of the Cole-Cole plots with an R-C parallel equivalent circuit are presented in a logarithmic plot against reciprocal temperature. Two straight lines are apparent, enabling from their respective slopes to be used to determine an activation energy for each conduction path. Activation energies of 0.53 eV and 0.197 eV were found from fitting respectively the semicircle that appears at high frequencies (on the left) and at low frequencies (on the right). The semicircle at low frequencies only appearing at temperatures above 75°C, the activation energy of 0.197 eV was only found over the reduced temperature range 100-300°C.

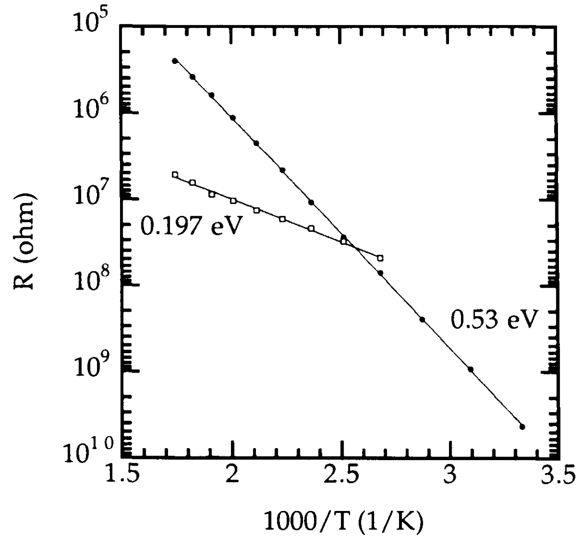

Figure VIII.3: Temperature dependence of electrical resistance on P-doped diamond film.

VIII.4. DISCUSSION

Impedance spectroscopy is able to correlate electrical properties and physical properties using equivalent circuit models on a non-destructive basis. Theoretically, a model consisting of a succession of R-C parallel circuits in series could be used to simulate the different electrical conduction paths within the diamond film [30,33]. Each parallel R-C equivalent circuit accurately fits each semicircle of the Cole-Cole plot. The complex impedance Z* measured by the Solartron impedance spectroscopy meter can be expressed as:

$$Z^* = Z' - j\,Z'' \quad \text{(VIII.1)}$$

with

$$Z' = \sum_{i=1}^{n} \frac{R_i}{1 + \omega^2 R_i^2 C_i^2} \quad \text{(VIII.2)}$$

$$Z"=\sum_{i=1}^{n}\frac{\omega R_i^2 C}{1+\omega^2 R_i^2 C_i^2} \qquad \text{(VIII.3)}$$

where $i \in \mathrm{N}$ and $n \in \mathrm{N}$.

Z' and Z" represents the real an imaginary portions of the impedance, respectively, and ω is the angular frequency. When plotted in a complex plan, Z" versus Z' takes the form of n semicircles. In this representation, the n different conduction paths can be studied separately and the contribution from grain interiors, impurity bands, grain boundaries or electrodes can be identified. It has already been established in the literature that the contribution from the electrode, grain boundary and grain interior can be determined from the simulated capacitance value of each semicircle, which normally have a capacitance value in the range of μF, nF and pF, respectively [31,33-36].

A central issue to be addressed here is what portion of the equivalent circuit corresponds to the two observed semicircular responses. For diamond, different electrode configuration effects have been investigated and the results showed no significant variation in impedance spectroscopy due to its large resistance discrimination between diamond and electrode [30]. Further, in this case, the capacitance values of both semicircles lie outside the μF range normally associated with electrode effects, again suggesting that contributions from the Au electrodes are not significant. For the semicircle occurring at high frequencies, all the capacitance values C_1 are in the range of pF (see table VIII.1). This implies this semicircular response is from grain interiors, which is expected from a single crystal diamond where no grain boundaries are involved.

The capacitance values C_2 of the semicircle occurring at low frequencies lie in the range of nF (table VIII.1). Grain boundaries are normally associated with such values. Since the sample is a single crystal, the grain boundary effects are not expected. Indeed, in our previous study of boron-doped single crystal diamond using impedance spectroscopy, only one semi-circular response was seen. This displayed an activation energy (E_a) of 0.36eV,

characteristic of the substitutional boron acceptor state [37]. However a second (nF) semicircle is seen here at higher temperatures. An inspection of the grain boundaries in polycrystalline diamond reveals that the carbon atoms are no longer arranged according to their tetragonal structure but instead mixed sp^2/sp^3 or sp^2 phases are present [38]. It is therefore legitimate to assume that the semicircle with capacitance values falling in the nF range is due to non-diamond carbon bonding. The P^+ contacts are heavily doped regions. Keeping in mind that P is a large atom for the diamond lattice, it is reasonable to think that the incorporation of a high concentration of P atoms to form the P^+ contacts would locally perturb the diamond lattice periodicity to such an extent that some of the carbon atoms would finally bond in a similar manner as they would do in the grain boundary region of polycrystalline material. As a result the contribution to the impedance spectroscopy measurements of the P^+ contacts in this single crystal would be similar to that of grain boundaries in a polycrystalline material giving rise to a semicircle in the Cole-Cole plot in which capacitance values would be in the nF range.

Further evidence of this can be found from inspection of the behaviour of the I-V characteristics as a function of temperature, as shown in figure VIII.1(a) and VIII.1(b). It is found that the contacts give linear I-V characteristics from RT up to 75°C. Above that temperature a curvature is clearly visible becoming stronger with increasing temperature. Note that this temperature also corresponds to the occurrence of the lower frequency semi-circle in the Cole-Cole plot (see figure VIII.2(b)), so that there exists a direct correlation between curvature in the I-V characteristic on one hand, and the presence of the lower frequency semicircle on the other hand. The electronic properties of contacts to phosphorus doped diamond samples have been studied by Teraji *et al.* [39,40] Their results indicate that ohmic contacts are difficult to form on P-doped diamond using commonly evaporated metals, but that good ohmic contacts can be obtained at RT when such metals are deposited onto selectively grown, heavily doped diamond layers [32]. Note that in such regions the material was also thought to be defective which supports the assertion made here that the nF response relates to non-diamond carbon bonding. In fact, evaporation of metal contacts

to P-doped diamond often leads to an S-shape characteristic of the type shown in figure VIII.1. This has been previously explained in terms of tunnelling at the higher potentials [40]. The same author also suggested that the S shape of the I-V curve may originate from the difference between the temperature dependence of the film resistance and that of the contact resistance. Since the activation energy for the P-doped diamond is large (about 0.6eV), the resistivity of the diamond film would decrease rapidly with increasing temperature while that of the contact would remain largely unaffected. These findings strongly suggest that the occurrence of the S-shape behaviour in the I-V characteristic of P-doped diamond is closely related to the presence of a non negligible resistance in the contact region, as opposed to the bulk of the diamond. In the case of the sample studied here, the change in the shape of the I-V characteristic at around 75°C therefore indicates that a transition from a conduction mechanism dominated by the bulk of the diamond, to one which is partly controlled by the region in close proximity to the metal contacts, occurs. In the case of a contact scheme similar to the one used here, Teraji *et al.* suggested that the current flow could be controlled by thermionic-field emission at low applied electric fields, replaced by field emission at higher fields [32]. Since impedance spectroscopy results have shown that there is no limitation from the Au-diamond interface to the current flow, it is reasonable to conclude that the S-shape behaviour observed here originates from the highly-doped regions underneath the metal contacts. Therefore, this provides further evidence that the second, low frequency, semicircle observed in the Cole-Cole plots of figure VIII.2(b)–(f) at temperatures in excess of 75 °C indeed originates from the P^+-doped regions within the sample.

The activation energy E_a for the P donor atom has been found to vary from 0.43eV [12], 0.56eV [41], 0.6eV [17,20,39], 0.63 eV [42] and recently 0.57 eV [18]. Here the value for E_a was found to be 0.53eV from the variation of resistance (R) with temperature. This value is in agreement with those reported in the past however it is a bit lower than the value of 0.6 eV corresponding to the ground level of the P-related donor level. This discrepancy is thought to arise from the various scattering mechanisms such as inter-valley scattering as

well as phonon scattering [18]. Indeed, when such events take place, the mobility of the carriers in the P-doped sample will be temperature dependent. Katagari *et al.* [18] have reported that the mobility was decreasing with temperature as $T^{-1.4}$ up to 450 K and was decreasing as $T^{-2.6}$ above 450 K. The activation energy in our experiment was deduced from the variation of R with T, where R is both a function of mobility and carrier concentration. With increasing temperature it is expected that the carrier concentration increases, therefore R would be expected to increase with T. However if the mobility is also a function of T, as we expect in the present case, then since the mobility is decreasing with increasing temperature, the variation of R would be smaller than if the mobility value remained constant with increasing temperature. The direct consequence of this is a decrease in activation energy, as observed in our experiments.

VIII.5. CONCLUDING REMARKS

The reliable introduction of phosphorus into {111} oriented homoepitaxial diamond layers to create n-type conductivity is an important development in the topic of diamond electronics. A wide range of techniques have been used previously to determine the position of the donor level within the band gap of diamond. Whilst values in the range 0.43-0.6eV have been reported, it is believed that 0.6eV is the activation energy for the ground state of the donor atom relative to the conduction band edge. In this chapter we have used impedance spectroscopy to identify the components that contribute to the overall conductivity of phosphorus doped diamond films. Two semicircular responses have been seen in Cole-Cole plots when they are recorded at temperatures above 75^0C; below this a single semicircle is seen. One state reveals an activation energy of 0.53eV, with a capacitance in the pF range. This can be attributed to the P donor level in the crystalline bulk of the homoepitaxial layer; the fact that the value of E_a is slightly less than 0.6eV can be understood in terms of reducing mobility values for electrons within these films as temperature is increased. The other state gives an activation energy of 0.197eV, and a

capacitance in the nF range. The most likely assignment for this state is material with poor crystalline quality associated with the heavily phosphorus doped regions under the metal contacts. It appears that high crystalline quality diamond can be generated which includes sufficient phosphorus concentrations for effective n-type doping. However, at concentrations that are typically required for the generation of tunnelling (and hence ohmic) contacts, the diamond lattice becomes damaged, introducing other electrically active states. This implies that other approaches for the formation of good ohmic contacts to phosphorus doped diamond are required.

VIII.6. REFERENCES

[1] G. S. Gildenblat, S. A. Grot, and A. R. Badzian, Proc. IEEE **79**, 647 (1991).

[2] V. S. Vavilov, M. I. Guseva, E. A. Konorova, and V. F. Sergienko, Sov. Phys. Semicond. **4** (1970).

[3] S. Prawer, C. Uzan-Saguy, G. Braunstein, and R. Kalish, Appl. Phys. Lett. **63**, 2502 (1993).

[4] J. F. Prins, Physical Review B **31**, 2472 (1985).

[5] I. Sakaguchi, M. N.-Gamo, Y. Kikuchi, E. Yasu, H. Haneda, T. Suzuki, and T. Ando, Phys. Rev. B **60**, R2139–R2141 (1999).

[6] S. C. Eaton, A. B. Anderson, J. C. Angus, Y. E. Evstefeeva, and Y. V. Pleskov, Electrochem. Solid-State Lett. **5**, G65 (2002).

[7] Z. Teukam, J. Chevallier, C. Saguy, R. Kalish, D. Ballutaud, M. Barbé, F. Jomard, A. Tromson-Carli, C. Cytermann, J. E. Butler, M. Bernard, C. Baron, and A. Deneuville, Nature Materials **2**, 482–486 (2003).

[8] M. Kamo, H. Yurimoto, T. Ando, and Y. Sato, in *Proceedings of the 2nd International Conference on New Diamond Science and Technology, Materials Research Society*, edited by R. Messier, J. T. Glass, J. E. Butler, and R. Roy (1991), p. 637.

[9] K. Okano, H. Kiyota, T. Iwasaki, Y. Nakamura, Y. Akiba, T. Kurosu, M. Iida, and T. Nakamura, Appl. Phys. A-Mater. Sci. Process. **51**, 344 (1990).

[10] A. E. Alexenko and B. V. Spitsyn, Diamond Relat. Mater. **1**, 705 (1992).

[11] T. Ando, H. Haneda, M. Akaishi, Y. Sato, and M. Kamo, Diamond Relat. Mater. **5**, 34 (1996).

[12] S. Koizumi, M. Kamo, Y. Sato, H. Ozaki, and T. Inuzuka, Appl. Phys. Lett. **71**, 1065 (1997).

[13] M. Nesladek, K. Haenen, J. D'Haen, S. Koizumi, and H. Kanda, Phys. Status Solidi A-Appl. Res. **199**, 77 (2003).

[14] A. Tajani, E. Gheeraert, N. Casanova, E. Bustarret, J. A. Garrido, G. Rumen, C. E. Nebel, M. E. Newton, and D. Evans, Phys. Status Solidi A-Appl. Res. **193**, 541 (2002).

[15] S. Koizumi, M. Kamo, Y. Sato, S. Mita, A. Sawabe, A. Reznik, C. Uzan-Saguy, and R. Kalish, Diamond Relat. Mater. **7**, 540 (1998).

[16] S. Koizumi, Phys. Status Solidi A-Appl. Res. **172**, 71 (1999).

[17] S. Koizumi, T. Teraji, and H. Kanda, Diamond Relat. Mater. **9**, 935 (2000).

[18] M. Katagiri, J. Isoya, S. Koizumi, and H. Kanda, Appl. Phys. Lett. **85**, 6365 (2004).

[19] H. Sternschulte, K. Thonke, R. Sauer, and S. Koizumi, Physical Review B **59**, 12924 (1999).

[20] M. Nesladek, K. Meykens, K. Haenen, L. M. Stals, T. Teraji, and S. Koizumi, Physical Review B **59**, 14852 (1999).

[21] K. Haenen, K. Meykens, M. Nesladek, G. Knuyt, L. M. Stals, T. Teraji, S. Koizumi, and E. Gheeraert, Diamond Relat. Mater. **9**, 952 (2000).

[22] E. Gheeraert, S. Koizumi, T. Teraji, and H. Kanda, Solid State Communications **113**, 577 (2000).

[23] E. Gheeraert, N. Casanova, S. Koizumi, T. Teraji, and H. Kanda, Diamond Relat. Mater. **10**, 444 (2001).

[24] S. Koizumi, K. Watanabe, M. Hasegawa, and H. Kanda, Science **292**, 1899 (2001).

[25] O. Gaudin, D. K. Troupis, R. B. Jackman, C. E. Nebel, S. Koizumi, and E. Gheeraert, J. Appl. Phys. **94**, 5832 (2003).

[26] A. Huanosta and A. R. West, J. Appl. Phys. **61**, 5386 (1987).

[27] D. C. Sinclair and A. R. West, Physical Review B **39**, 13486 (1987).

[28] N. Hirose and A. R. West, J. Am. Ceram. Soc. **79**, 1633 (1996).

[29] H. T. Ye, C. Q. Sun, H. T. Huang, and P. Hing, Thin Solid Films **381**, 52 (2001).

[30] H. Ye, O. A. Williams, R. B. Jackman, R. Rudkin, and A. Atkinson, Phys. Status Solidi A-Appl. Res. **193**, 462 (2002).

[31] H. Ye, C. Q. Sun, H. Huang, and P. Hing, Appl. Phys. Lett. **78**, 1826 (2001).

[32] T. Teraji, M. Katagiri, S. Koizumi, T. Ito, and H. Kanda, Jpn. J. Appl. Phys. **42**, L882 (2003).

[33] J. R. Macdonald, *Impedance Spectroscopy: Emphasizing Solid Materials and Systems* (Wiley, New York, 1987).

[34] S.-E. Park, H.-M. Kim, K.-B. Kim, and S.-H. Min, Thin Solid Films **341**, 52 (1999).

[35] J.-C. M'Peko, D. L. Spavieri, J. , and M. F. de Souza, Appl. Phys. Lett. **81**, 2827 (2002).

[36] A. Huanosta, O. Alvarez-Fregoso, E. Amano, C. Tabares-Munoz, M. E. Mendoza-Alvarez, and J. G. Mendoza-Alvarez, J. Appl. Phys. **69**, 404 (1991).

[37] H. Ye, O. Gaudin, R. B. Jackman, P. Muret, and E. Gheeraert, Physica Status Solidi A **199**, 92 (2003).

[38] J. Narayan, J. Mater. Res. **5**, 2414 (1990).

[39] T. Teraji, S. Koizumi, S. Mita, A. Sawabe, and H. Kanda, Jpn. J. Appl. Phys. **38**, L1096 (1999).

[40] T. Teraji, S. Koizumi, and H. Kanda, Physica Status Solidi A: Applied Research **181**, 129 (2000).

[41] A. Reznik, R. Kalish, and S. Koizumi, in *Proc. 6th NIRIM Intern. Symp. Advanced Material, NIRIM, Ibaraki*, edited by Y. Bando, M. Akaishi, H. Kanda, Y. Matsui, T. Kobayashi, K. Watanabe, K. Seki, and N. Yamashita (1998), p. 27.

[42] E. Gheeraert, S. Kozumi, T. Teraji, H. Kanda, and M. Nesladek, Phys. Status Solidi A-Appl. Res. **174**, 39 (1999).

CHAPTER IX
CONCLUDING REMARKS

Two of the main issues that have been hindering the development of electronic devices from diamond have been studied in this thesis. The problems associated with low growth rates and doping diamond have been addressed. In the light of the results that have been obtained, a few conclusions can be drawn with regard to the growth processes used and the approach for achieving the *p*- and *n*-type conductivity necessary for device fabrication.

In this study, MWPECVD has been used to grow electronic grade diamond films, which exhibited *p*-type surface conductivity due to hydrogen termination. The use of these surfaces offers a simple and easy way to produce electronic devices, as no doping of the material is necessary. Furthermore these layers require little thermal activation, permitting device operation at room temperature. This property has been used to fabricate some of the most promising diamond-based electronic devices reported over the past few years, but no control over the transport properties was exerted despite several attempts to vary the nature of the hydrogenation process. This consequently left the device engineer unable to 'tune' the characteristics of the device structure being made. In spite of this, a clear correlation between surface roughness, which becomes greater with film thickness, sheet carrier concentration and mobility values has been demonstrated during the course of this work. The rougher films showed the highest sheet carrier concentration and the lower mobility values. It was proposed that the roughness of these films increased the surface area and hence more surface hydrogen bonds could contribute to the conduction process by out-diffusing electrons into a surface based adsorbate layer. This would lead to a higher sheet carrier concentration whilst the mobility is reduced by the roughness of the surface and scattering at the grain boundaries. The problem of low growth rates has also been addressed where rates as high as 50 μm/h have been achieved without addition of nitrogen in the

growth gas mixture, which is known to increase the growth rate but unfortunately degrades the electronic properties.

Although some impressive device have been fabricated based on hydrogen surface conductivity, the instability of the surface to atmospheric and temperature fluctuation is likely to hinder any commercialisation of these devices. Passivation with inorganic and organic coatings was therefore investigated to circumvent this matter if useful devices are to emerge from this technology. The inorganic material (CaF_2), did not show conclusive results as the conductivity under the passivation layer was lost, but the inorganic coatings (photoresist and olive oil) achieved good results up to about 200°C. Above this temperature, the passivation layers suffered from thermal degradation, causing the conductivity of the layer beneath to be eventually lost. Therefore if reliable devices are to emerge from hydrogenated diamond technology, more temperature resilient passivating layers need to be found.

Problems with doping diamond *n*-type have been investigated as it has hindered the development of diamond as a device material. Much work is currently being undertaken to find a shallow *n*-type dopant, but without success. However, nitrogen in UNCD seems to act as such dopant. Hall effects measurements performed on nitrogenated UNCD films have showed that the conductivity is *n*-type, with a low thermal activation energy. This contrasts to the case in single and polycrystalline diamond, where the activation energy of substitutional nitrogen is 1.7 eV, suggesting that nitrogen is not substitutional in UNCD films. Instead, nitrogen introduces shallow donor states, which leads to a curious increase in carrier population at low temperatures, possibly linked with an impurity band conduction process. This impurity band seems to be widening with increasing nitrogen concentration until it merges with the conduction band. This is believed to be responsible for the fact that the films become more and more conductive with increasing nitrogen in the growth gas mixture until the conduction becomes semi-metallic for 20% nitrogen film. Based on this model, a critical impurity concentration is predicted to be 8×10^{18} cm^{-3}, which is consistent

with the literature. Evidence of hopping conduction has also been observed at low temperatures in these films.

Impedance spectroscopy measurements were conducted to correlate the physical and electronic properties of UNCD films in order to learn more about the *n*-type conduction in these films. Three semicircles were observed indicating that three main conduction paths exist within UNCD. This observation was made regardless of the nitrogen level in the films. Based on the equivalent resistance and capacitance values derived from the impedance data, contributions from the grain interiors and the grain boundaries have been isolated from the overall conduction. The equivalent capacitance values for two semicircles were maintained in the nF range, suggesting a conduction via grain boundaries, while values in the pF for the last semicircle were attributed to a grain interior conduction mechanism. The temperature-dependence resistance measurements showed an activation energy of a few meV for the grain interiors, suggesting that the conduction via the grain interiors is due to some defects. On the other hand, the conduction via the grain boundaries was found to be multiple thermally activated and the conduction mechanism was ascribed to nitrogen forming an impurity band. Non-diamond carbon atoms in the grain boundaries were identified a complementary conduction route within UNCD films.

To assess the reliability of the impedance spectroscopy technique and to verify the validity of the results obtained on UNCD, a phosphorus-doped single crystal diamond was measured as a reference sample. This sample is known to be *n*-type with a 0.6 eV activation energy. The impedance spectroscopy results showed two semicircles for all temperatures above 75°C; a single semicircle being observed at temperatures below this. The results suggest the presence of two conduction paths with activation energies of 0.53 eV and 0.197 eV. The former was attributed to the phosphorus donor level, being lower than 0.6 eV due to reduced mobility within the film at elevated temperatures. The latter was discussed in terms of defects in the highly phosphorus-doped region under the ohmic contact being used. At the view of these results it was concluded that the impedance spectroscopy technique is

a powerful tool to investigate and understand the electrical conduction mechanisms within different types of diamond films.

The work carried out in this thesis has found a new route to obtain *n*-type diamond with low activation energy. This could open up prospects for novel diamond-based applications and devices to be manufactured, where both types of dopants are required. Although a shallower *p*-type dopant is still looked for, the field of diamond electronics would benefit from investigating the nitrogenated UNCD/boron-doped diamond interfaces with the view of fabricating new device structures.